DEPARTAMENTO DE ASTROFÍSICA

Universidad de La Laguna

Search and characterization of exo-Earths: Participation in the development of the ESPRESSO spectrograph for the VLT

Memoria que presenta
Don Alejandro Suárez Mascareño
para optar al grado de
Doctor por la Universidad de La Laguna.

INSTITUTO Đ ASTROFISICA Đ CANARIAS
octubre de 2016

Examination date: November, 2016
Thesis supervisors: Dr. R. Rebolo López & Dr. J. I. González Hernández

Resumen

La búsqueda de exotierras por medio de espectroscopía doppler se enfrenta hoy en día a dos grandes dificultades. La primera es de carácter técnico. En estrellas de tipo solar la precisión de los instrumentos existentes limita la amplitud de las señales que se pueden medir a aquellas producidas por supertierras a separaciones orbitales cercanas a sus estrellas. Los planetas de tipo terrestre orbitando alrededor de estrellas de tipo solar producen variaciones muy inferiores a 1 m s^{-1} excepto a distancias muy cercanas a la estrella. La llegada de ESPRESSO y el Laser Frequency Comb como unidad de calibración paliarán esta limitación al llevar la precisión de las medidas hasta el rango de los 5 cm s^{-1}. Hasta ese momento la búsqueda en estrellas de tipo solar queda limitada a supertierras. La alternativa en estos momentos está en la búsqueda alrededor de estrellas de tipo M, ya que su baja masa hace que las señales de los planetas de tipo terrestre sean detectables con los instrumentos actuales. La segunda dificultad está en las variaciones en velocidad radial producidas por las inhomogeneidades de la superficie de las estrellas. Los cambios en las regiones activas de la superficie en las estrellas y su rotación provocan variaciones periódicas en la velocidad radial que pueden ir desde menos de 1 m s^{-1} en estrellas tranquilas hasta varias decenas de m s^{-1} en las más activas y pueden ser fácilmente confundidas con la variación provocada por planetas rocosos. En el caso de las estrellas M la necesidad de realizar este análisis de las señales originadas por la actividad estelar se vuelve aun más importante. Las señales inducidas por las estrellas M tempranas tienen periodos compatibles con los de las órbitas de los planetas en la zona habitable de estas estrellas, y amplitudes compatibles con las de las supertierras. Con el aumento de precisión previsto para el futuro estas señales aparecerán hasta en las estrellas menos activas conocidas, resultando cada vez más importante entenderlas y modelarlas correctamente. Usando series temporales de indicadores cromosféricos de espectros de alta resolución y curvas fotométricas estudiamos la variabilidad de 176 estrellas de baja actividad magnética de tipos espectrales desde F tardío hasta M intermedio, buscando tanto actividad a largo plazo (ciclos similares al ciclo solar) como a corto plazo (rotación). Presentamos nuevas medidas de ciclos magnéticos para 105 estrellas, y periodos de rotación para 123 estrellas. Estudiamos la distribución de periodos de rotación, donde encontramos una evolución hacia mayores valores en la duración del periodo en los tipos espectrales más tardíos. Esa evolución se detiene al llegar a las estrellas de tipo K temprano, y se reanuda al cruzar la frontera de las estrellas M2. Estudiamos así mismo la distribución de ciclos magnéticos, sin encontrar diferencias evidentes entre las estrellas de diferentes tipos espectrales.

Estudiamos la relación entre el periodo de rotación medido y el nivel medio de actividad cromosférica, medido como el $\log_{10}(R'_{\rm HK})$. Para ello extendemos la calibración del $\log_{10}(R'_{\rm HK})$ para cubrir estrellas de B-V hasta ∼2.0. Encontramos una fuerte correlación entre el periodo de rotación medido y el nivel de actividad cromosférica, que permite predecir el periodo de rotación de estrellas desde estrellas de tipo G hasta estrellas de tipo M intermedio de secuencia principal con una precisión del ∼23%.

Analizamos las curvas de velocidad radial de 133 estrellas buscando tanto señales de velocidad radial inducidas por actividad como señales inducidas por planetas. Detectamos la señal inducida por rotación en 46 estrellas, con amplitudes desde 0.3 hasta 16.4 m s^{-1}. Estudiamos la relación entre la amplitud de las señales inducidas y los indicadores de actividad cromosférica, encontrando una vez más una correlación entre el nivel medio de actividad $\log_{10}(R'_{\rm HK})$ y la amplitud de la señal inducida. Esta relación nos enseña que las estrellas FGK siguen un comportamiento similar, mientras que para las estrellas M las amplitudes inducidas son mayores. Encontramos también una relación entre la amplitud de la modulación rotacional del índice S_{MW} y la amplitud de la señal en velocidad radial inducida por la rotación. En este caso encontramos dos poblaciones bien diferenciadas, divididas por las estrellas de tipo K intermedio.

Tras limpiar las curvas de velocidad radial de señales inducidas por actividad llevamos a cabo una búsqueda de señales dinámicas en la misma muestra de estrellas. Recuperamos la mayor parte de los candidatos a planetas previamente publicados, salvo unos pocos casos donde atribuimos a la señal un origen intrínseco a la estrella. Presentamos el descubrimiento de seis nuevos planetas alrededor de las estrellas HD 1581, HD 161098, HD 176986, GJ 536 y GJ 3998, con masas mínimas de 5.87 ± 0.99, 26.60 ± 4.39, 4.86 ± 0.66 and 5.47 ± 0.84 $M_\oplus$, 2.35 ± 0.42 $M_\oplus$ y 6.12 ± 1.11 $M_\oplus$ respectivamente, situados a 0.321, 2.503, 0.061, 0.066, 0.029 y 0.089 au de sus estrellas. Los dos últimos publicados ya durante este año (Affer et al. 2016). Cinco de ellos probablemente sean planetas rocosos. Sugerimos también la presencia de un séptimo en la estrella HD 161098 con una masa mínima de 5.30 ± 1.22 $_\oplus$ orbitando a una distancia de 0.317 au, que podría ser habitable si se diesen las condiciones atmosféricas apropiadas. Sugerimos por último la presencia de cinco candidatos adicionales que aún requieren observaciones adicionales y un análisis detallado.

Summary

The search for exo-Earths using Doppler spectroscopy faces nowadays two main difficulties. The first is a technical limitation. The precision of the instruments limits the measurable amplitudes to signals produced by super-Earths orbiting close to their host stars. Terrestrial planets orbiting solar-type stars induce variations smaller than 1 m s^{-1} except when orbiting very close to the star. The arrival of ESPRESSO and the Laser Frequency Comb as calibration unit will palliate this limitation and move the measurement precision to the range of 5 cm s^{-1}. So far the search in solar-Type stars is limited to super-Earths. The alternative is to find terrestrial planets in the habitable zone is the search around M-type stars. Their lower mass makes the signals of terrestrial planets detectable by today's instruments.

The second issue is the presence of radial velocity variations induced by the homogeneities of the stellar surface. The changes in the stellar surface and the stellar rotation induce periodic signals that go from less than 1 m s^{-1} in the quietest stars to dozens of m s^{-1} in active stars and might be easily mistaken for signals induced by rocky planets. In the case of M-dwarfs the need of performing the analysis of the stellar induced signals is even more important. Signals produced by early M-dwarfs have periods compatible with the habitable zone of those stars and amplitudes similar to those of super-Earths. The rise in precision expected for the next years will make this kind of signals visible even in the quietest stars making even more important to understand and correctly model them.

Using chromospheric indicators from high resolution spectroscopic and photometric time series we study both long term and short term variability (solar-like cycles and rotation) of a sample of 176 low magnetic activity stars with spectral types going from late F-type to mid M-type stars. We provide new measurements of magnetic cycles for 105 stars, and rotation periods for 123 stars. We study the distribution of rotation periods, finding that there is an evolution in the rotation period lengths, getting longer for later type stars, that saturates when reaching K-type stars and begins to increase again at types later than M2. We study the distribution of magnetic cycles, finding no clear difference among different spectral types.

We study the relationships between the measured periods and the chromospheric activity level of the stars, measured as the $\log_{10}(R'_{\rm HK})$. To do so we extend the $\log_{10}(R'_{\rm HK})$ calibration to cover stars up to B-V $\sim$ 2.0. We find a strong correlation between the measured rotation period and the mean level of chromospheric activity that allows to predict the rotation periods of main sequence stars from G-type to mid M-type with an accuracy of the $\sim$ 20% of

the period.

We analyse the radial velocity time series of 133 stars searching both for activity induce signals and planetary signals. We detect rotation induced signals in 46 stars, with amplitudes going from 0.3 to 16.4 ms^{-1}. We study the relationship between the amplitude of the induced signals and the activity indicators, finding a correlation between the mean level of chromospheric activity $\log_{10}(R'_{HK})$ and the measured amplitude of the signal. This relationship shows that FGK stars show a similar behaviour, which is different for M-type stars. We find also a relationship between the amplitude of the modulation in the Mount Wilson S index and the amplitude of the induced radial velocity signal. This relationship behaves differently for two populations of stars, with a breaking point around mid-K stars.

After cleaning the radial velocity series form stellar activity induced signals we performed a search for dynamical signals in the same sample of stars. We recovered most of the previously published planet candidates, except for a few cases where we attribute a stellar origin to the previously assumed planetary companion. We present the discovery of six new planets around the stars HD 1581, HD 161098, HD 176986, GJ 536 and GJ 3998, with minimum masses in $M_\oplus$ units of 5.87 $\pm$ 0.99, 26.60 $\pm$ 4.39, 4.86 $\pm$ 0.66 and 5.47 $\pm$ 0.84, 2.35 $\pm$ 0.42 and 6.12 $\pm$ 1.11 respectively located at 0.321, 2.503, 0.061, 0.066, 0.029 and 0.089 au from their parent stars. The latter two have been reported by Affer et al. (2016). Five of them are presumably rocky planets. We suggest the presence of a seventh one in the star HD 161098 with a minimum mass of 5.30 $\pm$ 1.22 $M_\oplus$ located at 0.317 au of the star, which could be habitable given the appropriate atmospheric conditions. We suggest also the presence of five additional candidates that still require further analysis and observations.

Contents

List of Figures

List of Tables

1

Introduction

1.1 The search for exo-Earths

Since the dawn of civilization, humanity has been visualizing the possibility of other worlds, starting with pure speculation until reaching modern times when astronomical information flows in a way that has been never seen before. The search for planets outside our own Solar system traces back as far as the moment when the Earth was moved away from the center of the universe. By the XVII century the Italian philosopher Giordano Bruno already explicitly presented the idea that there must be other worlds similar to ours. He extended the Copernican model by proposing that the stars were distant suns surrounded by their own planets, which could even foster life of their own. He was also one of the first claiming that there was no such thing as a center of the universe.

"There are countless suns and countless earths all rotating round their suns in exactly the same way as the seven planets of our system. We see only the suns because they are the largest bodies and are luminous, but their planets remain invisible to us because they are smaller and non-luminous. The countless worlds in the universe are no worse and no less inhabited than our earth."

Giordano Bruno

Later, during the XVIII century, Sir Isaac Newton came back to that idea in the *General Scholium* that closes the 1713 edition of his *Principia*. He stated that the stars would not only might host other planets, but that if it were the case the rules of physics should be the same as in our solar system.

"And if the fixed Stars are the centers of other like systems, these, being form'd by the like wise counsel, must be all subject to the dominion of One; especially since the light of the fixed Stars is of the same nature with the light of the Sun, and from every system light passes into all the other systems. And lest the systems of the fixed Stars should, by their gravity, fall on each other mutually, he hath placed those Systems at immense distances from one another."

Sir Isaac Newton

It was not until the XIX century when the first claims of extrasolar planetary discoveries arose. The first case concerned the binary star 70 Ophiuchi. In 1855 Captain W.S. Jacob from the Madras observatory, property of the British East India Company, found orbital anomalies in the star which were probably caused by a planetary companion (Jacob 1855). Later in the decade of 1890 astronomers from the University of Chicago and the U.S. Naval Observatory asserted that the anomalies were evidence of the presence of a dark body in the system, with an orbital period of 36 years around both stars. That theory was soon discarded as the system would have been unstable given the theorised configuration. During the following years many claims of the discovery of extrasolar planets were made. Most of them were rapidly discarded, and the rest followed the same fate some time after. One of the most famous cases was the planetary system of Barnard's star.

Barnard's star (Barnard 1916) is an M-type star located at just 1.82 pc from the Sun with a very high proper motion. The study of its proper motion led Peter van de Kamp to propose the existence of two large mass planets orbiting the star by measuring the changes in the proper motion of the star (van de Kamp 1963). For many years there was a controversy on the existence of those planets, until it was finally attributed to an artefact of the maintenance of the telescope used.

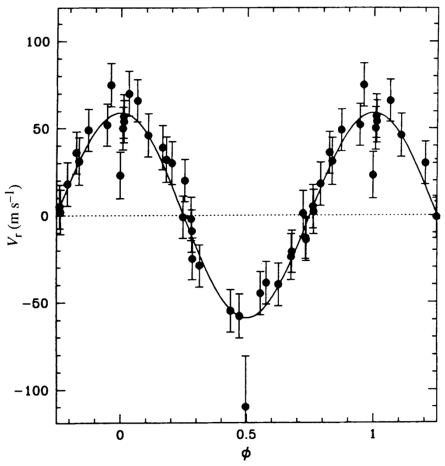

Figure 1.1: Phased radial velocity time series of 51 Pegasi

The first published claim that ended up being confirmed was the planet around Gamma Cephei Ab (Campbell et al. 1988), which could not be confirmed until many years later

(Hatzes et al. 2003) as the measurements were on the edge of the instrumental precision of its time. The first extrasolar planets whose existence could be demonstrated where the two planets orbiting the pulsar PSR 1257+12 (Wolszczan & Frail 1992). This discovery is considered to be the first definitive detection of an extrasolar planet. 51 Pegasi b (Mayor & Queloz 1995) was the first extrasolar planet discovered orbiting a main sequence star. Fig. 1.1 shows the radial velocity curve presented in the original article. This discovery is widely considered to be the starting point of the modern era of exoplanet science.

The technological advances of the following years led to the discovery of thousands of extrasolar planets. Many of the first discoveries were giant planets located very close to their parent stars, but soon smaller mass planets started to appear. Butler et al. (1999) reported the first multiplanetary system around Upsilon Andromedae and Lovis et al. (2011a) reported a 7 planets system around the star HD 10180. Rivera et al. (2005) presented the first terrestrial planet orbiting the star GJ 876 and Anglada-Escudé et al. (2016) discovered an Earth-sized planet in the habitable zone of our closest star, Proxima Centauri (Fig. 1.2).

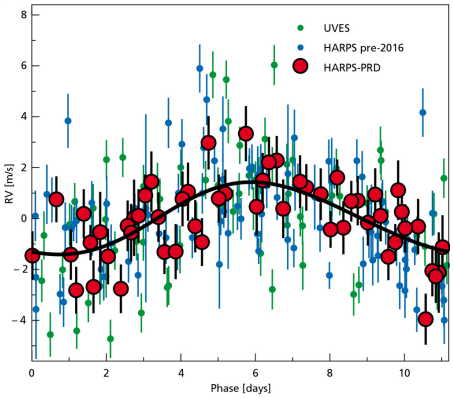

Figure 1.2: Phased radial velocity time series of Proxima published in Anglada-Escudé et al. (2016).

So far there are more than 3500 discovered exoplanet candidates in more than 2600 planetary systems. 246 of them are possibly rocky planets, smaller than 17 $M_\oplus$. Radial velocity surveys are able to measure signals smaller than 1 m/s (Pepe et al. 2011) and to detect planets as small as 1.3 $M_\oplus$ (Anglada-Escudé et al. 2016) while space transit missions can reach precisions of 29 ppm on a magnitude 12 star for a 6.5-hour integration and detect planets as small as 0.34 $R_\oplus$ (Barclay et al. 2013). Figure 1.3 shows the evolution of the discovery rate of exoplanets since 1995 up to 2016.

Nowadays it is estimated that the frequency of habitable planets around late type dwarfs is around $0.46^{+0.20}_{-0.15}$ (Gaidos 2013), and as time passes by and new discoveries come in the number only seems to increase.

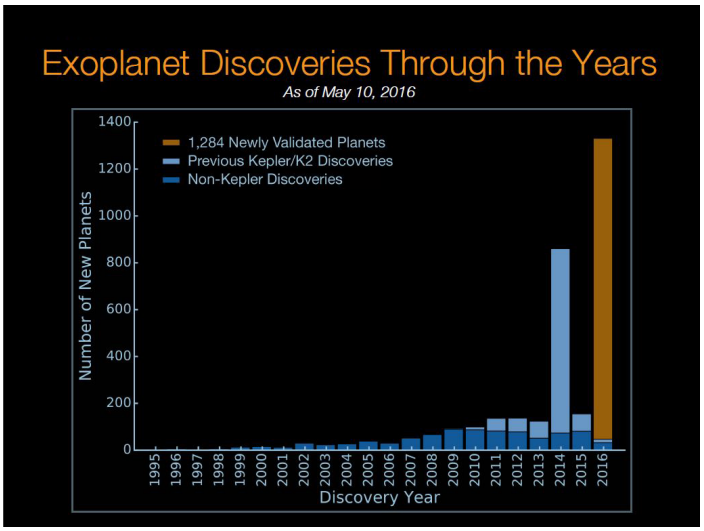

Figure 1.3: Number of new extrasolar planets discovered every year since 1995.

1.2 Techniques

Planets are very faint sources compared to their parent stars. The detection of most extrasolar planets is therefore performed trough indirect methods.

1.2.1 Doppler spectroscopy

A planet orbiting a star causes the center of mass of the system to be located away from the center of the star. This makes the star to move in a small orbit around the center of mass (typically located inside its radius). This small movement changes the velocity of the star in the line of sight of the Earth, i.e. its radial velocity changes. Measuring these small variations in the radial velocity it is possible to detect the presence of planetary companions. When the star velocity changes, the position of the spectral lines

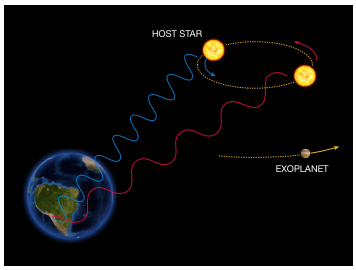

Figure 1.4: Blue-shift and red-shift of the light of the star as it moves around the center of mass of the system.

changes too by the Doppler effect. Moving to bluer wavelengths when the star moves towards us, and redder when the star moves away from us (Fig. 1.4). The measurement of the displacement gives the changes in the velocity. Finding periodic changes in the velocity of sufficient amplitude evidences the presence of an object orbiting around the star. From a radial velocity curve it is possible to obtain the parameters of the object orbiting around the star simply by studying the amplitude and the period by using Kepler's Third Law of planetary movement. In particular, the semi-amplitude of the radial velocity curve provides a determination of the minimum mass of the planet, $m_p\ sin(i)$, once the stellar mass of the host is known. The mass of the star is typically obtained from the determination of stellar parameters and metallicity and a comparison with model isochrones. This mass determination is accurate enough, especially for main-sequence stars, if the stellar parameters are known with high precision.

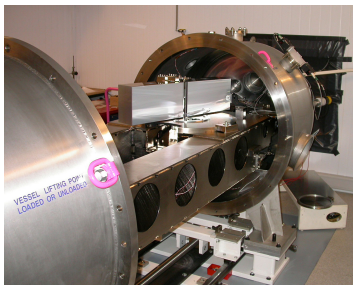

Figure 1.5: HARPS spectrograph.

The radial velocity signals induced by planets are usually of small amplitudes, specially those of rocky planets. The HARPS spectrograph was an important milestone moving the precision of the radial velocity measurements from under 10 m s^{-1} to under 1 m s^{-1}. ESPRESSO (Fig. 1.6) should achieve a similar step, going under 0.1 m s^{-1}. This should allow to detect earth sized planets in the habitable zones of solar type stars. Along with ESPRESSO comes the Laser Frequency Comb, a calibration unit with measured stability at photon noise level (Wilken et al. 2012).

The improvement in radial velocity precision will lead to the detection of smaller mass exoplanets, with masses smaller than the Earth in close orbits, and comparable to the Earth at Earth-like orbits., or in the habitable zone of their host stars.

Figure 1.6: The ESPRESSO spectrograph.

The importance of properly modelling activity induced signals for all the different stellar phenomenons becomes much more important the higher the instrumental precision gets. Moving from tens of m s^{-1} to 1 m s^{-1} made the measurement of the rotation and magnetic cycles of stars of moderate activity necessary.

Going below the 1 m s^{-1} precision requires the same even for the quietest stars. Being able to predict the stellar behaviour with just a few measurements becomes a key point for survey efficiency, while completely characterizing the stellar behaviour does the same in the analysis phase. Rotation, differential rotation, signals at the harmonics of both, global cycles, flip-flop cycles... Measure all of them and their effect in the radial velocity measurements is a necessary step in order to be able to find the smaller exoplanets that the improvements in technical precision allow.

This technique was the first to detect an extrasolar planet around a main sequence star, and remains among the most successful ones. Including outstanding discoveries like 51 Pegasi b (Mayor & Queloz 1995) and Proxima b (Anglada-Escudé et al. 2016). It is specially effective when the planet/star mass ratio is large and the planet stays at close orbits. This makes it specially effective for the detection of massive planets at close orbits and planets around small stars.

Radial velocity measurements can only provide a lower limit on the mass of the planet. The precise determination of the mass requires also the inclination angle of the orbit with respect to our line of sight. The worse the alignment of the orbit the smaller is the radial velocity amplitude generated by the same planet. Radial velocity measurements are frequently used to confirm the discoveries made by other methods or to determine the masses of planets discovered by the transit technique (see Section 1.2.2).

1.2.2 Transits

When a planet crosses between us and its star, blocking part of the emitted light, it is transiting its star. When this happens it is possible to measure the difference in the stellar luminosity and infer which kind of object is causing the dip (Fig. 1.7). This allows for planet detection and characterization.

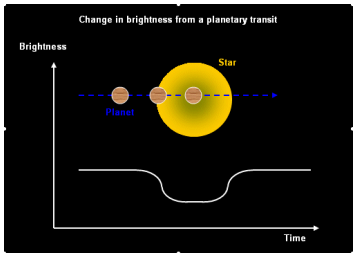

Figure 1.7: Light curve of a star during a transit.

While the radial velocity technique gave information about the mass of the planet, transit measurements can determine the radius, as the dip in brightness depends on the planet/star radius ratio. Combining transit measurements with radial velocity measurements allows for a complete characterization of the planet, including the determination of important physical parameters.

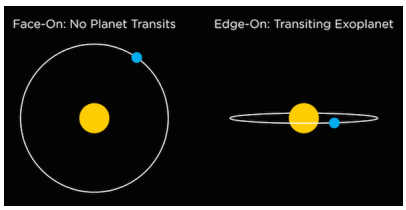

Figure 1.8: Effect of the alignment. Edge-on alignments allow for transits. Everything else, up to face-on, does not.

The transit technique also allows to characterize the atmospheric conditions of the planet. While the planet is transiting the light of the star goes through the upper layers of its atmosphere, allowing to measure its composition.

A drawback is that the probability for a planet to transit is very small. Specially at larger orbital separations. It requires a nearly perfect alignment between the orbital plane and the line of sight of the Earth (Fig. 1.8). For close orbits the probability might reach up to 10%, but the further away we move the smaller the probability is. High precision photometric monitoring of large areas of the sky, containing thousands of stars, may detect planetary companions outpacing any other method. This has been the strategy of space observatories as COROT and Kepler.

1.2.3 Transit-timing variations

For planetary systems with multiple planets it is possible to detect the presence of additional planets by measuring the changes of the time of the transit. By observing multiple transits it is possible to measure the orbital period of the planet and the transit length. The dynamical interaction between the planets might affect the orbit of the detected planet making the measured orbital period and transit length unstable.

Eclipsing binaries

An eclipsing binary is a system that is aligned to the line of sight to the Earth in a way that the stars eclipse each other. The timing of the eclipses is usually extremely regular, making any perturbations easy to spot. A planet orbiting such binary system will move the center of masses of the system, changing the light travel time. This change in the light travel time will cause an apparent change in the timing of the eclipses, revealing the presence of a planet.

1.2.4 Pulsar timing variations

A pulsar is a neutron star, the extremely dense and small remnant of a massive star that has exhausted its nuclear fuel. This kind of bodies rotate at very

high rates, and emit extremely regular radio pulses. The intrinsic regularity of the pulse emission makes it very easy to detect anomalies in the period of the pulses, and therefore detect the pulsar movement.

As in the case of an ordinary star a pulsar will move around the center of mass of the system when accompanied by other bodies. This motion alters the detected pulses, allowing for the detection of the planet. This was not intended to be a method for detecting planets, but its sensitivity is so high that allows for the detection of very small planets, even smaller than the Earth. It is even capable of detecting the gravitational interaction between them, giving information about the parameters of the whole system.

The drawback is that pulsars are rather rare objects and therefore there are not many planets detectable by this technique. Also life, as we know it, is unlikely to exist in this kind of planets because of the high energy radiation they receive.

1.2.5 Gravitational microlensing

When the gravitational well of a star acts as a lens, magnifying for a short time span the light of a star located behind it, we have what is called a gravitational micro-lens. When the star that is causing the micro-lens has a planet, the gravity well of the planet can contribute to the effect of the lens in a detectable way (Fig. 1.9).

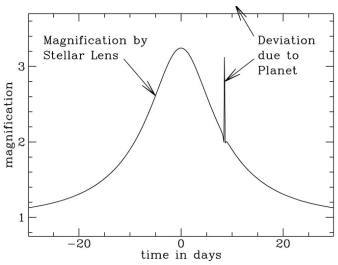

Figure 1.9: Shape of a microlensing event.

The alignment required for this phenomenon is very improbable, which makes it very hard to study with repeated measurements. This effect is usually detected by observing big areas of the sky, including thousands of stars.

This technique has been particularly successful finding planets located between our solar system and the central region of the Galaxy, because of the large number of observable stars and the large number of possible alignments. Planets detected by this technique are usually very far from us, implying it is very hard to confirm the discoveries by any other technique. On the other hand it is one of the techniques with greater potential for finding planets located beyond the snowline.

1.2.6 Astrometry

This technique consists in the precise measurement of the position of the star in the sky and its change in time. In the case of the star having a planet the gravitational pull of the planet will make the star move in a small circular orbit around the center of mass of the system (Fig. 1.10).

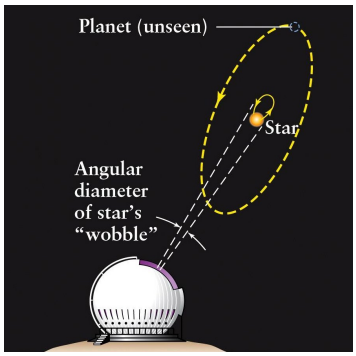

Figure 1.10: Movement of the star around the center of masses of the system.

Astrometry is the oldest technique in the search for extrasolar planets. Very much used in the early days because of its success characterizing binary stars. It goes back to the late XIX century, when claimed that an invisible body was affecting the position of the star 70 Ophiuchi. From then on, hundreds of claims were made about invisible companions affecting the orbits of nearby stars, but none of them could ever be confirmed. The expected changes in the position of the star caused by planetary companions are very small, of the order of *mili*-arcseconds and thus the distortions caused by the Earth's atmosphere and the instrumental uncertainties are big enough to bury them in the noise. Up to this point no planets have been discovered by this technique, although it was possible to characterize a planet discovered in GJ 876 using the Hubble Space Telescope (Benedict et al. 2002).

This technique is expected to be very sensitive to the movement caused by planets at long orbits, thus it could be very valuable complementing radial velocity and transit survey. The spacecraft GAIA (Global Astrometric Interferometer for Astrophysics) is expected to create an extremely precise 3D catalogue of the motion of over 1 billion stars with an accuracy of 20 μ-arcseconds. With its precision it is expected to detect thousands of Jupiter-sized planets.

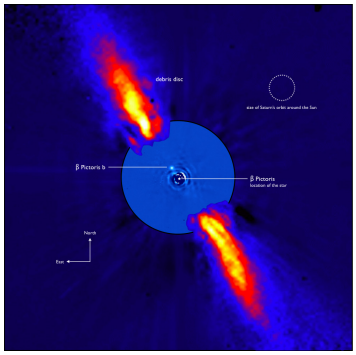

Figure 1.11: Image of Beta Pictoris with its planet.

1.2.7 Direct imaging

Planets reflect the light of their stars. Although planets are very faint sources compared to their stars and it is very hard to detect them, combining adaptive

optics and coronography masking of the stars may provide direct imaging in the near infrared of planets located at large orbital separations.

A remarkable case is Beta Pictoris b (Lagrange et al. 2009), detected by direct imaging with the 8.2m Very Large Telescope at the Observatorio de Paranal (ESO, Chile) (Fig.1.11).

1.3 Planet statistics

So far more than 3500 extrasolar planets have been found, one third of them could be super-Earths or Earth-like planets with masses below 10 $M_\oplus$ or radius below 4 $R_\oplus$.So far 351 Earth-sized (mass $<$ 1.9 $M_\oplus$ and radius $<$ 1.25 $R_\oplus$) planets and 847 super-Earths (1.9 $<$ mass $<$ 10 $M_\oplus$ and 1.25 $<$ radius $<$ 2 $R_\oplus$) have been discovered. They make a total of 1198 planets distributed in 910 planetary systems, 201 of those systems being multi-planetary systems. Every year it becomes more clear that rocky planets are the most abundant population around late-type dwarfs.

The statistic derived from the results of the Kepler mission shows that occurrence of planets at close orbits increases towards smaller radius planets, and also towards lower mass stars (Howard et al. 2012), as can be seen in Fig. 1.12. Gaidos (2013) estimated that the frequency of habitable rocky planets is $0.46^{+0.20}_{-0.15}$ on a wide spectral sample of Kepler dwarfs, which is consistent with the results of the HARPS survey that estimated that 50% of solar-like stars harbour at least one low mass ($<$ 50 $M_\oplus$) planet (Mayor et al. 2011). Petigura et al. (2013) estimated an occurrence rate of Earth-size planets in the habitable zones of Sun-like stars of the 22%, and a 26% at periods shorter than 100d.

1.3.1 M-Dwarfs

Several surveys have attempted to take advantage of the low masses of M-dwarfs (Fig. 1.13) – and therefore of the stronger radial velocity signals induced for the same planetary mass companions – and closer habitable zones to detect rocky habitable planets (Bonfils et al. 2013; Howard et al. 2014; Irwin et al. 2015; Berta-Thompson et al. 2015; Affer et al. 2016). While surveying M-dwarfs has advantages, it also has its own drawbacks. Stellar activity has been one of the main difficulties when trying to detect small planets trough Doppler spectroscopy. Not only it introduces noise, but also coherent signals

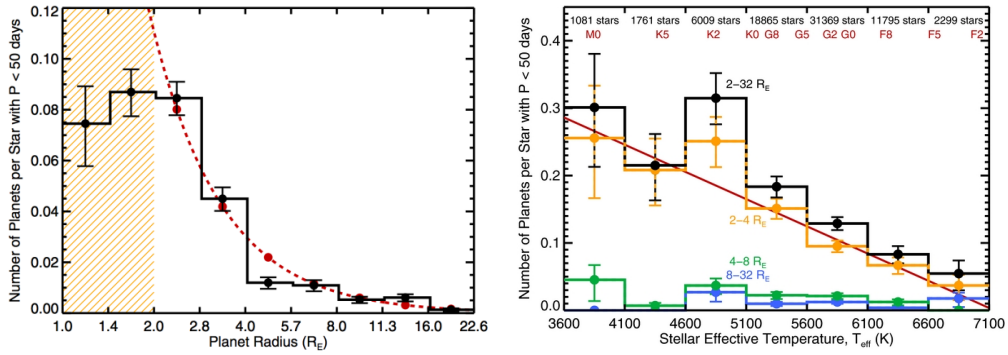

Figure 1.12: Occurrence of planet as a function of planet radius (left panel) and spectral type (right panel) according to Howard et al. (2012).

that can mimic those of planetary origin (Queloz et al. 2001; Bonfils et al. 2007; Robertson et al. 2013). The magnetic activity of M-dwarfs tend to induce radial velocity signals with amplitudes comparable to those of rocky planets (Howard et al. 2014; Robertson et al. 2013). While these kind of stars allow for the detection of smaller planets, they also demand a more detailed analysis of the radial velocity signals induced by activity. In addition this low mass stars offer valuable complementary information on the formation mechanisms of planetary systems. For instance giants planets are known to be rare around M dwarfs, while on the other hand super-Earths appear to be more frequent (Bonfils et al. 2013; Dressing & Charbonneau 2013; Dressing et al. 2015) than in solar-like stars.

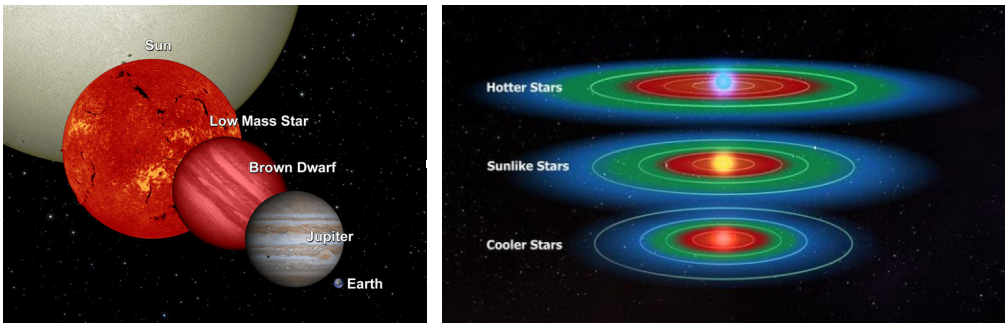

Figure 1.13: Relative size of a low mass star compared to the Sun and habitable zones of the stars for different spectral types. The lower the temperature the closer to the star the HZ moves

The first discovery of a planet around an M-dwarf dates back to 1998

(Delfosse et al. 1998; Marcy et al. 1998), in the star GJ 876. Since then several planetary systems have been reported containing Neptune mass planets and super-Earths (Udry et al. 2007; Delfosse et al. 2013; Howard et al. 2014; Astudillo-Defru et al. 2015) even some Earth-mass planets (Mayor et al. 2009b; Berta-Thompson et al. 2015; Wright et al. 2016). However the frequency of very low-mass planets around M-dwarfs is not well established yet. In particular, as noted by Bonfils et al. (2013), the frequency of rocky planets at periods shorter than 10 days is $0.36^{+0.24}_{-0.10}$, being $0.41^{+0.54}_{-0.13}$ for the habitable zone of the stars. On the other hand Gaidos (2013) estimated that the frequency of habitable rocky planets is $0.46^{+0.20}_{-0.15}$ on a wider spectral sample of Kepler dwarfs and Kopparapu (2013) gave a frequency of $0.48^{+0.12}_{-0.24}$ for habitable planets around M-dwarfs. The three measurements are compatible, but uncertainties are still big making it important to continue the search for planets around this type of stars in order to refine the statistics.

1.4 Stellar Activity

It is widely recognised that starspots on late-type dwarf stars lead to periodic light variations associated with the rotation of the stars Kron (1947). Starspots trace magnetic flux tube emergence and provide valuable information on the forces acting on flux tubes and photospheric motions, both important agents in the dynamo theory (Parker 1955; Steenbeck et al. 1966; Bonanno et al. 2002). Rotation plays a crucial role in the generation of stellar activity (Skumanich 1972). This becomes evident from the strong correlation of magnetic activity indicators with rotation periods (Pallavicini et al. 1981; Walter & Bowyer 1981; Vaughan et al. 1981; Middelkoop et al. 1981; Mekkaden 1985; Vilhu 1984; Simon & Fekel 1987; Drake et al. 1989; Montes et al. 2004; Dumusque et al. 2011, 2012; Suárez Mascareño et al. 2015).

Stellar rotation coupled with convective motions generate strong magnetic fields in the stellar interior and produce different magnetic phenomena, including starspots in the photosphere. Big spotted areas consist of groups of small spots whose lifetime is not always easy to estimate, but the main structure can survive for many rotations, causing the coherent brightness variations that we can measure (Hall & Henry 1994). In solar-like main-sequence stars the light modulations associated with rotation are of order a few percent (Dorren & Guinan 1982; Radick & Lockwood 1983), while in young fast rotating stars these modulations can be significantly larger (Frasca et al. 2011). Starspot induced light modulation was also proposed for M dwarfs decades ago (Chugainov

1971) and more recently investigated by, for example, Irwin et al. (2011), Kiraga (2012) and West et al. (2015).

Stellar induced radial velocity variations come mainly from two different sources. First, stellar spots are cooler and radiate less than other regions of the stellar photosphere, thus affecting the photospheric line profiles and therefore the RV measurements. This effect changes as the star rotates. Then stellar magnetic activity creates regions in which the convective currents are altered, thereby changing the ingoing or outgoing flux of material in parts of the star's surface (Dumusque et al. 2014). The position and distribution of these spots and magnetically active regions is strongly dependent on the long term magnetic cycle of the star, so it usually extends over more than a few rotational periods. The second effect produces an apparent change in the radial velocity of the star that becomes more important in later stellar types (Robertson et al. 2014), but it also results in a change in the intensity of the chromospheric emission lines. Since we integrate the whole light of the visible side of the star, the observed fluxes of the lines change with stellar rotation. Measuring these flux variations in spectroscopic time series of chromospheric lines can therefore reveal the rotation period of a star (Dravins et al. 1981; Dravins 1982; Livingston 1982; Brandt & Solanki 1990; Donahue et al. 1996; Lindegren & Dravins 2003; Meunier et al. 2010; Lovis et al. 2011b; Howard et al. 2014). This has been possible even for stars of very low activity (Dumusque et al. 2012; Robertson et al. 2014).

Magnetic activity influences spectral lines (Dravins 1985) and produces inhomogeneities in the stellar surface, which, combined with rotation, causes Doppler shifts of the stellar spectrum (Saar & Donahue 1997). Changes in the distribution of spots induce apparent Doppler shifts from less than one to dozens of metres per second, depending on the level of stellar activity (Huélamo et al. 2008; Pont et al. 2011; Hatzes 2013). When these induced signals are periodic, they could be mistaken for planetary signals. In fact, stellar activity is one of the most important causes of false alarm signals in the analysis of high precision RV time series. Disentangling these signals from a real planetary signal in RV curves is a crucial issue when searching for terrestrial exoplanets. Since the exoplanet community started to search for small planets there has always been a concern that the intrinsic variability of the stellar surface (Baliunas et al. 1997) could render impossible the detection of the low amplitude radial velocity signals caused by terrestrial planets (Queloz et al. 2001; Dumusque et al. 2012; Santos et al. 2014). The precise determination of the rotation periods of stars is a crucial first step in discriminating true planetary signals from those induced by the stellar activity.

A well-known connection between stellar activity and rotation has been

widely used to estimate rotation periods through stellar models (Skumanich 1972; Catalano & Marilli 1983; Baliunas et al. 1983). Rotation periods have usually been measured from periodic variations in the stellar luminosity associated with the distribution of superficial magnetic spots. These surface structures are sufficiently stable in time to span longer than the rotation period of the star (Robertson et al. 2015) and to make possible the measurement of stellar rotation periods from extensive photometry time series (Messina & Guinan 2002; Kiraga & Stepien 2007). However, these photometric variations are not always strong enough to be detected in stars of very low activity where many RV searches have been performed.

Long-term magnetic activity similar to that of the Sun is also observed on stars with external convection envelopes (Baliunas & Vaughan 1985; Radick et al. 1990; Baliunas et al. 1996; Strassmeier et al. 1997; Lovis et al. 2011b; Savanov 2012; Robertson et al. 2013). Photometric and spectroscopic time series observations over decades have revealed stellar cycles similar to the 11 yr solar magnetic cycle (Fig. 1.14). In some active stars even multiple cycles are often observed (Berdyugina & Tuominen 1998; Berdyugina & Järvinen 2005). It is possible to distinguish between cycles that are responsible for overall oscillation of the global level of the activity (similar to the 11 yr solar cycle) and cycles that are responsible for the spatial rearrangement of the active regions (flip-flop cycles) at a given activity level, such as the 3.7 yr cycle in sunspots (Berdyugina & Usoskin 2003; Moss 2004). The correct understanding of the different types of stellar variability, their relationships, and their link to stellar parameters is a key aspect to properly understand the behaviour of the stellar dynamo and its dependence on stellar mass. While extensive work has been conducted in FGK stars over many decades, M dwarfs have not received so much attention with only a few tens of long-term activity cycles reported in the literature (Robertson et al. 2013; Gomes da Silva et al. 2012).

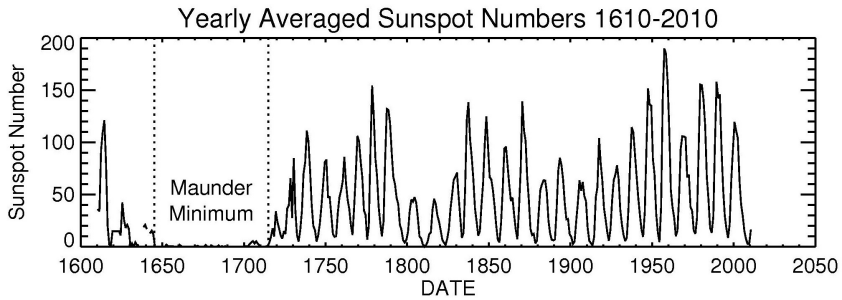

Figure 1.14: Long term measurements of Sunspots

Understanding the full frame of stellar variability in stars with a low level of activity is also crucial for exoplanet surveys. Modern spectrographs can now reach sub ms^{-1} precision in the radial velocity measurements (Pepe et al. 2011) and next generation instrumentation is expected to reach a precision of a few cm s^{-1} (Pepe et al. 2013). At such precision level, the stellar activity induced signals in the radial velocity curves become a very important limiting factor in the search for Earth-like planets. Activity induced signals in timescales of days associated with rotation and in timescales of years for magnetic cycles are two of the most prominent sources of radial velocity induced signals (Dumusque et al. 2011). Measuring and understanding this short-term and long-term variability in different types of stars and the associated effects in radial velocity curves, and being able to predict the behaviour of a star, is required to disentangle stellar induced signals from Keplerian signals.

1.4.1 Signals induced by stellar activity

High precision radial velocity measurements give astronomers the possibility of detecting small planets, reaching Earth size. Unfortunately the technique is not sensible only to the motion of a star around the center of mass of a star/planet system. Intrinsic variations on the stellar surface induce radial velocity variations, which in some cases, when they produce a periodic signal over a few rotational period, can mimic a planetary signal. Recognizing and understanding them is one of the key points to be able to disentangle them from the planet induced signals (Queloz et al. 2001; Dumusque et al. 2012; Santos et al. 2014).

The nature of these signals depends mainly in two parameters. The activity level of the star and its spectral type. More active stars usually rotate faster, inducing shorter period signals with bigger amplitudes, but the amplitude depends also on the strength of the magnetic field, which is a function of the spectral type as it depends strongly on the depth of the convective zone (Saar & Donahue 1997; Noyes et al. 1984; Santos et al. 2000).

The amplitude of the so-called radial velocity jitter has already been explored in the past (Santos et al. 2000) but taking advantage of the precision obtained with HARPS (going below 1 ms^{-1}) we will investigate and characterize this jitter as a signal, measuring its period and amplitude even in multi-planetary systems. We then explore the presence of the harmonics of the rotation in the time series (Boisse et al. 2011) and the relationships between the measured amplitudes and the level of chromospheric emission measured as the $\log_{10}(R'_{\rm HK})$ and with the amplitude of the signals measured in the variations of the chromospheric emission.

Those signals with periods very compatible to the measured rotation and/or differential rotation, their harmonics and magnetic cycles must be carefully studied, as could be mistaken as Keplerian signals.

1.5 Objectives

The main goal of this PhD thesis is to search for rocky planetary companions in late-type dwarfs using high precision radial velocity time series. In order to be able to accurately detect the planets it will be necessary to perform a study of the chromospheric activity of a large sample of moderate to low activity late type main sequence stars and determine its effect on the radial velocity time series of the studied stars.

Using spectroscopic and photometric time series spanning, in many cases, more than 10 years ,we will search for the rotation and magnetic cycles of a set of late type dwarfs (from late F to mid M). We will study the distribution periods and the relations with the classic chromospheric activity indicator $\log_{10}(R'_{\rm HK})$.

Using the information about the stellar behaviour we will study the radial velocity signal induced by stellar activity, mainly by stellar rotation but also by long-term cycles, and study their distribution and relationship with chromospheric activity indicators.

Finally we will do a search for planetary companions on our sample of stars using all the knowledge acquired during the previous studies to disentangle planetary induced signals from stellar induced signals at the level of 1-2 m s^{-1} and below.

2

Sample and data

In this chapter we describe the different kinds of data used in the following chapters as well as the sample of stars that has been studied. This thesis research has been based mainly on HARPS and HARPS-N spectra to study the stellar activity, to characterize activity signals trough activity indicators and induced radial velocities and to search for low-mass exoplanets performing high precision radial velocity measurements. As support data for the activity diagnosis and calibrations I relied in the photometry from the All Sky Automated Survey and in the recently released S_{MW} index data from the Mount Wilson HK Project. We then present the catalogue used for all the analysis. It was built-up by combining new observations with data from different public archives to improve the statistical significance of the sample by extending it along all the different axis of the parameter space. The final catalogue includes stars covering from F to mid M dwarfs from the northern and southern hemispheres.

2.1 Sample

The following study about stellar activity and exoplanet hunting has been performed over a sample of 200 late-type dwarf stars, going from F to mid M-type, being early M-type stars the most abundant part. The sample is composed of stars with previously known planets and stars with no published planets. The sample of stars is defined by joining new observations with data from public archives such as the HARPS archive at the European Southern Observatory (ESO). This can be described as the combination of three different samples from two new observational programs and one conformed with stars with data in public archives.

2.1.1 The HADES RV program – Northern M-dwarfs

A collection of 80 early M-dwarfs (M0-M3) from the northern hemisphere selected from the Lépine & Gaidos (2013) catalogue. With visible magnitudes going from 8 to 12. Stars are located at declinations from 0^o to $+90^o$, being most of them around $\sim +30^o$. This sample was designed to maximize the possibilities of finding small rocky planets in the habitable zones of these stars with radial velocity monitoring with HARPS-N and therefore is biased towards low activity stars.

2.1.2 The equatorial GK-type stars program

It is a small sample of 15 equatorial G and K type stars with available observations in the HARPS public database and magnitudes brighter than m_V 9. These stars are located at declinations from $\sim$ -20^o to $\sim +20^o$. This sample was designed to maximize the possibilities of finding rocky planets in close orbits around them, with radial velocity monitoring with both HARPS and HARPS-N. Again it is biased towards stars of low activity.

2.1.3 Public archives

To increase the completeness of the sample and to compensate for the biases introduced in the two previous samples, we add a selection of stars with available data from the HARPS public database and the All Sky Automated Survey (ASAS) public archive. The data is completed with support data coming from the recent data release of the Mount Wilson HK Project, used for calibration purposes.

2.1.4 The complete sample

The full selection consists of 228-late type stars from the solar vicinity, going from the nearest star (Proxima Centauri) to stars at a distance of 70 pc, covering from mid F-type to mid M-type stars, with apparent magnitudes m_V in the range 4–13, plus 6 more stars of A and early F-type used only as calibrators. Figure 2.1 shows the distribution of spectral types. The sample is dominated by early M-dwarfs, as those are the largest population in the solar vicinity. The B-V colour of the stars go from bluer than 0.5 up to redder than 2 with most of the intervals adequately covered. The least populated regions are the F-type and late K-type stars. A small number of A-type and early F-type stars have been included only for calibration purposes. These stars are excluded from the analysis ofradial velocities, spectral indicators and photometry. Out of the

228 stars, a sub-sample of 133 stars that have more than 30 spectra combining HARPS and HARPS-N measurements will be used to study the radial velocity variability. To study the stellar activity another sub sample of 176 stars that includes those 133 stars plus 43 more that do not have enough spectra, but have good quality photometry. The remaining stars will be used for calibration purposes and to measure mean activity levels.

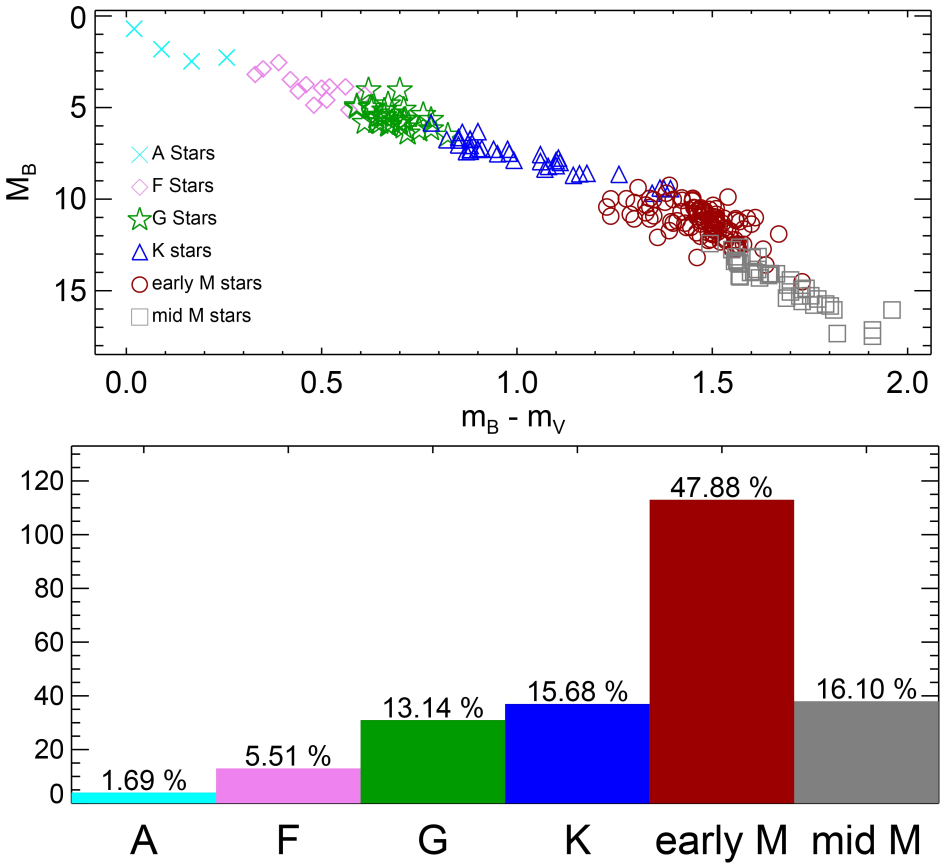

Figure 2.1: Spectral distribution of the complete sample. Upper panel shows the color magnitude diagram, lower panel shows the fraction of stars of each spectral type.

The sample described before cover the right ascension axis in an almost homogeneous way, while in declination most stars accumulate around the equator. Most of the stars in the sample are very nearby stars, peaking at distances smaller than 10 pc. Only a handful are located beyond 40 pc. Observations

have been performed in middle-size telescopes, such as the 3.6m ESO Telescope and the Telescopio Nazionale Galileo, at very high spectral resolving power making it very hard to go beyond m_V greater than 13. This makes it difficult to include distant dwarf stars of the desired spectral types. Most of the stars show metallicities close to solar. This is not surprising considering all of them are located in the solar vicinity. Figure 2.2 shows the distribution of coordinates, distances and metallicities of the sample.

While the selection is far from being a volume limited unbiased sample, it represents well enough the population of the solar vicinity to draw some conclusions from it and adequately covers the whole sky. The bias for low activity stars is unavoidable as we rely in data from planet-hunting programs, but it makes the sample more appropriate to draw conclusions for future planet-hunting programs. As for the study on magnetic cycles, the large population of M-dwarfs, specially mid M-dwarfs, makes it specially interesting, as cold stars have been historically less studied. Table 2.1 shows relevant data for a all the stars for which we present planetary detections. Appendix A.1 shows the relevant data for all the stars in the sample.

Table 2.1: Relevant information for a selection of the stars of our sample. Full table in Appendix A.1

Star	Sp. Type	m_B	m_V	$T_{\rm eff}$ (K)	Mass ($M_\odot$)	[Fe/H] (dex)	Dist. (pc)
HD 1581	F9.5	4.80	4.23	5977	1.0	-0.18	8.6
HD 161098	G8	8.31	7.67	5560	0.82	-0.27	30.2
HD 176986	K2.5	9.39	8.45	5018	0.73	0.00	26.4
GJ 536	M1	11.18	9.71	3685	0.52	-0.08	10.1
GJ 3998	M1	12.34	10.83	3722	0.50	-0.16	17.8

References for spectral types: Gray et al. (2006), Houk & Swift (1999), Stephenson (1986)
References for photometry:Ducati (2002),Høg et al. (2000), Koen et al. (2010)
References for temperatures, masses & metallicities: Sousa et al. (2008), Maldonado et al. (2015), Affer et al. (2016)
References for distances: van Leeuwen (2007)

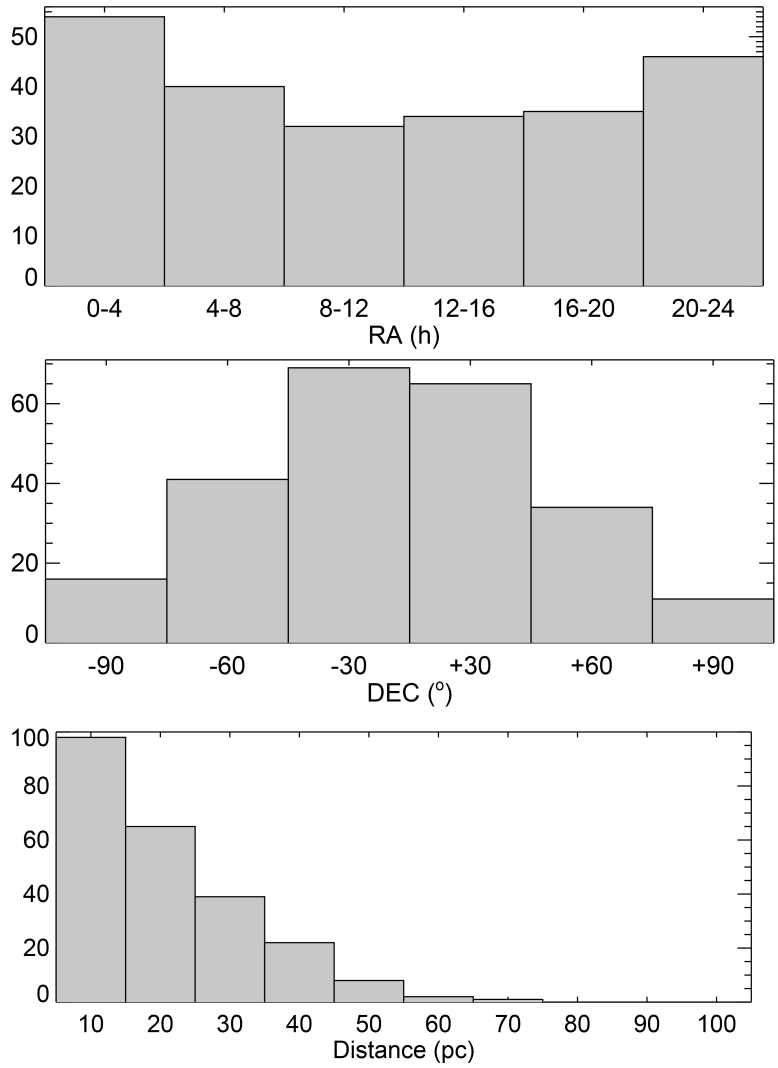

Figure 2.2: Distribution of coordinates of the targets (top and middle panels), and of distances of the targets (bottom panel).

2.2 Data and Observations

2.2.1 Spectroscopic data - HARPS and HARPS-N

The spectra for the northern M-dwarf program and the equatorial GK-type stars were taken with HARPS-N at the 3.6m Telescopio Nazionale Galileo (TNG) in the Observatorio del Roque de los Muchachos. The Observatorio del Roque de los Muchachos is one of the two astronomical observatories of the Canary Islands. It is located in the island of La Palma (Fig. 2.3), at an altitude of ∼2400 metres. It belongs to the Instituto de Astrofísica de Canarias (IAC) and was inaugurated in 1985. It hosts a number of large telescopes, such as the Gran Telescopio de Canarias (GTC), the William Herschel Telescope (WHT) or the Telescopio Nazionale Galileo (TNG).

The TNG is a 3.6 m telescope operated by the Fundación Galileo Galilei, a non-profit institution of the Italian National Institute of Astrophysics (INAF). It has a design derived from the New Technology Telescope (NTT), an ESO 3.5-meter telescope located at La Silla (Chile). The telescope saw first light in 1998 and is named after the Italian Renaissance astronomer Galileo Galilei.

The northern M-dwarf program started in the late 2012 and the equatorial GK-type stars program in the summer of 2014. Both programs are still ongoing, and altogether have acquired more than 4500 spectra of 110 stars in the course of 150 nights.

Figure 2.3: The TNG telescope right after opening the dome (left panel) and the location of the Observatorio del Roque de los Muchachos (right panel).

The HARPS data have been acquired by different groups on the course of more than ten years. HARPS is a high resolution ultra-stable echelle spectrograph operating at the 3.6m ESO telescope in the Observatorio de La Silla. The Observatorio de La Silla is located in the outskirts of the Atacama Desert (Chile). It is the oldest ESO observatory in Chile and one of the largest in the Southern Hemisphere (Fig. 2.4). Apart from the ESO 3.6 m telescope it

hosts other telescopes such as the New Technology Telescope (NTT), the Max Planck Gesellschaft (MPG) 2.2 m telescope or the Euler Telescope.

Figure 2.4: The ESO 3.6m Telescope behind the NTT (left panel) and the location of the Observatorio de La Silla (right panel).

HARPS (Mayor et al. 2003) and HARPS-N (Cosentino et al. 2012) are two fibre-fed high resolution echelle spectrographs installed at the 3.6 m ESO telescope in the Observatorio de la Silla (Chile) and at the Telescopio Nazionale Galileo in the Observatorio del Roque de los Muchachos (Spain), respectively. Both instruments have a resolving power greater than $R \sim 115\,000$ over a spectral range from ∼380 to ∼690 nm and have been designed to attain very high long-term radial velocity accuracy. Both are contained in vacuum vessels to avoid spectral drifts due to temperature and air pressure variations, thus ensuring their stability. HARPS and HARPS-N are equipped with their own pipeline providing extracted and wavelength-calibrated spectra, as well as RV measurements and other data products such as cross-correlation functions and their bisector profiles. Figure 2.5 shows an order of a spectrum of the HARPS first light.

HARPS and HARPS-N radial velocities can be measured with a long term stability of 1 m s^{-1} without the use of a simultaneous calibration. But it also has a second fiber that allows for a simultaneous calibration helping to decrease that factor an order of magnitude. Most of the observations of stars brighter than $m_V < 10.5$ were carried out using a Thorium-Argon (ThAr) lamp or a Fabry Perot (FP) as simultaneous calibration.

The ThAr lamp (Fig. 2.6) allows for the monitoring of the instrumental drift with a precision of 20 cm s^{-1} (Lovis & Pepe 2007). It has proven extreme long term stability over time. The ThAr lamp has the disadvantage of producing saturated lines in the blue part of the spectra. This diminishes its usability for M-dwarfs, which are specially faint in that region, for the risk of contamination of the stellar spectrum.

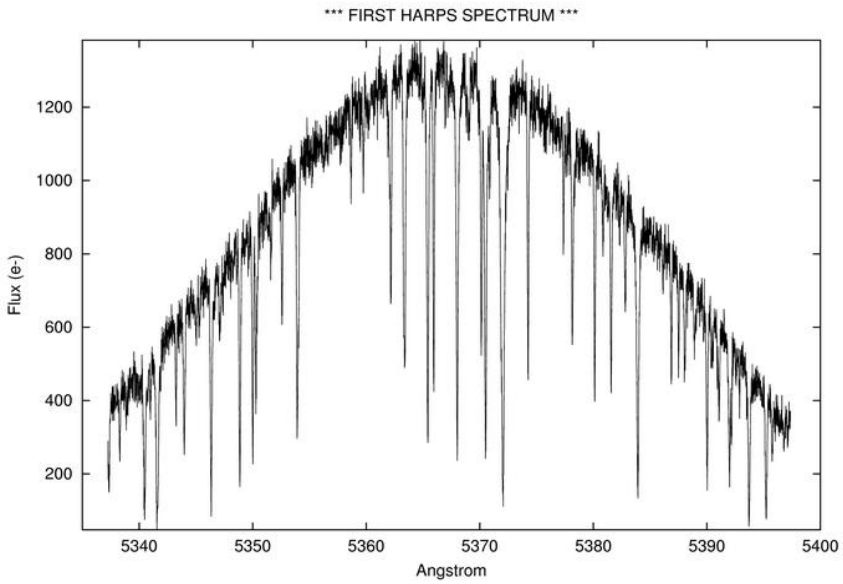

Figure 2.5: Individual order of the spectrum of HARPS first light.

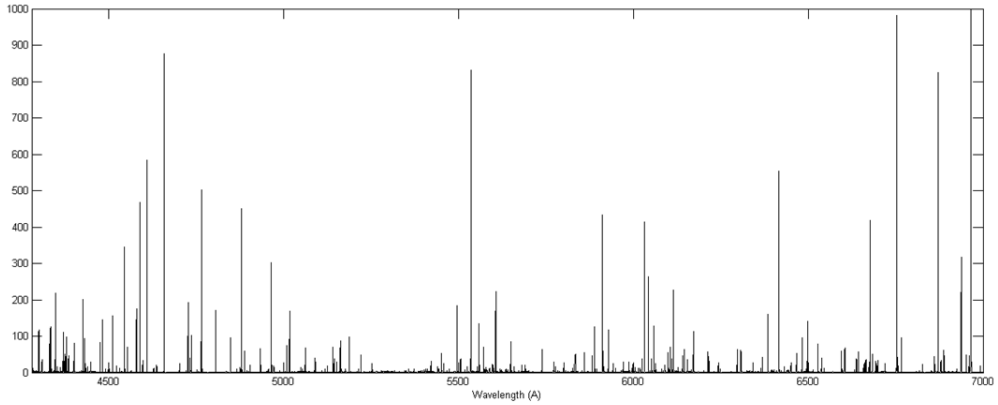

Figure 2.6: Spectrum of the ThAr lamp.

The new Fabry Perot (Fig. 2.7) offers the possibility of monitoring the instrumental drift with a precision of 10 cm s^{-1} without the risk of contamination of the stellar spectra by the ThAr saturated lines (Wildi et al. 2010). While this

is not usually a problem in G and K stars, the small amount of light collected in the blue part of the spectra of M-dwarfs might compromise the quality of the measurement of the Ca II H&K flux. The FP allows a precision of ~ 1 m s^{-1} in the determination of the radial velocities of the spectra with highest signal to noise while assuring the quality of the spectroscopic indicators even in those spectra with low signal to noise. Measurements of M-dwarfs taken before the availability of the FP were taken without simultaneous reference.

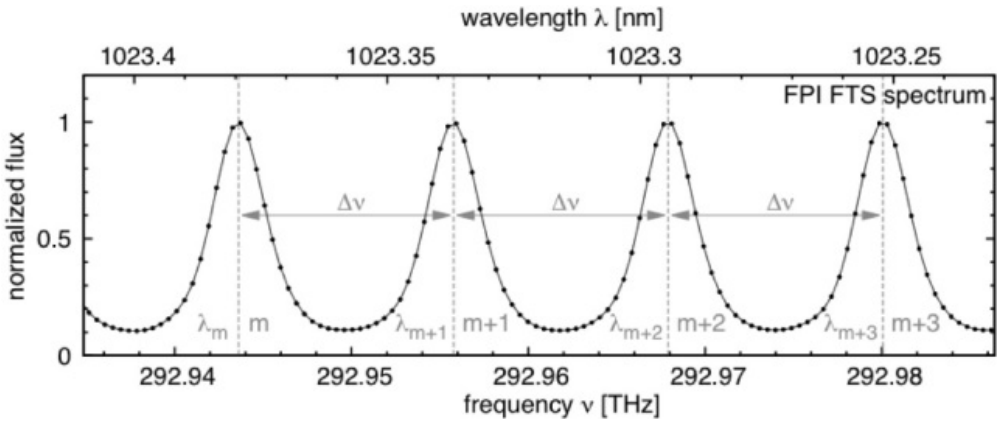

Figure 2.7: Fragment of the spectrum of a Fabry Perot calibrator unit.

For faint stars the second fibre is pointed at the sky in order to clean the spectra from possible sky contamination.

Observations are carried out with a typical exposure time of 900 seconds per visit, to average out the stellar p-modes. In the case of the GK stars each visit is split in 3 individual exposures to avoid any risk of saturation. For our analysis we use the extracted order-by-order wavelength-calibrated spectra produced by the HARPS/HARPS-N pipeline. For a given star, the change in atmospheric transparency from day to day causes variations in the flux distribution of the recorded spectra that are particularly relevant in the blue where we intend to measure Ca II lines. In order to minimize the effects related to these atmospheric changes we create a spectral template for each star by de-blazing and co-adding every available spectrum and use the co-added spectrum to correct the order-by-order fluxes of the individual ones. We also correct each spectrum for the Earth's barycentric radial velocity and the radial velocity of the star using the measurements given by the standard pipeline and re-binned the spectra into a wavelength-constant step. Using this HARPS dataset, we expect to have high quality spectroscopic indicators to monitor tiny stellar activity and radial velocity variations with high accuracy.

2.2.2 Spectroscopic Data - Mount Wilson HK Project

The Mount Wilson HK Project at the Mount Wilson Observatory (MWO), which aimed at studying stellar chromospheric activity and variability, was started by Olin Wilson in early 1966 and continued by Art Vaughan, George Preston, Douglas Duncan, Sallie Baliunas, and many others through 2002. It was one of the first and most outstanding programs of observation of solar-type stars. One of its most important achievements was the discovery of 11-yr cycles in solar-type stars (Baliunas et al. 1995). The recent data release (June 2016)[1] provides calibrated time series of the S_{MW} index from 1966 up to 1995, with data up to 2001 for some stars. Data were acquired at the 2.5m Hooker telescope and at the 1.5m Hale telescope at the MWO. The MWO is located in the north-east of Los Angeles (United States) on the Mount Wilson (Fig. 2.8). Nowadays the MWO is mostly dedicated to solar observations and interferometry because of the light pollution coming from Los Angeles, which diminishes its capabilities for nightly observations.

The Mount Wilson HK data has been used solely for the calibration of the S_{MW} activity index.

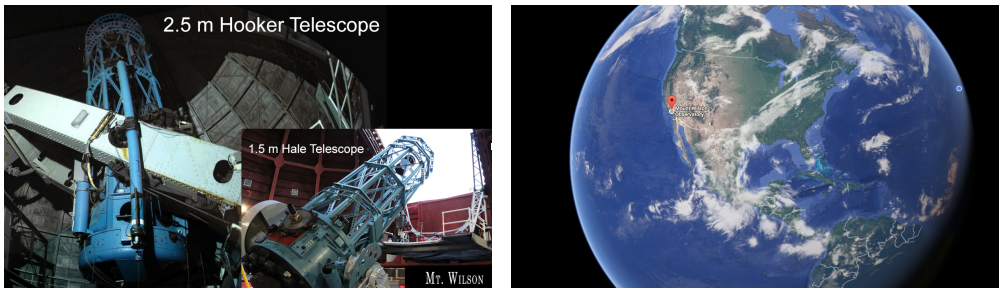

Figure 2.8: The 2.5 m Hooker Telescope and the 1.5 m Hale Telescope (left panel) and the location of the The Mount Wilson Observatory (right panel).

2.2.3 Photometric Data - ASAS

The data from the All Sky Automated Survey (Pojmanski 1997) comes from the last data release of the ASAS-3 system. The ASAS-3 system is a set of four small robotic telescopes. Two wide field telescopes equipped with 200/2.8 Minolta telephoto lens observing in V and I bands, one narrow field telescope (F=750mm, D=250mm, F/3.3 which) and one very-wide field telescope with a 50 mm lens. The ASAS-3 system is installed in the 10-inch astrograph dome of

[1] Data can be found in: ftp://solis.nso.edu/MountWilson_HK/

the Las Campanas Observatory and operated from 2000 to 2009. Las Campanas Observatory is an observatory owned and operated by the Carnegie Institution for Science (CIS) located in the south of the Atacama Desert in Chile (Fig. 2.9).

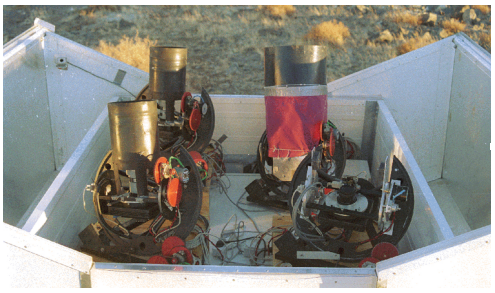
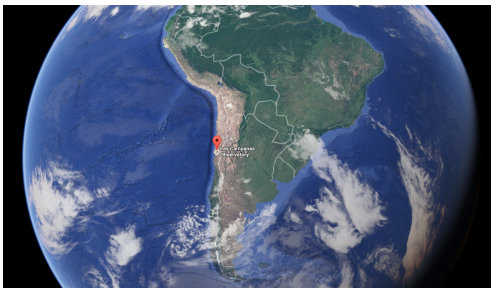

Figure 2.9: The four telescopes of the ASAS-3 System (left panel) and the location of Las Campanas Observatory (right panel).

The ASAS survey in the V and I bands has been running at Las Campanas Observatory (Chile) since 1998. It has a spatial scale of 14"$/pixel$ and an average accuracy of $\sim$ 0.05 mag per exposure. Best photometric results are achieved for stars with V ∼8-12, but this range can be extended if some additional control on the quality of the data is implemented. Almost all stars brighter than V ∼6 show inconsistent results and very large scatter, probably a result of the saturation of the CCD. ASAS has produced light curves for around 10^7 stars at $\delta < 28°$.

2.2.4 Full Available Dataset

The full available sets of data consist in 65301 high resolution spectra, 21191 H&K measurements and 71016 photometric exposures for our 228 stars plus 8 early F and A stars used only for calibration purposes. The number of observations for each individual star is far from homogeneous. Some stars have a few thousand measurements while some other barely reach a dozen measurements. This will lead to different kinds of analysis depending on the amount of available data. Out of the 228 stars, 176 stars have enough data for the study of stellar activity, and 133 stars to search for planetary signals. Table 2.2 shows the number of available measurements of each type for the stars for which we present planetary detections. The full sample available dataset is listed in the Appendix A.2.

The time span of the observations is highly variable too. Ranging from several days to decades. Table 2.3 shows the time span of the observations

Table 2.2: Available data for a selection of the stars of our sample. Full table in Appendix A.2

Star	Sp. Type	HARPS N_{Meas}	HARPS-N N_{Meas}	MW HK N_{Meas}	ASAS N_{Meas}
HD 1581	F9.5	1728			738
HD 161098	G8	120	137		471
HD 176986	K2.5	134	146		425
GJ 536	M1	141	12		359
GJ 3998	M1	6	129		554

of each type for the stars for which we present planetary detections. The full dataset can be found in Appendix A.3.

Table 2.3: Time span of the observations for a selection of the stars of our sample. Full table in Appendix A.3

Star	Sp. Type	HARPS T_{Span} (d)	HARPS-N T_{Span} (d)	MW HK T_{Span} (d)	ASAS T_{Span} (d)
HD 1581	F9.5	3606			3277
HD 161098	G8	3027	428		3155
HD 176986	K2.5	3585	428		3165
GJ 536	M1	4274	30		3153
GJ 3998	M1	94	868		2593

3

Measurement of stellar activity in late-type dwarfs

This chapter summarizes the study of stellar activity performed in the framework if this thesis. We present the studied activity proxies and the procedure used to identify both the stellar cycles and rotation of 176 stars of our sample. We report new measurements of magnetic cycles for 105 stars, and rotation periods for 123 stars. We found that the distribution of cycle lengths for the different spectral types is similar, as the mean cycle is 10.3 years for F-type stars, 7.5 years for G-type stars, 8.8 years for K-type stars, 6.2 years for early M-type stars, and 6.0 years for mid-M-type stars. On the other hand, the distribution of rotation periods is completely different, trending to longer periods for later type stars, from a mean rotation of 8.4 days for F-type stars to 71.6 days in mid-M-type stars. A trend of photometric amplitudes with rotation period is also outlined in the data. The amplitudes of the photometric variability induced by activity cycles of main-sequence GK stars are lower than those of early- and mid-M dwarfs for a given activity index. Using this information, along with the mean activity levels measured as the $\log_{10}(R'_{\rm HK})$ we study the different relationships between the chromospheric activity level of the stars and their rotation and cycles. We find a clear correlation between the mean level of chromospheric activity and the length of the rotation period for all the studied spectral types. This chapter is partially based on the articles by Suárez Mascareño et al. (2015, 2016).

3.1 Stellar Activity Indicators

3.1.1 S_{MW} Index

The Mount Wilson HK project defined the S index as the integrated flux of the core of the Ca II lines divided by the integrated flux of two wide bands

in the continuum at both sides of the absorption lines (Vaughan et al. 1981). For the HARPS and HARPS-N spectra the same index can be defined, using the same spectral passbands as used in the original Mount Wilson HKP-2 Spectrophotometer. This means defining two triangular-shaped passbands with an FWHM of 1.09 Å centred at 3968.470 Å and 3933.664 Å respectively for the CA II H&K line cores, and two 20 Å wide bands centred at 3901.070 Å (V) and 4001.070 Å(R) for the continuum, the S-index is defined as:

$$S = \alpha \cdot \frac{N_H + N_K}{N_R + N_V} \tag{3.1}$$

where N_H, N_K, N_R and N_V represent the total flux in each passband, while α is a calibration constant usually fixed at the value of 2.3. As explained in Lovis et al. (2011a), the Mount Wilson spectrophotometer is designed so that the H & K bands get 8 times as much flux as in a normal spectrograph, so in order to be at the same scale we fixed the calibration constant as $\alpha = 2.3 \times 8$. Figures 3.1 and 3.2 shows the shape of the filters.

Instead of working with integrated fluxes we opt to measure mean fluxes per wavelength interval. This approach has the advantage that it helps minimizing potential edge effects at band boundaries due to finite pixel size and errors in wavelength calibration (Lovis et al. 2011a). The S index then can be written as:

$$\begin{aligned} S &= \alpha \cdot 8 \cdot \frac{\Delta\lambda_{HK}}{\Delta\lambda_{RV}} \cdot \frac{\tilde{N}_H + \tilde{N}_K}{\tilde{N}_R + \tilde{N}_V} \\ &= 2.3 \cdot 8 \cdot \frac{1.09\text{Å}}{20\text{Å}} \cdot \frac{\tilde{N}_H + \tilde{N}_K}{\tilde{N}_R + \tilde{N}_V} \\ &\sim \frac{\tilde{N}_H + \tilde{N}_K}{\tilde{N}_R + \tilde{N}_V} \end{aligned} \tag{3.2}$$

where $\tilde{N}_H, \tilde{N}_K, \tilde{N}_R$ and $\tilde{N}_V$ represent the mean flux per wavelength interval in each passband.

The three S indexes obtained (Mt. Wilson, HARPS and HARPS-N) do not have to necessarily be in the same scale. The spectrographs are different, and therefore the measured contrast between the line cores and the continuum does not have to be comparable. To ensure the compatibility of the three measurements it is necessary to calibrate them. For historical reasons the Mt. Wilson S index is taken as the template value. The amount of stars with common Mt. Wilson and HARPS data, or Mt. Wilson and HARPS-N data is not as large as it would be ideal, but combining both HARPS and HARPS-N

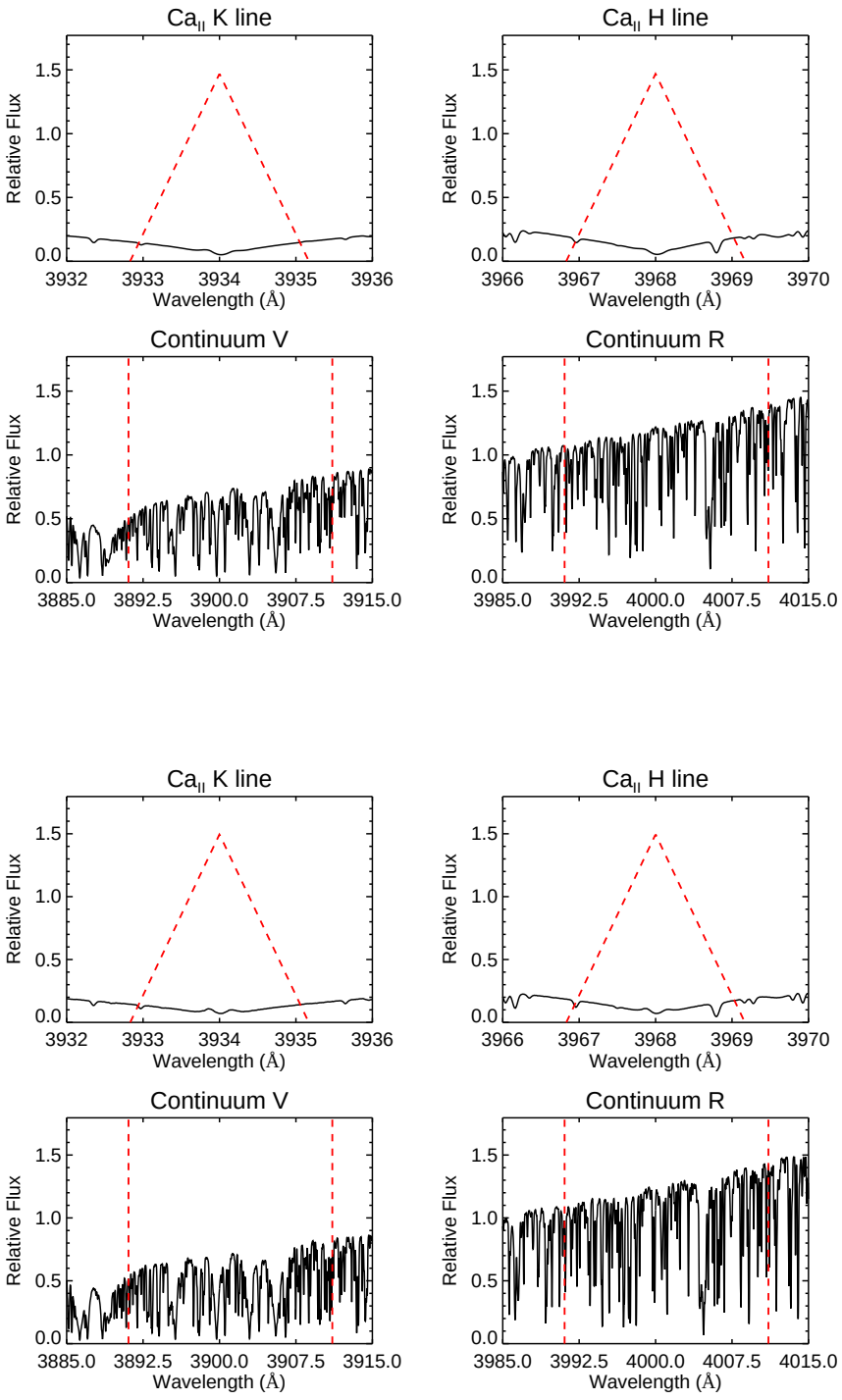

Figure 3.1: Ca II H&K filter of the spectrum of the F-type star HD 1581 (upper panel), the G-type star HD 161098 (lower pannel).

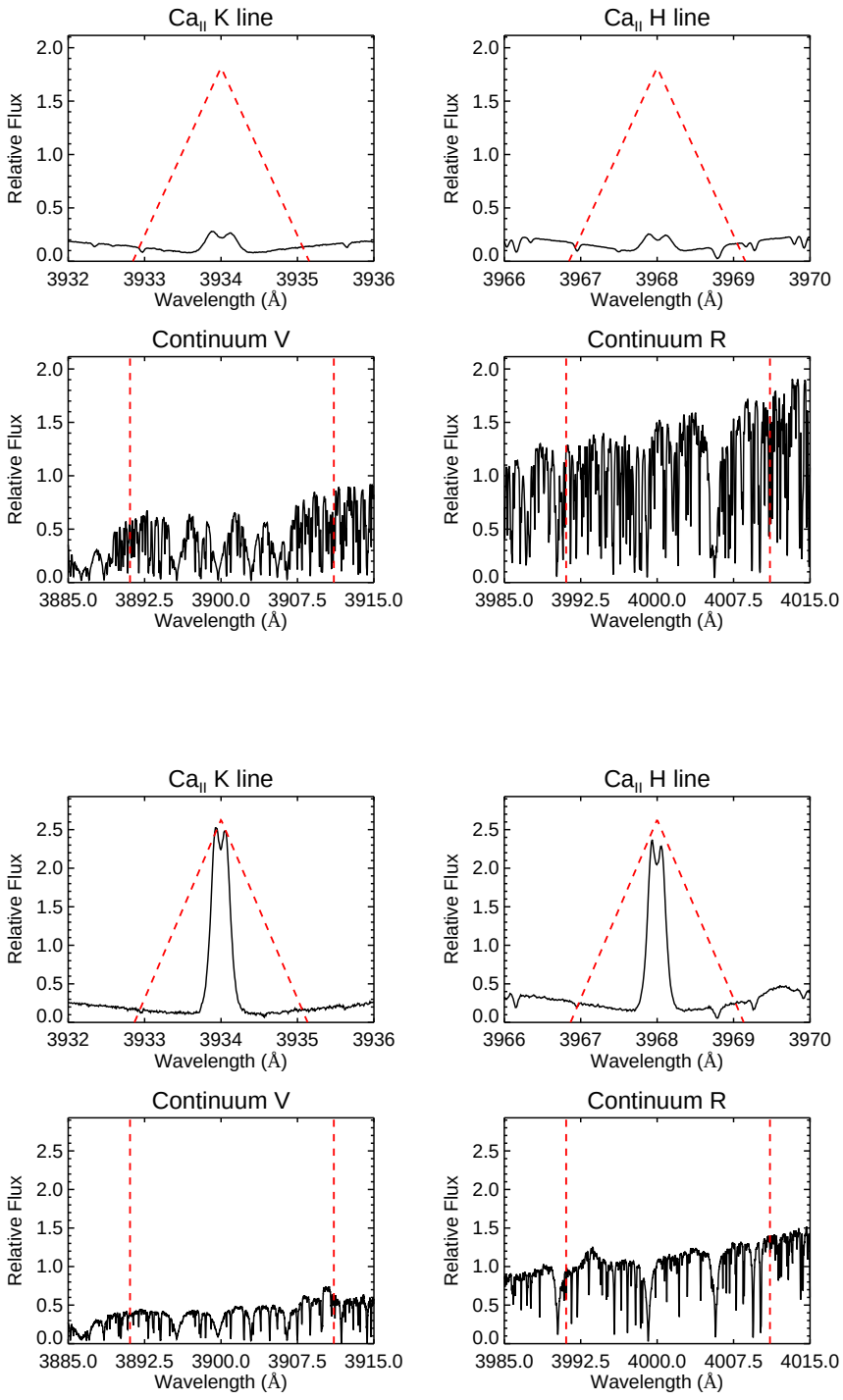

Figure 3.2: Ca II H&K filter of the spectrum of the K-type star HD 176986 (upper panel) and the M-type star GJ 536 (lower panel).

data the comparison data grows significantly. Therefore the first step is the calibration of the HARPS and HARPS-N data. HARPS and HARPS-N are almost identical spectrographs and behave in a very similar way. We calibrate the HARPS-N measurements into the HARPS scale by performing a linear fit using all the stars with common data. Fig. 3.3 shows the linear fit used to calibrate the HARPS-N S-index into the HARPS scale. We obtain the following relationship between the indexes measured in the two spectrographs:

$$S_{HARPS} = 1.04 \cdot S_{HARPS-N} - 0.011 \tag{3.3}$$

The calibration to the Mt. Wilson scale is performed by comparing the measured S indexes of the Mt. Wilson and the HARPS and HARPS-N spectrographs for the stars with common data. The intrinsic variability of the stars might affect this calibration – it is possible to measure a star in two different epochs with the same instrument and measure two different, non compatible, values – the inclusion of as many stars as possible should ensure that all variations get buried as scatter. The bigger the number of stars the less likely it is to see a systematic change in any direction. Fig. 3.3 shows the linear fit used to calibrate the HARPS S-index into the Mt Wilson scale.

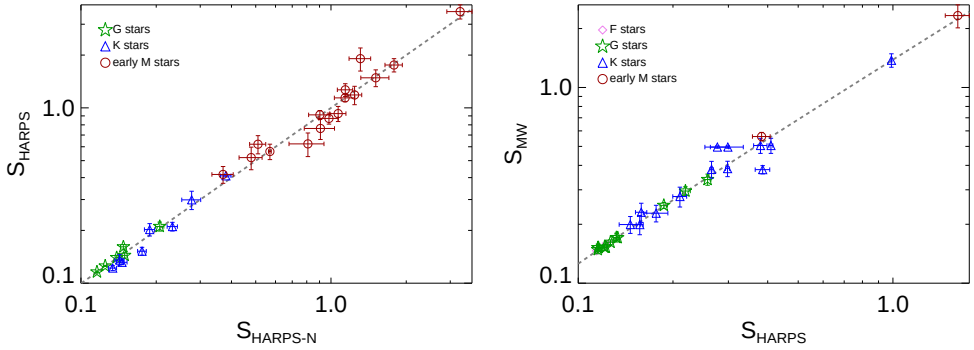

Figure 3.3: S_{HARPS} against S_{HARPS_N} (left panel) and S_{MW} against S_{HARPS} and $S_{HARPS-N}$ calibrated into the S_{HARPS} scale (right panel). The dashed grey line shows the best fits to the data.

A linear fit to Mt Wilson and HARPS values provides the calibration:

$$S_{MW} = 1.317 \cdot S_{HARPS} - 0.011 \tag{3.4}$$

Combining it with Eq. 3.3 we obtain:

$$S_{MW} = 1.370 \cdot S_{HARPS-N} - 0.106 \tag{3.5}$$

The S_{MW} index is a highly spectral type dependent index. As the value of the continuum decreases at lower temperatures, the index increases and thus its variations. Table 3.1 shows the measured mean S_{MW} indexes for the stars for which we present planetary detections and the rms of the measurements. Fig. 3.4 shows the evolution of the mean S_{MW} index value with colour and the histogram of measured S_{MW} indexes.

Table 3.1: S_{MW} measurements and S_{MW} RMS for the stars for which we present planetary detections. Full table in Appendix B.1

Star	Sp. Type	$< S_{MW} >$	RMS $(S_{MW})^*$
HD 1581	F9.5	0.1638	0.0013
HD 161098	G8	0.1809	0.0043
HD 176986	K2.5	0.294	0.016
GJ 536	M1	1.37	0.12
GJ 3998	M1	1.57	0.13

* RMS of the different measurements of the same star.

3.1.2 $Log(R'_{HK})$

The S-index gives the Ca II H&K core flux normalized to the neighbouring continuum. This index is very useful to study periodicities related to the rotation and/or long term cycles but is extremely spectral type dependent. Not only the contrast between the line cores and the continuum increases when going to cooler stars, but it includes a photospheric contribution that is increased towards hotter stars. To compare stars of different spectral type it is necessary to subtract the photospheric contribution and normalize the chromospheric flux to the bolometric luminosity of the star. For that reason the $R'_{\rm HK}$ index was developed (Noyes et al. 1984), and it is defined as:

$$R'_{\rm HK} = 1.34 \cdot 10^{-4} \cdot C_{\rm cf}(B-V) \cdot S - R_{\rm phot}(B-V) \tag{3.6}$$

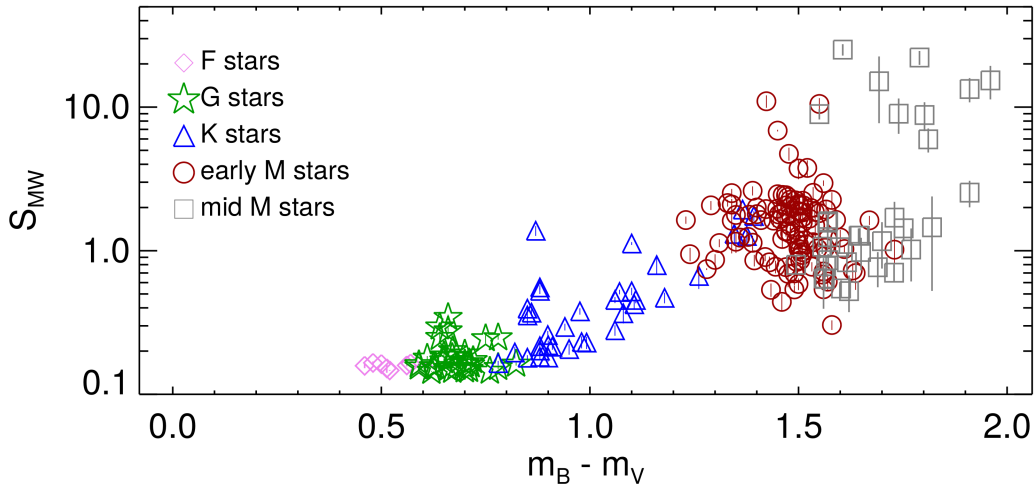

Figure 3.4: S_{MW} mean measurements against the B-V colour. Bars show the RMS of the different measurements for each star. A-type and early F-type stars are not included as the photospheric contribution greatly surpasses the chromospheric contribution.

where $C_{\rm cf}(B-V)$ is the conversion factor that corrects flux variations in the continuum passbands and normalizes to the bolometric luminosity and $R_{\rm phot}$ is the photospheric contribution. The Noyes et al. (1984) original conversion factor is based on the Middelkoop (1982) calibration, which is still widely used nowadays. But this calibration is only reliable in a narrow colour range (from $B-V \sim 0.45$ to ~ 1.2). The sample under study also contains stars outside that range. This bolometric correction has been extended at least once (Rutten 1984), but the sample still exceeds the range of application of the updated calibration (from $B-V \sim 0.45$ to ~ 1.6). To extend the range of applicability to the realm of M-dwarfs a new calibration is needed. To do so it is enough to follow the original Middelkoop (1982) and Rutten (1984) procedure used to perform the original calibration. The factor $C_{\rm cf}$ is defined as as:

$$C_{\rm cf} = (S_R + S_V) \cdot 10^{-4} \cdot 10^{0.4(m_v + BC)}, \tag{3.7}$$

where S_R and S_V are the mean fluxes measured in the continuum passbands, m_V is the visual magnitude in the V band and BC is the bolometric correction according to Johnson (1966).

The first step is to calibrate HARPS and HARPS-N S_R and S_V fluxes. HARPS and HARPS-N are mostly identical, but the sensitivity of the HARPS-

N CCD in the blue edge is better than in the original HARPS CCD. Taking the HARPS S_R and S_V values as the base measurement, as they fit nicely with the Rutten (1984) measurements, calibrate the HARPS-N S_R and S_V into the HARPS scale is trivial using the stars with common measurements. Fig. 3.5 shows how the HARPS and HARPS-N continuum fluxes compare.

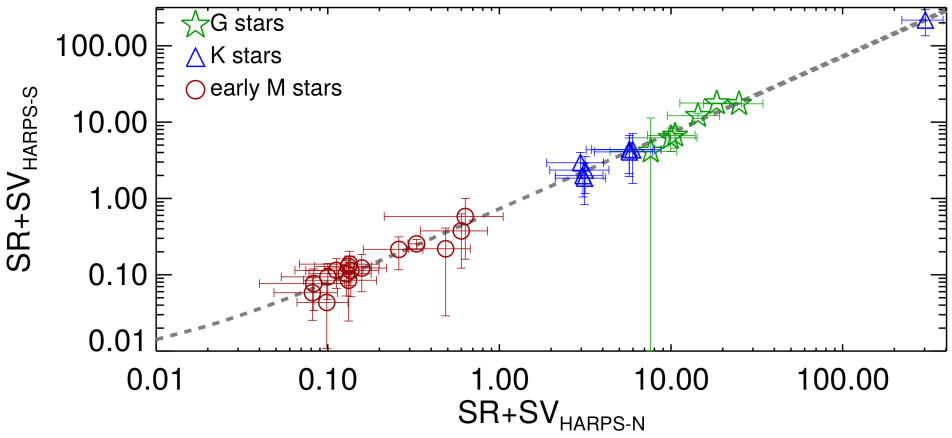

Figure 3.5: $(S_R + S_V)_{HARPS}$ versus $(S_R + S_V)_{HARPS-N}$ for stars with data in common.

A linear fit to the data gives us that:

$$(S_R + S_V)_{HARPS} = 0.6 \cdot (S_R + S_V)_{HARPS-N} \tag{3.8}$$

The final values for the C_{cf} can be seen in Figure 3.6. The original measurements from Rutten (1984) are included to strengthen the statistics. The new calibration is performed by fitting a fourth-order least-squares polynomial to the data. It provides the following correction factor, which is valid in the range from $B - V \sim 0.4$ to $B - V \sim 1.95$.

$$\begin{aligned} \log_{10} C_{\rm cf} = {} & 0.013(B-V)^4 - 0.032(B-V)^3 \\ & -0.661(B-V)^2 - 0.061(B-V) + 0.331 \end{aligned} \tag{3.9}$$

Figure 3.1 shows the shape of the H & K bands, they are wide enough to ensure that no light is missing from the core emission line. But this also allows some photospheric contribution to the measured flux in the wings of the band. The photospheric contribution to the H & K passbands $R_{\rm phot}$ was modelled by Hartmann et al. (1984) for the Mount Wilson HKP-2 Spectrophotometer. For

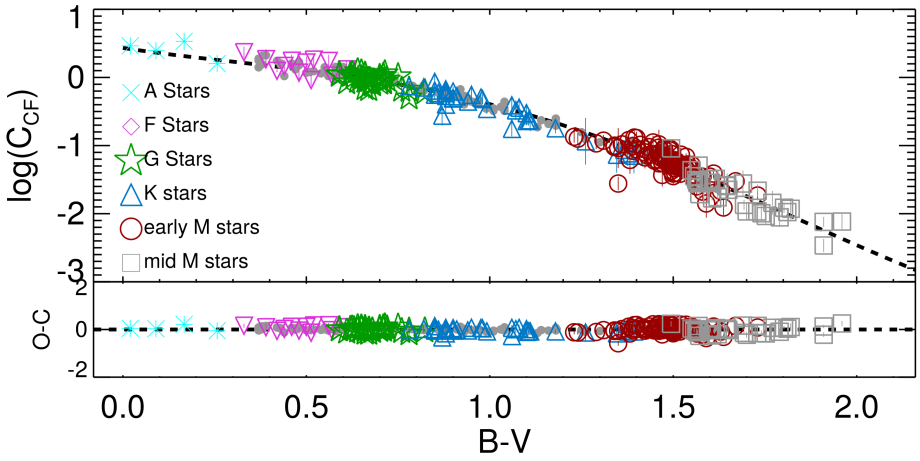

Figure 3.6: Conversion factor C_{cf} against $B-V$ colour for the combination of the sample stars (coloured symbols) and the Rutten (1984) sample (grey symbols). The curve is the fourth-order least-squares polynomial fits. A-type and early F-type stars are included to guarantee the good behaviour of the polynomial fit near the blue edge of the sample.

HARPS and HARPS-N a specific calibration is needed. The $R_{\rm phot}$ is defined as:

$$R_{\rm phot} = 1.34 \cdot 10^{-4} \cdot C_{cf}(B-V) \cdot S_{\rm phot}. \tag{3.10}$$

To calibrate the index it is enough to measure the $S_{\rm phot}$ by following Hartmann et al. (1984), i.e. subtracting the core emission line from the H & K passbands in the spectrum where the lowest activity is recorded and measuring the residual flux inside the band. This is done by defining the limits of the core emission line inside the filter defined in Fig. 3.1 as a 0.7 Å rectangular window around the core-emission lines for F-G-K stars and a 0.4 Å window for M-dwarfs and then measuring the flux outside those limits. Figure 3.7 shows the evolution of the measured $R_{\rm phot}$ with the B-V colour, which we calibrate as:

$$\log_{10}(R_{\rm phot}) = 1.48 \cdot 10^{-4} \cdot exp[-4.3658 \cdot (B-V)] \tag{3.11}$$

The final quantity used to compare the chromospheric activity level of different stars is the $\log_{10}(R'_{\rm HK})$.

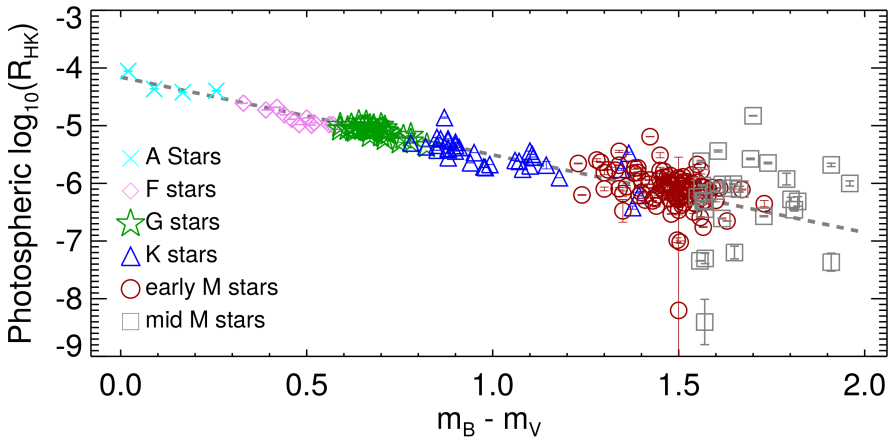

Figure 3.7: Measured $\log_{10}(R_{\rm phot})$ against the colour of the sample stars. The grey dashed line shows the best fit to the data. A-type and early F-type stars are included to guarantee the good behaviour of the fit near the blue edge of the sample.

$$\log_{10}(R'_{\rm HK}) = \log_{10}(1.34 \cdot 10^{-4} \cdot C_{\rm cf}(B-V) \cdot S - R_{\rm phot}(B-V)) \qquad (3.12)$$

Table 3.2 shows the measured $\log_{10}(R'_{\rm HK})$ and its rms for the stars for which we present planetary detections. The full dataset can be found in the Appendix B. Figure 3.8 shows the evolution of the $\log_{10}(R'_{\rm HK})$ against the colour B-V. Stars from late F-type to early M-type show a very similar behaviour. After crossing the M2-type the situation changes. Stars later than M2 show a larger range of activity levels, going down to extremely low values.

3.1.3 H_α Index

In the case of the Hα index we use a simpler passband following Gomes da Silva et al. (2011). It consists of a rectangular bandpass with a width of 1.6 Å and centred at 6562.808 Å (core), and two continuum bands of 10.75 Å and 8.75 Å centred at 6550.87 Å (L) and 6580.31 Å (R), respectively, as seen in Figure 3.9. As in the case of the S_{MW} index we opted to measure mean fluxes per wavelength instead of total fluxes.

Thus, the Hα index is defined as

Table 3.2: $\log_{10}$R'$_{HK}$ measurements and RMS for the stars for which we present planetary detections. Full table in Appendix B.2

Star	Sp. Type	$\log_{10}$R'$_{HK}$	RMS ($\log_{10}$R'$_{HK}$)
HD 1581	F9.5	–4.84	0.01
HD 161098	G8	–4.83	0.02
HD 176986	K2.5	–4.83	0.03
GJ 536	M1	–4.99	0.04
GJ 3998	M1	–5.00	0.04

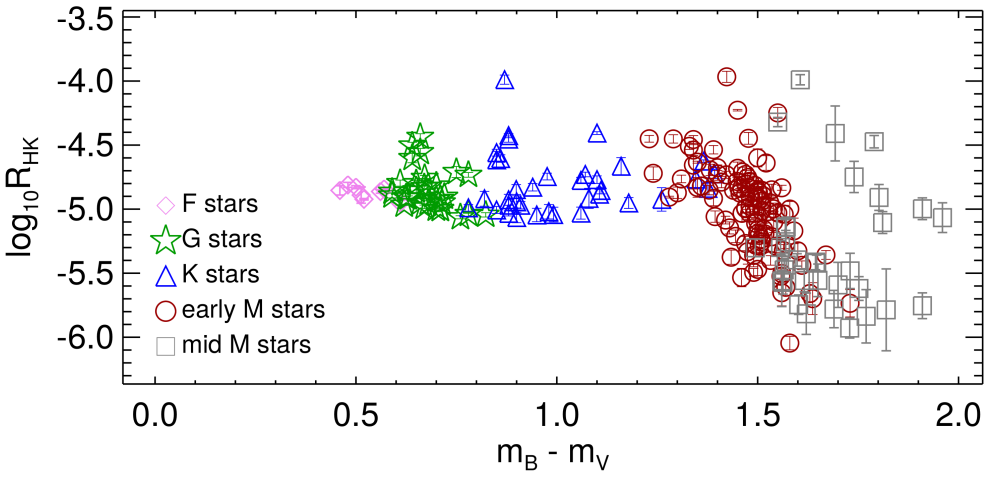

Figure 3.8: Evolution of the measured $\log_{10}(R'_{\rm HK})$ against the colour B-V. A-type and early F-type stars are not included as the photospheric contribution greatly surpasses the chromospheric contribution.

$$H\alpha_{\rm Index} = \frac{\tilde{H}\alpha_{\rm core}}{\tilde{H}\alpha_L + \tilde{H}\alpha_R}. \tag{3.13}$$

The HARPS and HARPS-N H$_\alpha$ indexes are not exactly equal. To calibrate the HARPS-N H$_\alpha$ index into the HARPS scale we compare the mean measure-

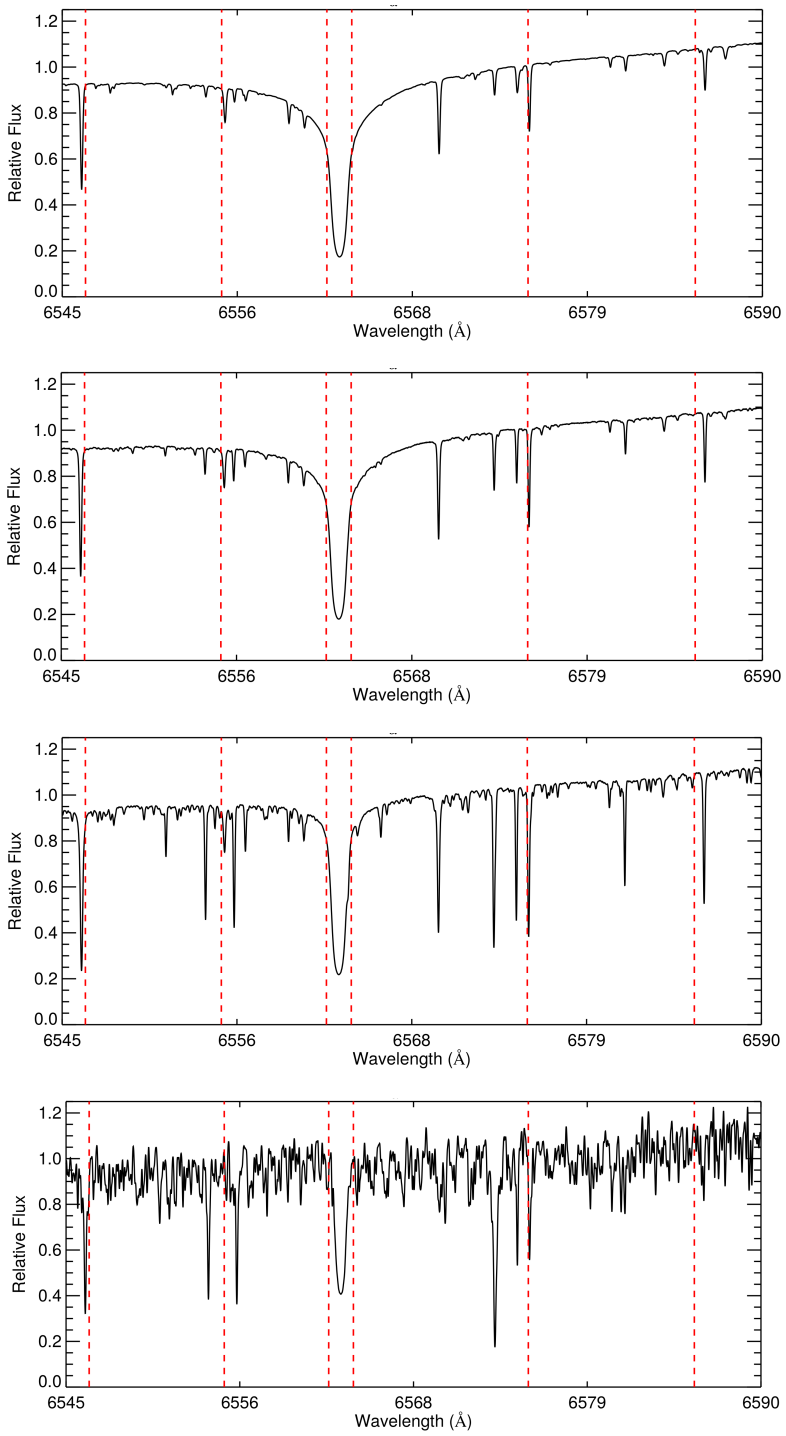

Figure 3.9: Spectrum of the F-type star HD 1581 (top panel), the G-type star HD 161098 (middle-up), the K-type star HD 176986 (middle-low panel) and the M-type star GJ 536 (lower panel) showing the Hα filter passband and continuum bands.

ments as done with the S_{MW} index. Fig. 3.10 show the comparison of both indexes. The relation between them is very similar to that of the S_{MW} index:

$$H_{\alpha\ HARPS} = 1.04 \cdot H_{\alpha\ HARPS-N} - 0.010 \tag{3.14}$$

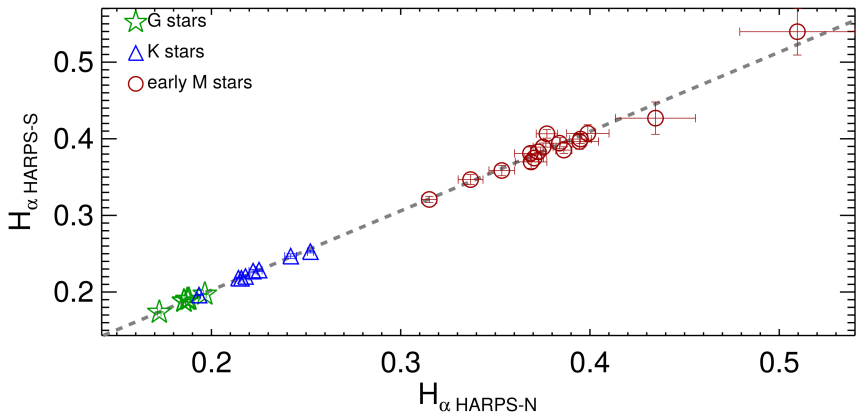

Figure 3.10: S_{HARPS} against S_{HARPS_N}. The dashed line shows the best fit to the data. A-type and early F-type stars are not included as the photospheric contribution greatly surpasses the chromospheric contribution.

As in the case of the S_{MW} index, this index is a highly spectral type dependant index. Tab. 3.3 shows the measured mean H_α indexes for the stars for which we present planetary detections and the rms of the measurements. Fig. 3.11 shows the evolution of the mean H_α index value with colour.

3.1.4 Photometry

The ASAS catalogue supplies ready-to-use light curves with flags indicating the quality of the data. For this analysis we relied only on good quality data (grade "A" and "B" in the internal flags). Even after this quality control, there are still some high dispersion measurements that cannot be explained by a "regular" stellar behaviour. There are some cases of extreme scatter in stars closer to the magnitude limits of the survey and some stars that show a behaviour compatible with stellar flares. As our data is not well suited for modelling flares, to remove flare affected points, we iteratively rejected all measurements that deviate from the seasonal median value more than 3 times the rms of the full light curve. Iteration was applied until no more measurements where left outside these

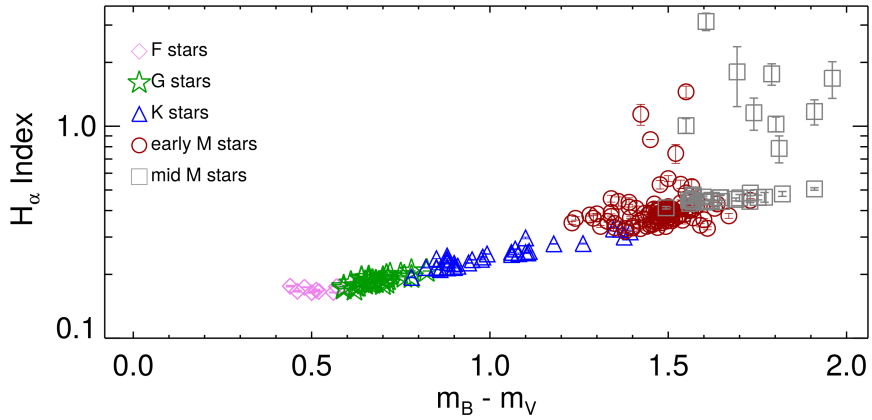

Figure 3.11: Evolution of the H_α index against the B-V color.

limits. Table 3.4 shows the data for the ASAS measurements for the stars for which we present planetary detections.

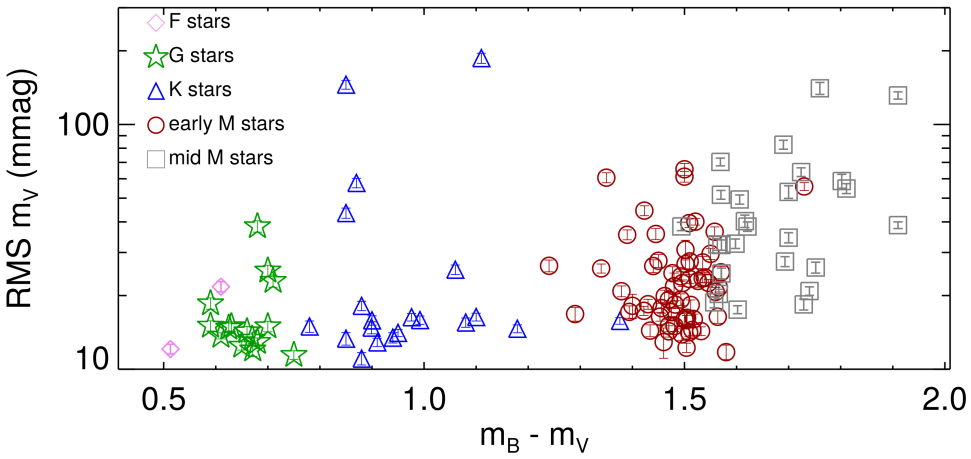

Figure 3.12: Dispersion of the visual magnitude measurements for all the stars with ASAS photmetric lightcurves. Vertical bars show the intrinsic uncertainty of the measurements.

Table 3.3: H_α index measurements for a selection of stars in the sample. Full table in B.3

Star	Sp. Type	H_α Index	RMS H_α
HD 1581	F9.5	0.1779	0.0004
HD 161098	G8	0.1853	0.0008
HD 176986	K2.5	0.2263	0.0013
GJ 536	M1	0.3717	0.0076
GJ 3998	M1	0.3580	0.0059

Table 3.4: Mean photometric magnitude and RMS of the measurements for the stars for which we present planetary detections. Full table in Appendix B.4

Star	Sp. Type	m_V (mag)	$m_{V\ ASAS}$ (mag)	RMS (mmag)	Flag
HD 1581	F9.5	4.23	4.959	327.28	Bad Photometry
HD 161098	G8	7.67	7.681	13.31	
HD 176986	K2.5	8.45	8.460	13.45	
GJ 536	M1	9.71	9.708	14.29	
GJ 3998	M1	10.83	10.848	23.36	

3.2 Searching for stellar variability

Stellar rotation and long-term magnetic cycles can be detected by analysing the periodic variability of spectroscopic indicators and photometric time series. For time series with enough data a generalised Lomb-Scargle periodogram (Zechmeister & Kürster 2009) will return a set of candidate periodicities that then can be fitted using pseudo-sinusoidal models. For the case of stellar activity a double harmonic sinusoidal model is usually an appropriate choice as it can cope with the irregularities of the activity series without introducing parameters without physical meaning. For the following analysis the signals have been modelled by least squares minimization with the MPFIT routine (Markwardt 2009) using Eq. 3.15 as test model.

$$\begin{aligned} y(t) = A_1 \cdot sin(2 \cdot \pi \cdot t/P + \phi_1) \\ +A_2 \cdot sin(2 \cdot \pi \cdot t/(0.5 \cdot P) + \phi_2) + C \end{aligned} \tag{3.15}$$

The parameters and errors of the individual signals are given by the parameters and errors calculated by the MPFIT routine.

Once a signal is detected and modelled, we subtract the fitted signal and the analysis is repeated in the residuals after the fit. This process is called prewhitening, and is a commonly used tool for finding multi-periodic signals in time series data (Vaníček 1971). It is iterated until no more significant signals are found. When multiple signals are found the final parameters are always given by the simultaneous fit of all the detected signals.

The significance of the periodogram peak is evaluated using the Cumming (2004) modification of the Horne & Baliunas (1986) formula to obtain the spectral density thresholds for a desired false alarm level. The false alarm probability is defined as $FAP = 1 - [1 - P(z > z_0)]^M$ where $P(z > z_0)$ is the probability of z, the target spectral density, being greater than z_0, the measured spectral density, and M the number of independent frequencies, approximated as $\Delta T/\delta t$, with the time span of periodogram going from 1.5 to 10 000 days and the number of frequency steps fixed at 100 000.

We have data from many different sources with very different observational cadences. In some situations, for instance the case of HARPS and HARPS-N data for the brightest stars, we even have multiple exposures every day of observations. In these situations we rebin the data into daily measurements. The Nyquist frequency of our data is hard to determine, as it varies from star to star and from dataset to dataset. However none of the datasets is well suited to measure very high frequency signals. We limit the search for variability to periods longer than 1.5 days. On the low frequency side we limit the search to

10 000 days, that is approximately 3 times longer than the longest time span of the HARPS N/S. This allows us to measure incomplete signals, obviously involving large uncertainties.

To study the expected uncertainties related to periods longer than the time-span of the observations we simulate 5000 datasets with periodic signals periods from 0.1 to 18000 days and time-spans from 100 days to 4500 days. Each dataset has its own number of observations going from 50 to 1100 with a random distribution of measurements inside the time-span of the observations. Signals have amplitudes compatible with the typical RMS of the S_{MW} index measurements and Gaussian noise compatible with the typical error bars of the S_{MW} index measurements. For each trial we try to detect and fit the signal following the procedure explained before.

For signals with periods shorter than the time-span of the observations we recover 97.9% of the signals with an error of the detection smaller than 10% of the test period and 92.5% with an error smaller than 1% of the test period. For signals with periods between 1 and 2 times the time span of the observations we recover 70.1% of the signals with a measured period inside the 10% of the test period and 35% of the signals with a measured period inside the 1% of the test period. For signals between 2 and 3 times the time-span of the observations we recover 24.1% of signals with an error in the determination smaller than 10% of the test period 4.5% of the signals with an error smaller than 1% of the test period. For signals longer than 3 times the time-span of the observations we are only able to recover 7% of the signals with an error in the determination smaller than the 10% of the test period. Figure 3.13 shows the results of the simulations.

The different activity proxies that we are using provide us with information about different parts of the stellar atmosphere. Photometry gives information mainly about photospheric variability, while the S_{MW} and H_α indexes speak about the variability at different heights of the stellar chromosphere and sometimes maybe even at different latitudes and different seasons. It is not expected that the three variability indicators give results compatible within the error bars of the individual fits. The mean cycle and rotation of a star is estimated by calculating the weighted average of the different detections. The error in the determination is the standard deviation of the measurements and the global false alarm probability is the combined probability of the null hypothesis being true given by a Fisher's combined probability test (Fisher 1925).

HARPS is known to have a one year parasitic signal caused by the deformation of spectral lines crossing block stitchings of the CCD (Jérémy Coffinet 2015; Dumusque et al. 2015). This signal, along with the imprecision in the Earth's barycentric radial velocity correction, might cause a one-year parasitic

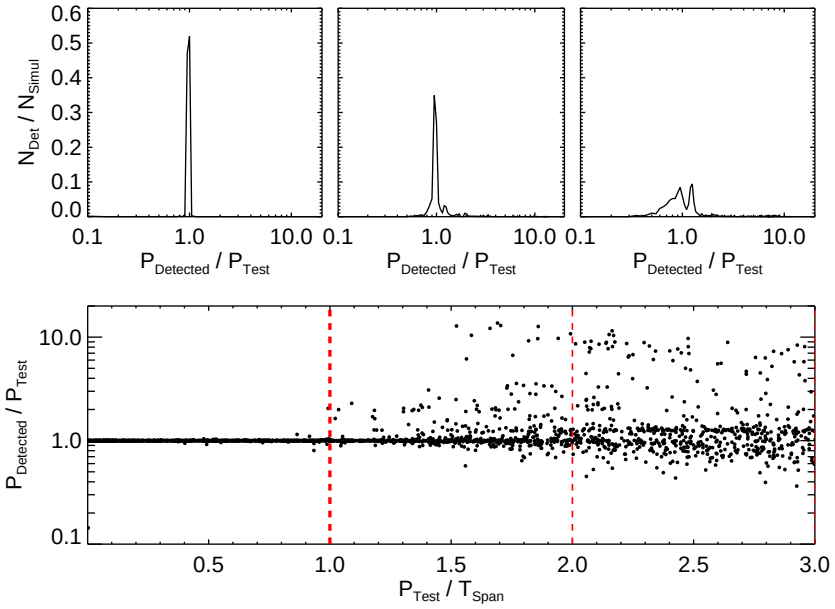

Figure 3.13: Results of the simulations to test the detection limits. Upper panels show the density of detections for the cases of periods smaller than the time-span (left panel), periods from 1 to 2 times the time-span of the observations (central panel) and periods from 2 to 3 times the time-span of the observations (right panel). Bottom panel shows the detected periodicities relative to the test periodicities (1 meaning perfect detection) against the test period normalized to the time-span of the observations (1 meaning period equal to time-span of the observations).

signal in the time series of activity indexes in the case of stars with very small variations. (Dumusque et al. 2015) suggested fitting a 1 year sinusoidal in the case of the radial velocities to clean the data from the parasitic signal. We opt to do the same for the activity indicators in those datasets affected by the parasitic signal.

A pre-screening of all the targets is performed using a home-made automatic tool that identifies the stars with significant variability and analyses them searching for long term trends, magnetic cycles and rotation periods using the S_{MW} and H_α indexes of HARPS and HARPS-N combined, and the ASAS light-curves. So far it is able to identify all the significant periodic components

and interpret the obvious ones, e.g. large amplitude magnetic cycles, very long magnetic cycles (far from the year) and simple rotation patterns (maximum of 3 components: rotation, one obvious harmonic and one differential rotation signal – assuming it detects the rotation signal in the first place). This tool allowed us to do a fast selection of interesting cases before going into a detailed analysis.

In order to illustrate the method, we describe below the cases of five stars with different spectral types for which we determine long-term cycles and rotation periods. The chosen stars are the four stars were planetary companions have been detected (HD 1581, HD 161098, HD 176986 and GJ 536), with the addition of GJ 3998 which is the star were we confirm the discovery of Affer et al. (2016) with a completely independent analysis of the data. Those stars also have the particularity of showing a wide variety of activity patterns, making them specially useful to illustrate the difficulties of the process.

HD 1581

The late F star HD 1581 has 1728 HARPS spectroscopic measurements taken during 201 individual nights over 9.9 years and 728 ASAS photometric measurements taken during 589 nights over 9.0 years (Fig. 3.14).

A visual inspection of the S_{MW} curve shows a variation that seems compatible with a long term cycle with a F-test giving a probability of that variation being explained by the measurement uncertainties much smaller than the 0.1%. For the H_α index the situation is similar, with the F-test resulting in also a negligible probability of the scatter being due to uncertainties. We consider the photometric measurements not reliable as the measured magnitude drifts 0.73 magnitudes away from the established magnitude of the star, and the scatter is very large. This is probably due to the star brightness being near or beyond the saturation limit of the survey. HD 1581 is a very bright star ($m_V = 4.23$), much brighter than the recommended maximum brightness of the survey ($m_V \sim 8$) and than the saturation limit that we found ($m_V \sim 6$).

The S_{MW} curve of HD1581 is dominated by a long term cycle. The most significant signal detected in the periodogram is at $\sim$ 1500 days, but no satisfying fit could be obtained of that periodicity. Instead we opted for a third order polynomial to fit the long term cycle (Fig. 3.15). The cycle is clearly not closed, so it is not possible to assign a period at this stage.

The residuals after subtracting the long-term variation are dominated by a one-year parasitic signal, that we subtract by fitting and subtracting a one year sinusoidal signal. Cleaning the series unveils a clear short-term periodicity of 14.650 $\pm$ 0.003 days with a semi amplitude of 0.00035 $\pm$ 0.00002, detected

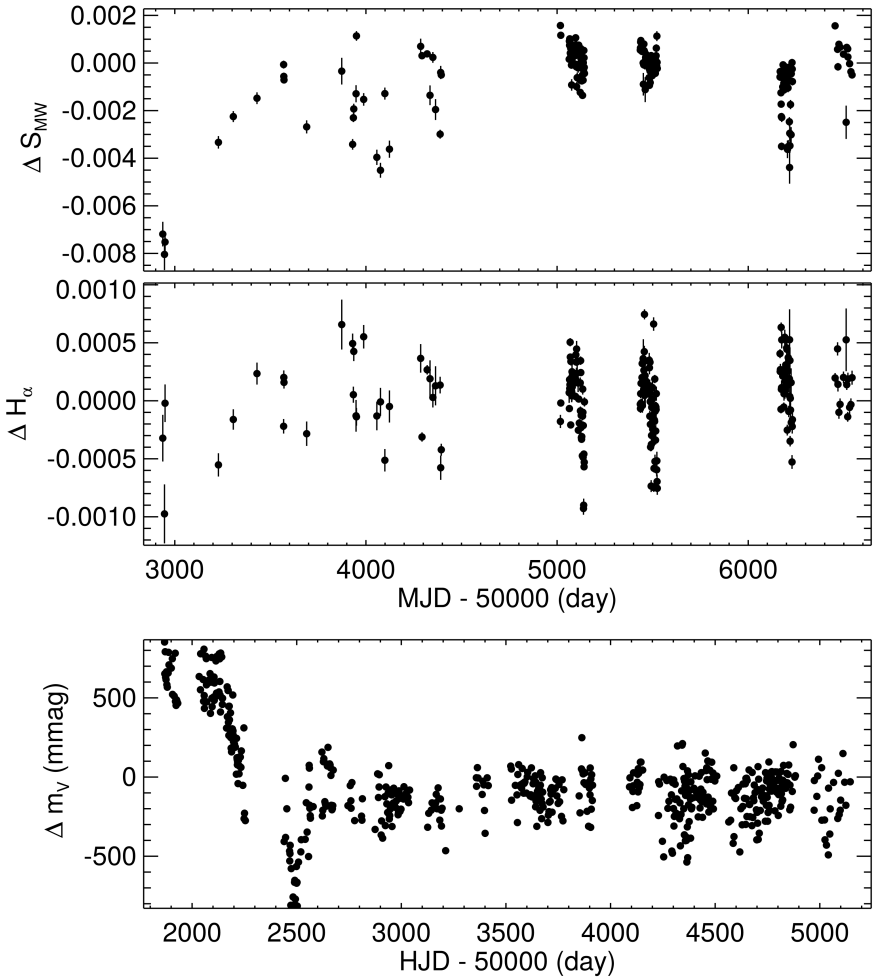

Figure 3.14: S_{MW} index and H_α index time series (upper panel) and photometric measurements (lower panel) for the star HD 1581

with a FAP better than the 0.1 % (Fig. 3.16). An additional peak at the first harmonic of the period is found. The periodicity is compatible with the rotation of the slowest stars of its kind (Suárez Mascareño et al. 2016). That is also consistent with its low activity level (see Table 3.2).

No more significant signals are found in the S_{MW} time-series after subtracting the last one.

The H_α index dataset is completely dominated by the one year parasitic

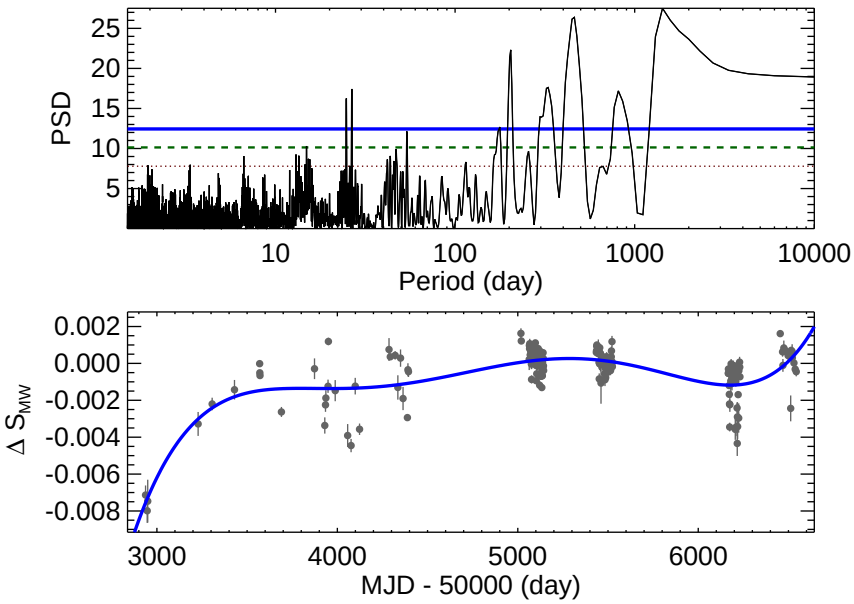

Figure 3.15: Periodogram of the S_{MW} index time series (upper panel) and the third order polynomial fit of the data (lower panel). Horizontal lines show PSD levels equivalent of a 10% FAP (red dotted line), 1% FAP (grey dashed line) and 0.1% FAP (flue solid line).

signal and its harmonics. No significant signals are present after subtracting it. This does not come as surprise, as the H_α index variations are very small, making it hard to search for periodicities using this index in F-type stars, specially in quiet ones. We find one non-significant but interesting signal. A 14.490 ± 0.003 days signal arises with a FAP of $\sim$10% (Fig. 3.17). It has little value on its own, but helps to reinforce the signal detected in the S_{MW} time series.

HD 1581 is a low activity late F-type star that exhibits a long-term magnetic cycle longer than 20 years. The actual cycle length cannot be measured with the available data. It rotates with a period of 14.6 ± 0.1 days. At this point there is not enough available information to measure flip-flop cycles or differential rotation.

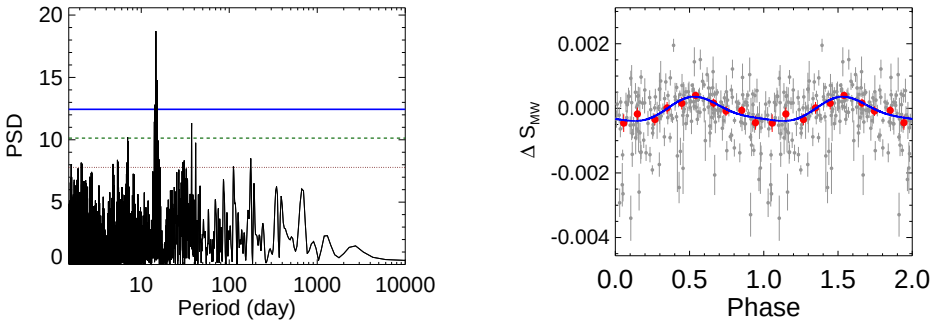

Figure 3.16: Periodogram of the residuals of the S_{MW} index time series of the star HD 1581 (left panel) and phased curve using the 14.65 days periodicity (right panel). Horizontal lines show PSD levels equivalent of a 10% FAP (red dotted line), 1% FAP (grey dashed line) and 0.1% FAP (flue solid line). Grey dots are the raw spectroscopic measurements after subtracting the mean magnitude. Red dots are the same points binned in phase with a bin size of 0.1. The error bar of a given bin is estimated using the weighted standard deviation of binned measurements divided by the square root of the number of measurements included in this bin. This estimate of the bin error bars assumes white noise, which is justified by the binning in phase, which regroups points that are uncorrelated in time.

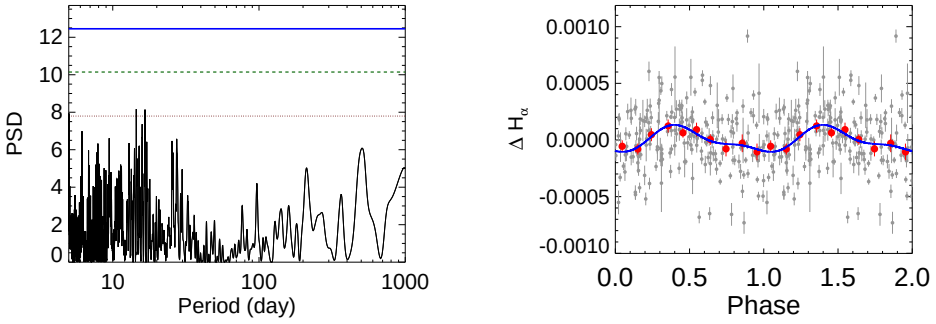

Figure 3.17: Periodogram of the residuals of the H_α index time series of the star HD 1581(left panel) and phased curve using the 14.49 days periodicity (right panel). For a detailed description see Fig. 3.16.

HD 161098

THe mid G star HD 161098 has 120 HARPS and 127 HARPS-N spectra, taken during 178 individual nights along 10.4 years, and 471 ASAS measurements

taken during 438 nights over 8.6 years (Fig. 3.18). The S_{MW} time series shows clear long term variability, which is once again reinforced by an F-test giving negligible probability of the variability being caused by the uncertainties. A similar variability is seen in the H_α curve, also with an almost zero probability of being due to the noise. The photometry in this case shows also a scatter that is to large to be explained by the error bars of the measurements.

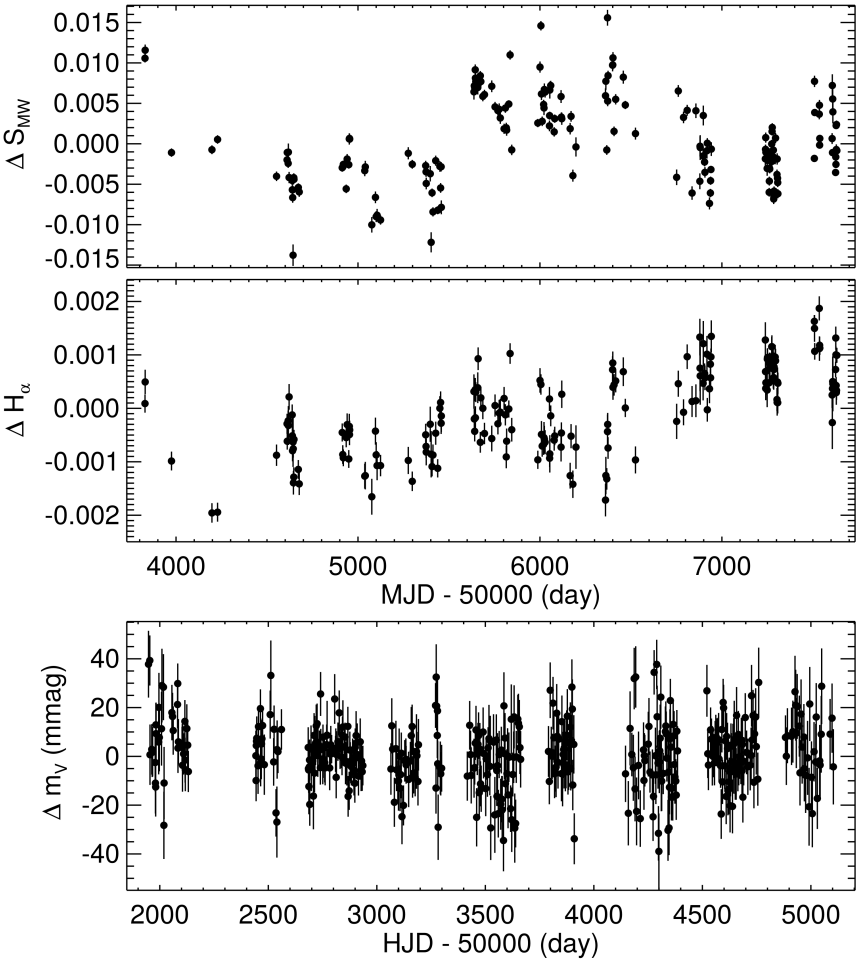

Figure 3.18: S_{MW} index and H_α index time series (top panel) and photometric measurements (bottom panel) for the star HD 161098.

The S_{MW} index dataset is affected by the one-year spurious signal. The first step consists in subtracting it using a sinusoidal fit. The cleaned curve

show a highly significant long term cycle of 2890 ± 180 days (7.9 years) with a semi amplitude of 0.00586 ± 0.00013 (Fig. 3.19). This length is consistent with those of global cycles in solar-type stars.

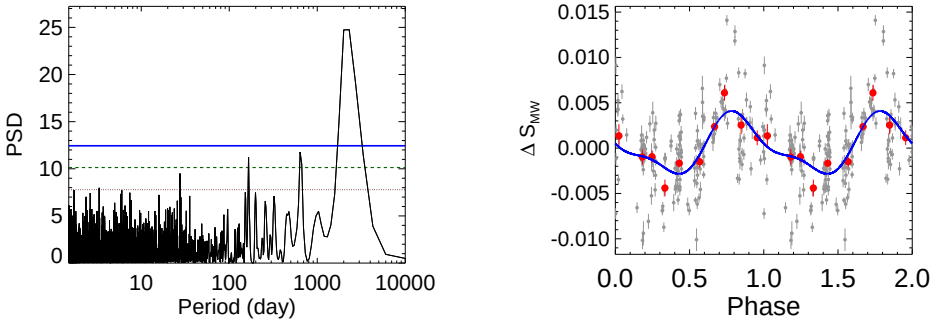

Figure 3.19: Periodogram of the the S_{MW} index time series of the star HD 161098 (left panel) and phased curve using the 7.9 years periodicity (right panel). For a detailed description see Fig. 3.16.

The analysis of the residuals shows a 27.647 ± 0.005 days signal with a false alarm probability smaller than the 0.1% with an amplitude of 0.00207 ± 0.00009 (Fig. 3.20). It is compatible with the typical rotation of a low activity solar type stars.

The periodogram also shows a less significant ∼ 700 days signal, which would be compatible with a flip-flop cycle in a solar type stars but its significance gets greatly diminished after subtracting the rotation signal. Further measurements are needed to study this signal.

No more significant signals are found in the S_{MW} index time series after subtracting the last one.

The H_α index shows a long-term modulation much longer than our baseline which at this point cannot be properly model with a closed signal. We subtract it using a first order polynomial. The resulting data is weakly affected by the one year parasitic signal, so we subtract once again a one year sinusoidal.

That leaves us with a moderately significant signal of 917.8 ± 9.1 days (2.5 years) with a semi amplitude of 0.00036 ± 0.00004 and a FAP better than the 1% (Fig. 3.21). This signal is similar to the non-significant periodicity detected in the S_{MW} index (Fig. 3.20) and it is compatible with a flip-flop cycle of a solar-type star.

Subtracting the flip-flop cycle we are left with the last signal of this dataset. A 28.497 ± 0.012 days signal with a semi amplitude of 0.00035 ± 0.00004 with a FAP better than the 1% (Fig. 3.22). This signal is compatible with the

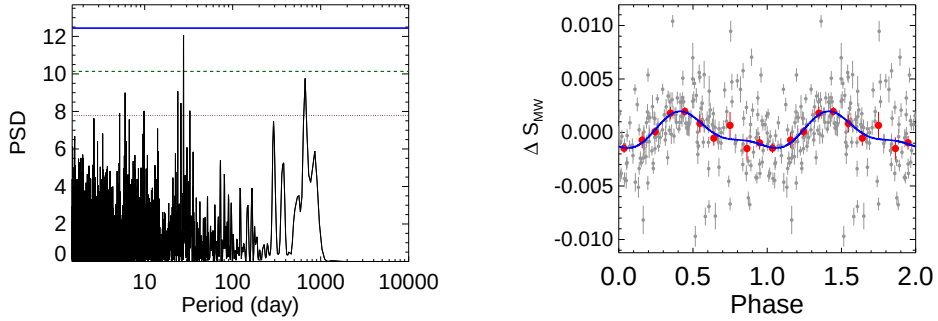

Figure 3.20: Periodogram of the the residuals of the S_{MW} index time series of the star HD 161098 (left panel) and phased curve using the 27.65 days periodicity (right panel). For a detailed description see Fig. 3.16.

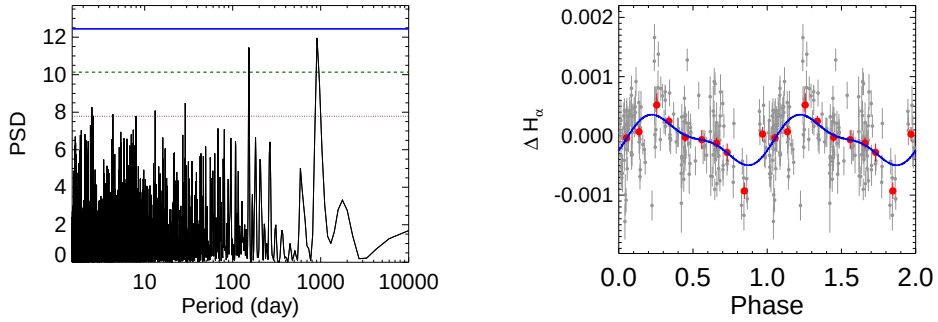

Figure 3.21: Periodogram of the the H_α index time series of the star HD 161098 (left panel) and phased curve using the 917 days periodicity (right panel). For a detailed description see Fig. 3.16.

expected rotation for a star of its kind and also with the rotation modulation found in the S_{MW} index data (Fig. 3.20).

The analysis of the ASAS m_V light curve shows the presence of a 3860 $\pm$ 160 days (10.6 years) with a semi amplitude of 5.7 $\pm$ 1.4 mmag detected with a FAP smaller than the 0.1% (Fig. 3.23).

The detected cycle does not match the S_{MW} index measurement. It might be because of a number of reasons. Different activity proxies do not necessarily give information about the same phenomenon, meaning the S_{MW} index and the m_V might be speaking about two different simultaneous cycles. Stars with several superimposed cycles have been detected in the past (Oláh et al. 2009). Other possibility is that the incomplete sampling of the m_V cycle and the low

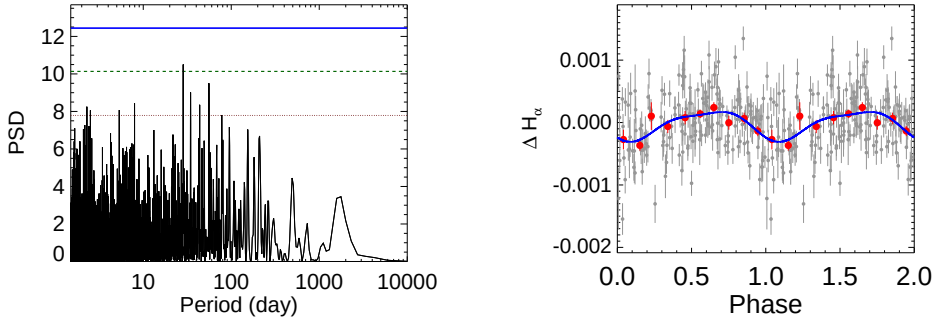

Figure 3.22: Periodogram of the H_α index time series of the star HD 161098 (upper panel) and phased curve using the 28 days periodicity. For a detailed description see Fig. 3.16.

amplitude of the measurement gives us an incorrect measurement of the cycle.

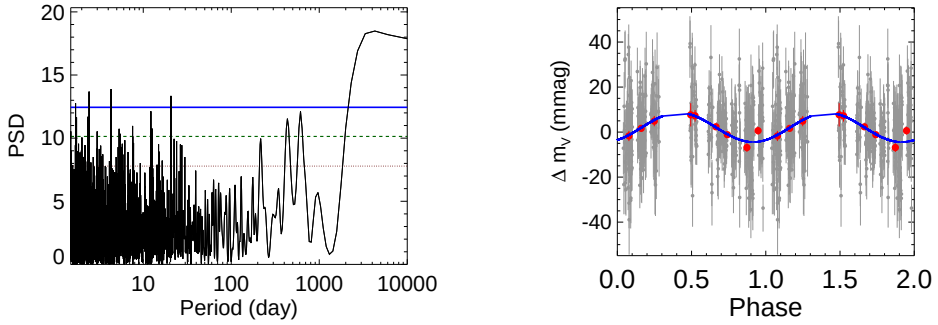

Figure 3.23: Periodogram of the the m_V light-curve of the star HD 161098 (left panel) and phased curve using the 10.6 years periodicity (right panel). For a detailed description see Fig. 3.16.

No more significant signals are found in the photometric data after subtracting the long-term cycle.

In summary, HD 161098 is a moderately low activity G8 star with a rotation period of 28.1 days and two possible super-imposed magnetic cycles of 7.9 and 10.6 years respectively. There is also a flip-flop cycle of 2.5 years.

HD 176986

HD 176986 is a moderately quiet K-type star for which we have 134 HARPS and 146 HARPS-N spectra, coming from 190 individual nights, during 12.2 years of observations. There are also 425 ASAS exposures taken during 411 individual nights during 8.7 years of observations (Fig. 3.24). All our activity proxies show clear signs of variability, that are supported by the results of the F-test which gives a probability of the variability being explained by the error bars much smaller than the 0.1% for the S_{MW} index, the H_α index and for the light curve.

The S_{MW} index dataset is affected by the one-year spurious signal. Once more, the first step consists in cleaning it by subtracting a sinusoidal fit plus a linear term. The cleaned curve shows a very significant long term periodicity of 2468 ± 14 days (6.8 years) with a semi amplitude of 0.01268 ± 0.00028 (Fig. 3.25). This periodicity is consistent with the typical cycle of a K-type star (Suárez Mascareño et al. 2016).

The residuals after fit show a dominant periodicity of 31.432 ± 0.004 days with an amplitude of 0.00716 ± 0.00022 detected with a FAP smaller than the 0.1%. This is consistent with the rotation of a quiet K-type star (Fig. 3.26).

Subtracting the rotation signal reveals a very similar signal of 32.809 ± 0.003 days and a semi amplitude of 0.00781 ± 0.00022, detected also with high significance (Fig. 3.27). The presence of those two signals for the rotational modulation *probably* speak about rotation at two different – but nearby – latitudes.

No more significant signals are found in the S_{MW} index time series after subtracting the last one.

The H_α index time series shows a long term magnetic cycle of 2467 ± 67 days (6.75 years) with a semi amplitude of 0.00105 ± 0.00008 detected with a FAP smaller than the 0.1% (Fig. 3.28). There is one peak in the periodogram that seems to be more significant than the cycle, at ∼ 322 days, but it is the one year alias of the 2467 days peak. This cycle is very similar in length to the one detected in the S_{MW} index data, meaning in this case both indexes are showing us the same change in the activity of the star.

The residuals of the H_α index curve show a very significant periodicity of 26.199 ± 0.006 days with a semi amplitude of 0.00066 ± 0.00012 and a FAP better than the 0.1% (Fig. 3.29). This is compatible with a rotation at a latitude closer to the equator compared to the one measured in the S_{MW} data.

The m_V light curve for HD 176986 shows a significant long term cycle of 2899 ± 142 days (7.9 years) with a semi amplitude of 6.09 ± 0.98 mmag with a FAP smaller than the 0.1% (Fig. 3.30). This measurement is compatible with

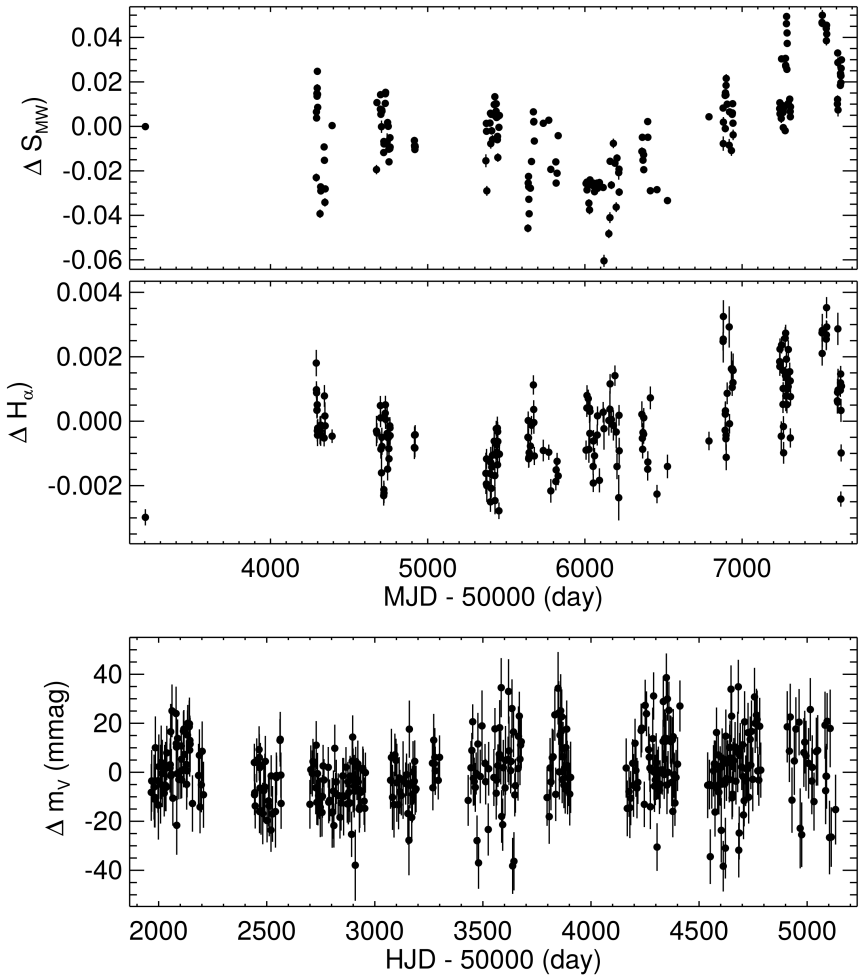

Figure 3.24: S_{MW} index and H_α index time series (upper panel) and photometric measurements (lower panel) for the star HD 176986

those of the S_{MW} and H_α indexes.

No more significant signals are found in the photometric data.

Thus, HD 176986 is a moderately quiet K-type star with a rotation period of 30.2 ± 2.0 days. It exhibits signs of differential rotation, going from 26.2 days up to 32.8 days presumably at different latitudes. The star has a magnetic cycle of 7.1 ± 0.4 years visible in all the studied activity proxies. The cycle length is compatible with the typical global cycle measured in a star of its kind.

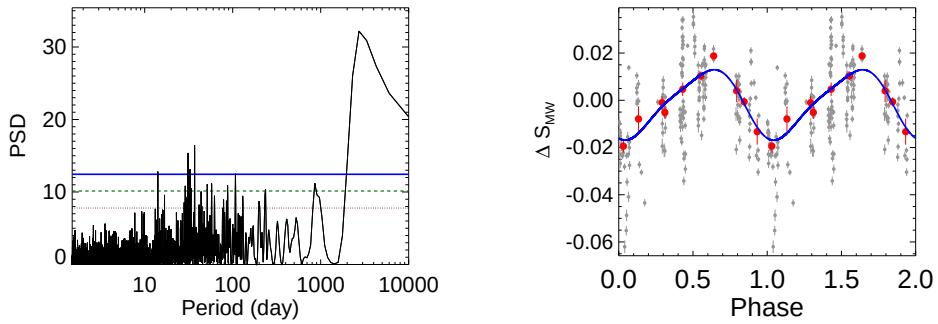

Figure 3.25: Periodogram of the S_{MW} index time series of the star HD 176986 (left panel) and phased curve using the 6.8 years periodicity (right panel). For a detailed description see Fig. 3.16.

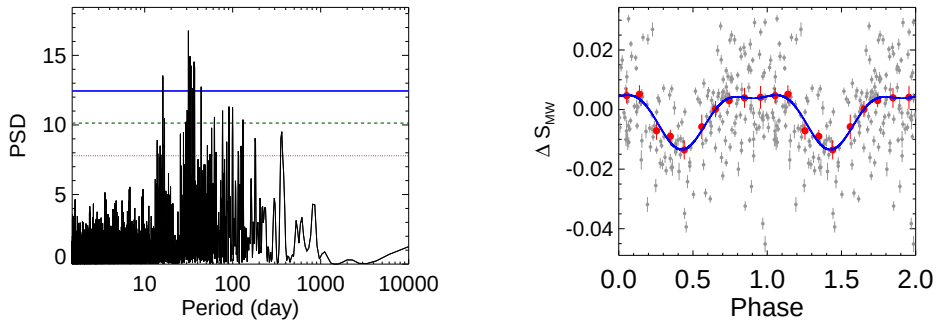

Figure 3.26: Periodogram of the residuals of the S_{MW} index time series of the star HD 176986 (left panel) and phased curve using the 31.4 days periodicity (right panel). For a detailed description see Fig. 3.16.

GJ 536

GJ 536 is a high proper motion early M-dwarf at a distance of 10 pc from the Sun (van Leeuwen 2007). Because of its high proper motion and its proximity this star shows a secular acceleration of 0.24 m s^{-1} yr^{-1} (Montet et al. 2014). Its moderately low activity combined with its moderate rotation period, of more than 40 days (Suárez Mascareño et al. 2015, 2016), makes it a very interesting candidate to search for rocky planets. For this star we are using 141 HARPS and 12 HARPS-N spectra coming from 145 individual nights along 11.9 years, with 359 ASAS photometric exposures coming from 354 nights along 8.6 years (Fig. 3.31). The three time series, of the S_{MW} and H_α indexes, and the light

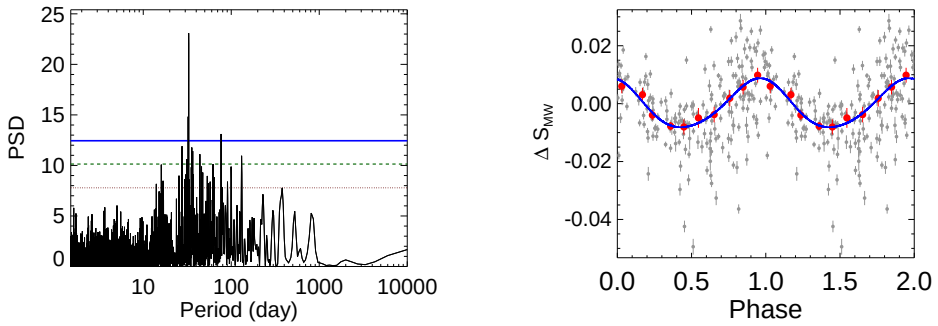

Figure 3.27: Periodogram of the residuals of the S_{MW} index time series of the star HD 176986 (left panel) and phased curve using the 32.8 days periodicity (right panel). For a detailed description see Fig. 3.16.

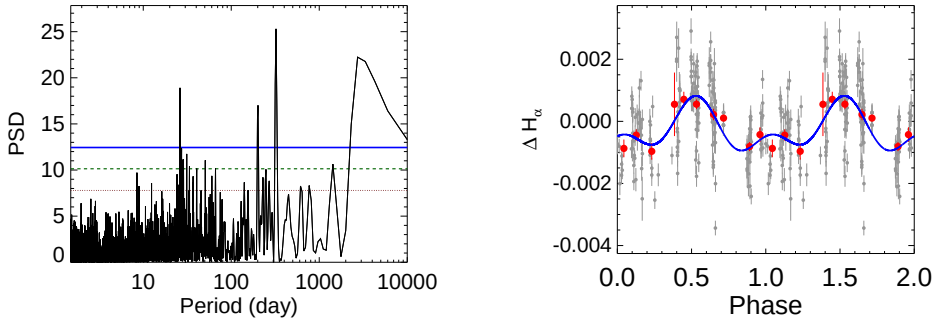

Figure 3.28: Periodogram of the H_α index time series of the star HD 176986 (left panel) and phased curve using the 6.8 years periodicity (right panel). For a detailed description see Fig. 3.16.

curve, show a variability beyond what can be explained by the error bars. An F-test returns a negligible probability – much smaller than the 0.1% for the spectroscopic indicators and the photometry – of that being the case.

The S_{MW} index time series show several significant periodicities, being the most important one a 795.2 ± 1.5 days (2.2 years) cycle with a semi amplitude of 0.0996 ± 0.0017 detected with a FAP smaller than the 0.1% (Fig. 3.32). This periodicity is consistent with those of flip-flop cycles in solar type stars, but this kind of cycles are not very studied in the case of M-dwarfs. The presence of a longer period less significant feature in the periodogram might imply the presence of a global cycle, but more measurements are needed to confirm it.

After subtracting the 2.2 yr cycle it shows a clear 43.794 ± 0.005 days

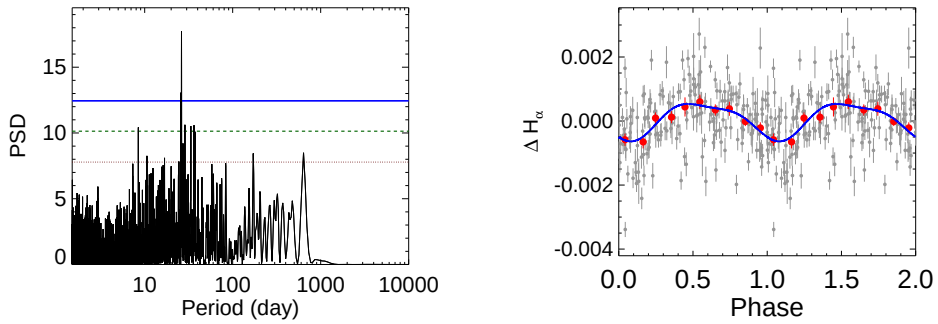

Figure 3.29: Periodogram of the residuals of the H_α index time series of the star HD 176986 (left panel) and phased curve using the 26.20 days periodicity (right panel). For a detailed description see Fig. 3.16.

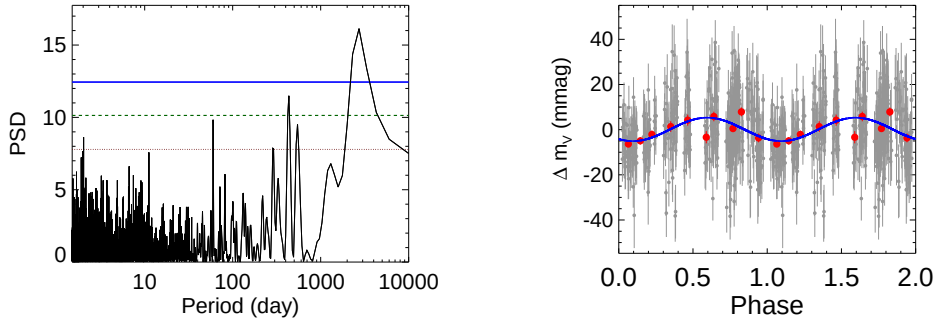

Figure 3.30: Periodogram of the residuals of the m_V light-curve of the star HD 176986 (left panel) and phased curve using the 7.9 years periodicity (right panel). For a detailed description see Fig. 3.16.

period signal with a semi amplitude of 0.0704 ± 0.0016 detected also with a FAP smaller than the 0.1% (Fig. 3.33). This measurement is consistent with the rotation of a moderately quiet M-dwarf, and with the values published by Suárez Mascareño et al. (2015, 2016).

As in the case of HD 176986, subtracting the rotation signal leaves us with a very similar signal probably related with activity features at different latitudes. The second signal in this case is of 45.400 ± 0.008 days with a semi amplitude of 0.0494 ± 0.0016 and it is once again detected with a FAP smaller than the 0.1% (Fig. 3.33).

No other significant signals are found after subtracting the last one.

The analysis of the H_α index time series shows a long-term cycle of 912.2 ±

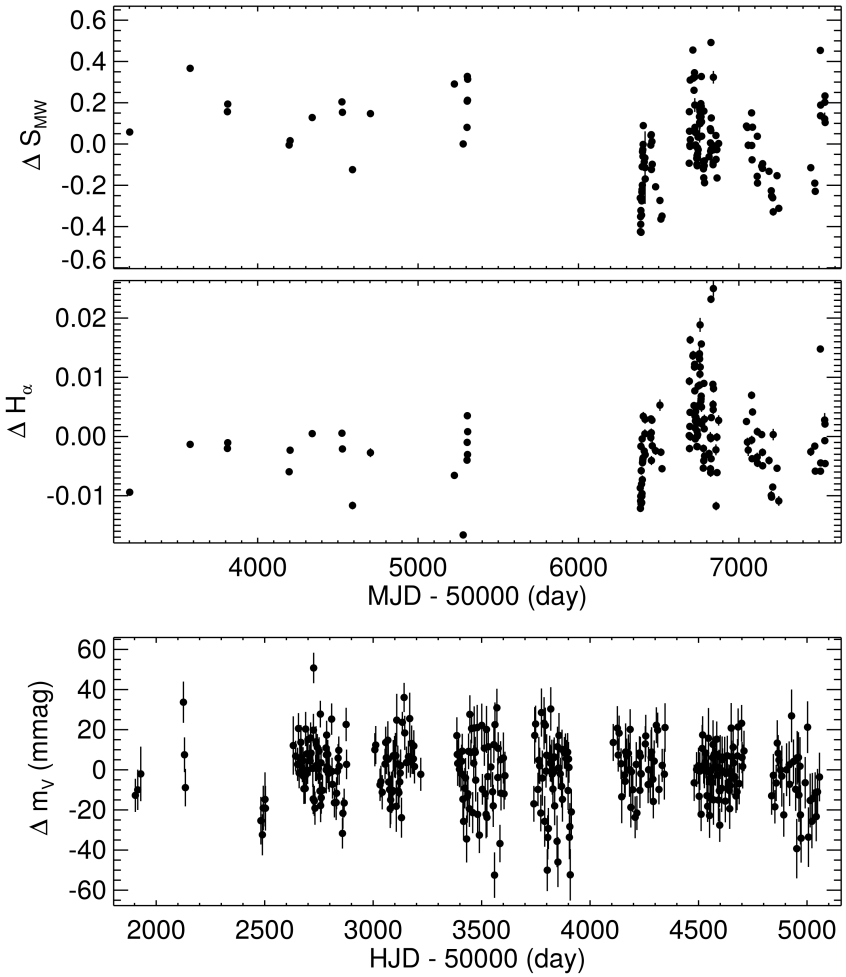

Figure 3.31: S_{MW} index and H_α index time series (upper panel) and photometric measurements (lower panel) for the star GJ 536.

2.2 days (2.5 years) with a semi amplitude of 0.00485 ± 0.00016 detected with a FAP smaller than the 0.1% (Fig. 3.35). The length of the cycle is more than 100 days apart from the one measured in the S_{MW} index.

Subtracting the cycle leaves us with a modulation of 42.953 ± 0.007 days with a semi amplitude of 0.00491 ± 0.00011 detected with a FAP smaller than the 0.1% (Fig. 3.36). This measurement is compatible with the rotational modulation detected in the S_{MW} index.

No more significant signals are found in the H_α index dataset.

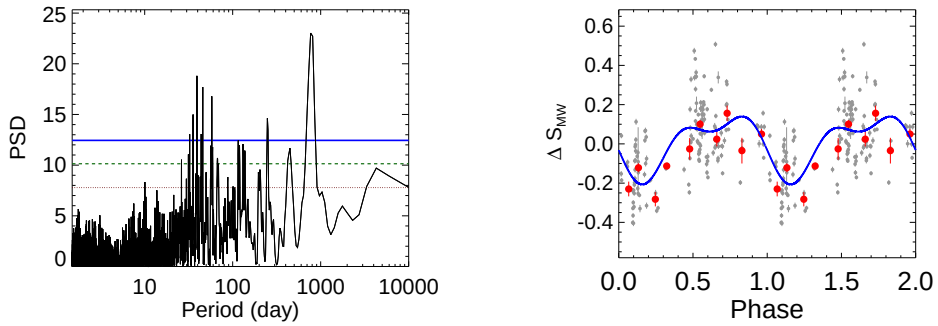

Figure 3.32: Periodogram of the S_{MW} index time series of the star GJ 536 (left panel) and phased curve using the 2.2 years periodicity (right panel). For a detailed description see Fig. 3.16.

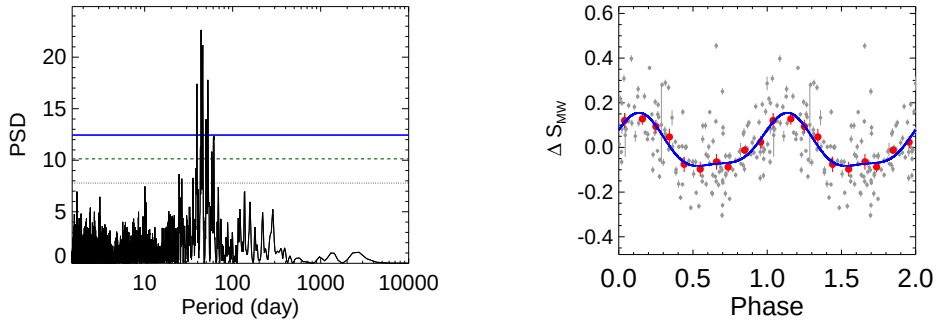

Figure 3.33: Periodogram of the residuals of the S_{MW} index time series of the star GJ 536 (left panel) and phased curve using the 43.8 days periodicity (right panel). For a detailed description see Fig. 3.16.

The analysis of the ASAS photometric light curve yields a rotational modulation of 43.326 ± 0.050 days with a semi amplitude of 5.98 ± 0.96 mmag with a FAP smaller than the 0.1% (Fig. 3.37). The measurement is compatible with those obtained using the S_{MW} and H_α indexes.

No more significant signals are found in the photometric data.

The M-dwarf GJ 536 shows a magnetic cycle of $\sim$ 2.3 years. A length compatible with that of a flip-flop cycles in solar type stars. For M dwarfs the information about magnetic cycles is scarce so we cannot rule out the possibility of this cycle being a short global cycle. The star rotates with a period of $\sim$ 43 days which is a rather long period for an early M dwarf.

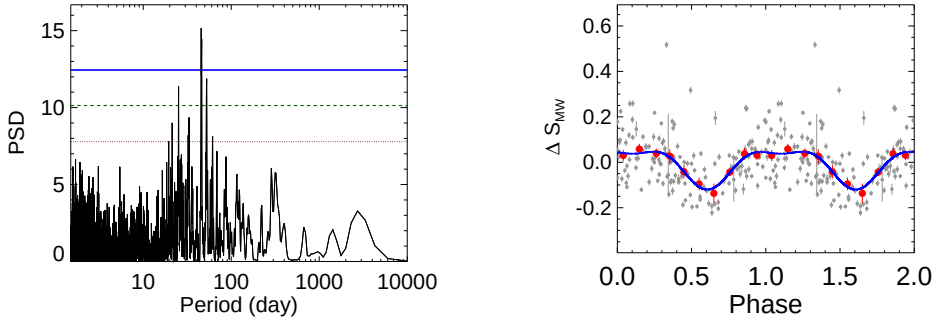

Figure 3.34: Periodogram of the residuals of the S_{MW} index time series of the star GJ 536 (left panel) and phased curve using the 45.4 days periodicity (right panel). For a detailed description see Fig. 3.16.

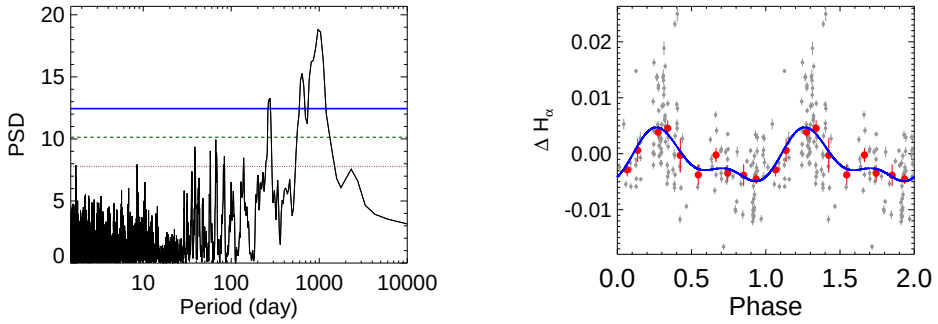

Figure 3.35: Periodogram of the H_α index time series of the star GJ 536 (left panel) and phased curve using the 2.50 years periodicity (right panel). For a detailed description see Fig. 3.16.

GJ 3998

GJ 3998 is a moderately low activity ($\log_{10}(R'_{\rm HK}) = -5.00$) M1 star (Maldonado et al. 2015) located at 17.8 pc (van Leeuwen 2007). The dataset for this star consists in 6 HARPS and 152 HARPS-N spectroscopic measurements distributed in 153 nights over 7.5 years and 554 ASAS photometric measurements taken in 441 nights over 7.1 years (Fig. 3.38). All three time series show variability unexplained by the error bars. An F-test yields probabilities smaller than the 0.1% for the error bars being enough to explain the observed variations.

The analysis of time series reveals a 499.5 ± 1.7 days (1.4 years) periodicity

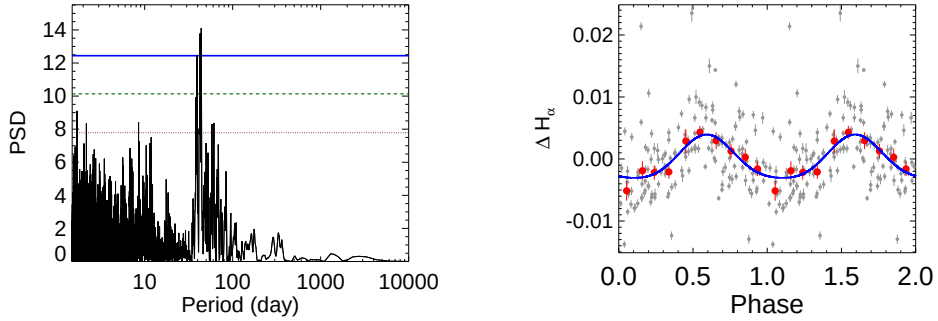

Figure 3.36: Periodogram of the residuals of the H_α index time series of the star GJ 536 (left panel) and phased curve using the 43.0 days periodicity (right panel). For a detailed description see Fig. 3.16.

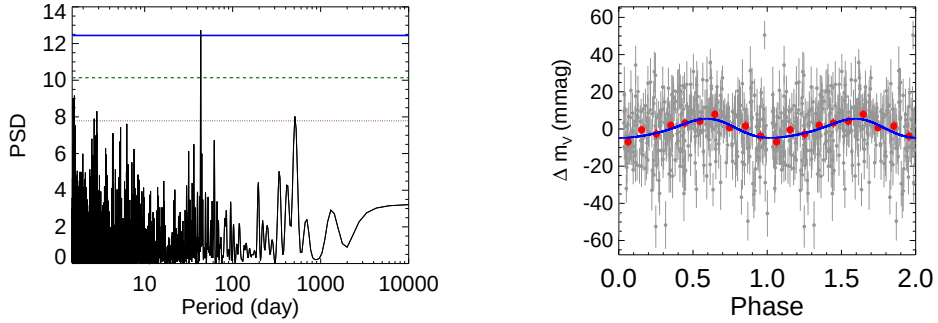

Figure 3.37: Periodogram of the m_V time series of the star GJ 536 (left panel) and phased curve using the 43.3 days periodicity (right panel). For a detailed description see Fig. 3.16.

with a semi amplitude of 0.13345 ± 0.0034 detected with a FAP smaller than the 0.1% (Fig. 3.39). The detected signal is consistent with a flip-flop cycle in a solar-type star. But considering that the reported cycles in M-dwarfs are only a few and of very different shapes and lengths, and that there does not appear to be any other longer cycle, this might be also the sign of a very short global cycle. The detected signal is clearly not sinusoidal, which is not unexpected for cycle related signals.

The subtraction of the cycle signal reveals the presence of a second periodicity of 30.486 ± 0.017 days with a semi amplitude of 0.0764 ± 0.0030 detected with a FAP better than the 0.1% (Fig. 3.40). This periodicity is consistent with the typical rotation for an early M-dwarf of the activity level of GJ 3998.

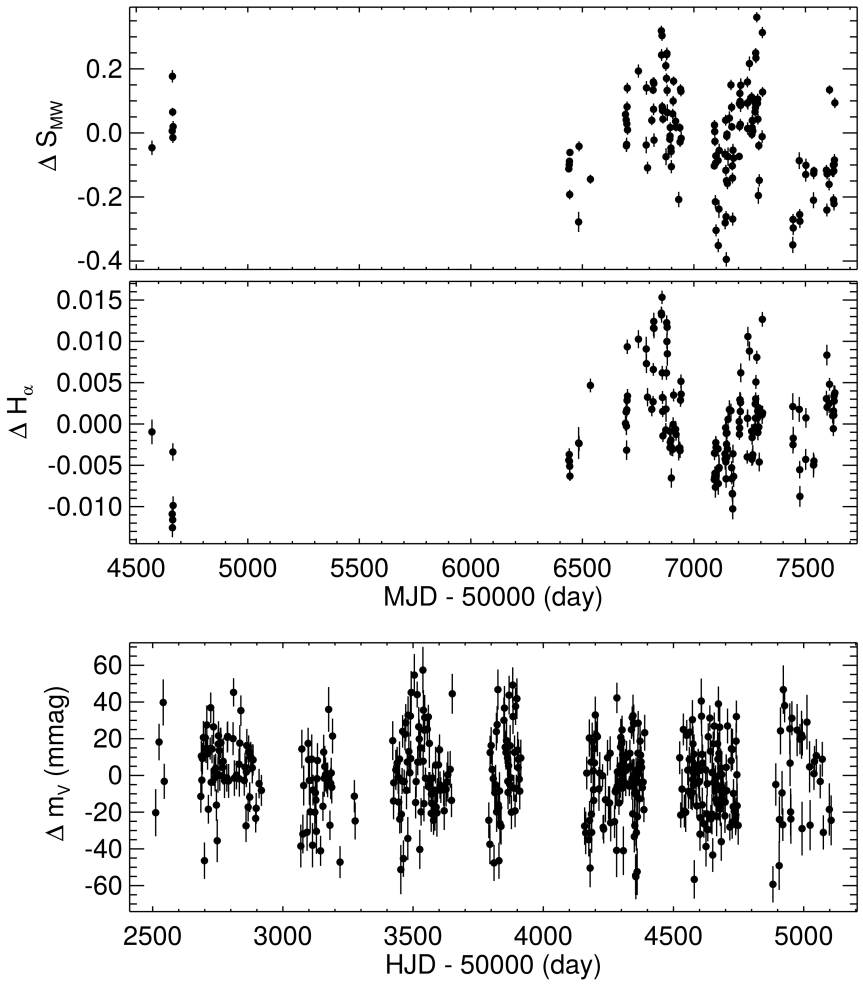

Figure 3.38: S_{MW} index and H_α index time series (upper panel) and photometric measurements (lower panel) for the star GJ 3998.

The signal is again not sinusoidal, which is something expected for rotation periodicities (Dumusque et al. 2011).

No more significant signals are found after subtracting the two previously mentioned signals.

The analysis of the H_α index time series shows the presence of a magnetic cycle of 606.8 ± 5.1 days (1.7 years) with a semi amplitude of 0.00586 ± 0.00018 detected with a FAP better than the 0.1% (Fig. 3.41). This cycle seems to be

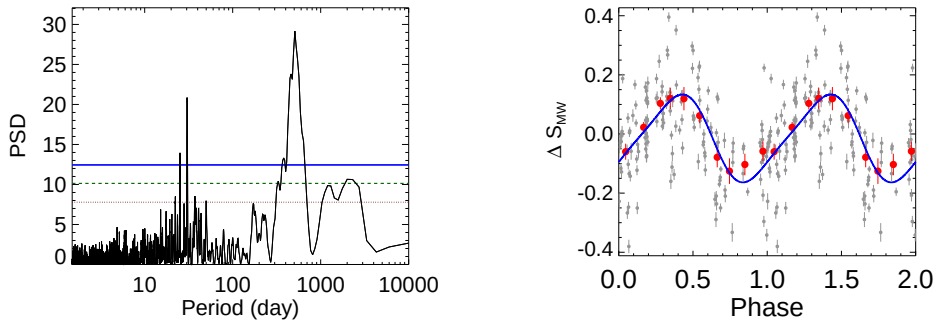

Figure 3.39: Periodogram of the S_{MW} index time series of the star GJ 3998 (left panel) and phased curve using the 1.4 years periodicity (right). For a detailed description see Fig. 3.16.

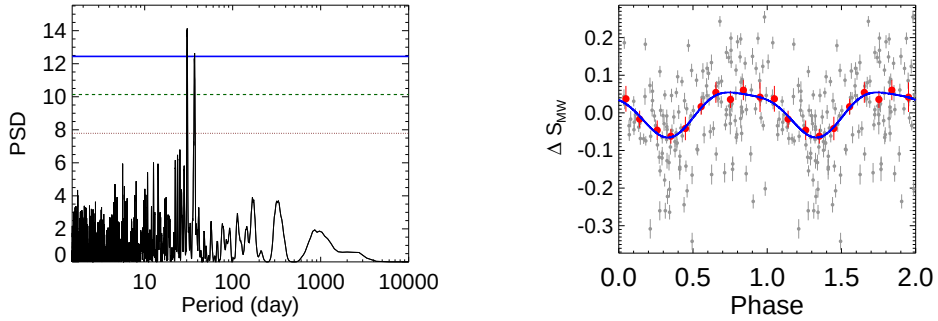

Figure 3.40: Periodogram of the residuals of the S_{MW} index time series of the star GJ 3998 (left panel) and phased curve using the 30.5 days periodicity (right). For a detailed description see Fig. 3.16.

the analogous of the 500 days cycle measured in the S_{MW} index time series. The 100 days difference might imply that the periodicity is still not perfectly defined in our dataset.

The H_α index data also shows a 27.853 ± 0.014 days periodicity with a semi amplitude of 0.00339 ± 0.00016 and a FAP smaller than the 1% (Fig. 3.42). This signal is compatible with a rotational modulation similar to the one measured in the S_{MW} index, but originated at latitudes closer to the equator.

No more significant signals are found in the H_α dataset.

The analysis of the photometric data does not show any significant periodic signal.

GJ 3998 is a moderately quiet M dwarf that shows a magnetic cycle of $\sim$

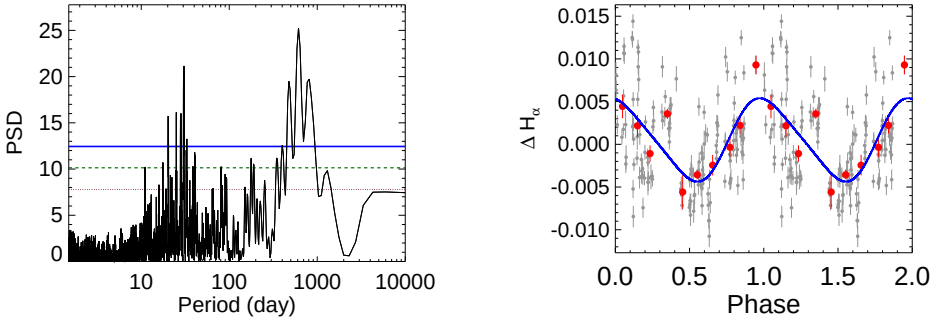

Figure 3.41: Periodogram of the H_α index time series of the star GJ 3998 (left panel) and phased curve using the 1.7 years periodicity (right panel). For a detailed description see Fig. 3.16.

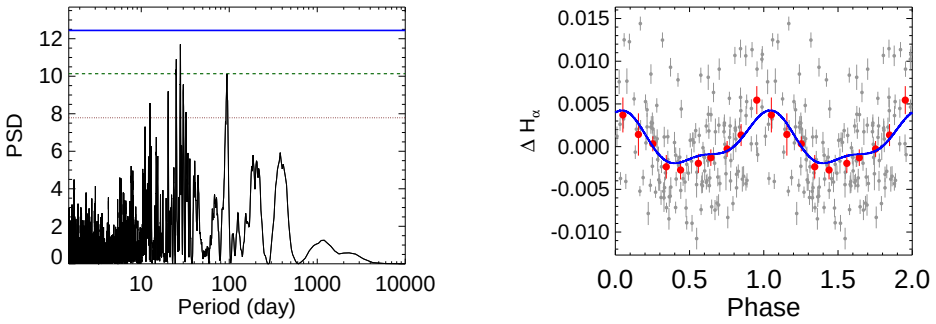

Figure 3.42: Periodogram of the residuals of the H_α index time series of the star GJ 3998 (left panel) and phased curve using the 27.9 days periodicity (right panel). For a detailed description see Fig. 3.16.

550 days, which would be compatible with a flip-flop cycle in a solar type star. The star rotates at 29.2 ± 1.9 days.

3.3 Results and Discussion

The previous analysis of variability in photometric time series provided a collection of magnetic cycles for 105 stars and rotation periods for 123 stars, out of which 82 are low activity M-type stars, for which only a few tens of magnetic cycles are reported in the literature. Table 3.5 shows the results obtained by the previous analysis.

We measured the magnetic cycles for 18 G-type stars for which we found a mean cycle length of 9.7 yr with a dispersion of 4.6 yr. We found a mean cycle length of 8.6 yr with a dispersion of 3.2 years for 25 K-type stars. A mean cycle length of 6.8 yr with a dispersion of 5.8 yr for 48 early M-type stars, and we found a mean cycle length of 6.1 yr with a dispersion of 2.4 yr for 13 mid M-type stars. We note that we might be mixing some flip-flop cycles along with the global cycles, but in most cases we do not find multiple cycles making it difficult to distinguish between the two types. Subsequently, we measured the rotation periods for 3 F-type stars with a mean measured rotation period of 12.3 days with a dispersion of 3.2 days, 21 rotation periods in G-type stars with a mean rotation period of 25.0 days and a dispersion of 5.2 days. For 25 K-type stars we measured a typical rotation of 25.3 with a dispersion of 13.7 days. For 61 early M-type stars, we measured an average rotation period of 37.2 days with a dispersion of 20.1 days, and an average rotation period of 67.0 days with a dispersion of 53.4 days for 13 mid M-type stars.

Table 3.5: Long-term cycles and rotation periods measured in this work for the stars in our sample. Periods are the mean periods of the measurements of the different activity proxies. Errors are the standard deviation of the different measurements. Stars are grouped by spectral type.

Star	$\log_{10}(R'_{\rm HK})$	P_{cycle} $(years)$	FAP %	P_{rot} $(days)$	FAP %
HD 25171	–4.89 ± 0.07			13.7 ± 0.1	< 10
HD 19994	–4.84 ± 0.02			8.7 ± 0.1	< 10
HD 1581	–4.84 ± 0.01	> 10	< 0.1	14.6 ± 0.1	< 0.1
HD 197210	–4.82 ± 0.02	16.2 ± 2.4	< 0.1	24.2 ± 0.1	< 0.1
		5.3 ± 1.1	< 0.1		
HD 134060	–4.91 ± 0.01	12.6 ± 3.5	< 1	23.9 ± 1.2	< 0.1
HD 7134	–4.87 ± 0.01	11.4 ± 2.0	< 0.1		
HD 1388	–4.89 ± 0.01	13.4 ± 6.0	< 0.1	22.9 ± 0.1	< 1
HD 10180	–4.91 ± 0.02	13.0 ± 1.2	< 10	27.2 ± 3.3	< 0.1

Continued on next page

Table 3.5 – *Continued from previous page*

		4.1 ± 0.4			
HD 30495	–4.50 ± 0.03			11.8 ± 3.0	< 0.1
HD 2071	–4.83 ± 0.02	11.2 ± 3.6	< 0.1	23.5 ± 4.7	< 0.1
HD 1320	–4.80 ± 0.02	3.3 ± 0.2	< 10	29.6 ± 1.0	< 10
HD 21019	–5.00 ± 0.03			29.5 ± 0.1	< 1
HD 41248	–4.80 ± 0.03			23.8 ± 4.7	< 0.1
HD 1461	–4.95 ± 0.02	8.6 ± 1.6	< 0.1	31.7 ± 0.1	< 0.1
HD 146233	–4.85 ± 0.03	8.6 ± 1.5	< 0.1	23.2 ± 1.7	< 0.1
HD 12264	–4.56 ± 0.03	16.0 ± 5.6	< 0.1	15.0 ± 0.1	< 0.1
		2.5 ± 0.3	< 0.1		
HD 4915	–4.76 ± 0.02	10.2 ± 1.0	< 0.1	21.8 ± 5.0	< 0.1
HD 59468	–4.95 ± 0.02	16.3 ± 1.1	< 0.1	23.1 ± 3.5	< 0.1
HD 115617	–4.93 ± 0.02	15.9 ± 0.1	< 0.1	30.3 ± 0.1	< 0.1
		4.3 ± 0.1	< 0.1		
HD 20794	–4.92 ± 0.01	11.4 ± 3.3	< 0.1	30.1 ± 0.1	< 0.1
HD 190248	–5.06 ± 0.02	9.8 ± 0.7	< 0.1	20.5 ± 0.1	< 0.1
		2.0 ± 0.1	< 0.1		
HD 161098	–4.83 ± 0.02	7.8 ± 0.5	< 0.1	28.1 ± 0.7	< 0.1
		2.5 ± 0.1	< 1		
HD 10700	–4.91 ± 0.01	8.2 ± 0.5	< 0.1	31.9 ± 1.8	< 0.1
		2.2 ± 0.1	< 0.1		
HD 7438	–4.74 ± 0.02			27.1 ± 0.4	< 0.1
HD 63765	–4.77 ± 0.05	12.9 ± 4.9	< 0.1	27.0 ± 3.0	< 0.1
HD 8389 A	–5.06 ± 0.04	13.7 ± 2.2	< 0.1	26.4 ± 2.6	< 0.1
HD 220256	–5.00 ± 0.04	16.3 ± 3.2	< 0.1	44.7 ± 4.8	< 0.1
HD 203384	–4.99 ± 0.03	6.7 ± 0.1	< 0.1	32.5 ± 13.3	< 0.1
		2.3 ± 0.1	< 0.1		
CoRoT-7	–4.62 ± 0.07			22.5 ± 0.9	< 0.1
HD 26965	–4.92 ± 0.06	10.3 ± 1.0	< 0.1	32.7 ± 0.1	< 0.1
HD 82558	–3.99 ± 0.04	2.5 ± 0.1	< 1	1.60 ± 0.01	< 0.1
HD 129621	–4.93 ± 0.04	10.3 ± 0.5	< 1	34.7 ± 3.9	< 0.1
HD 20165	–4.97 ± 0.05			32.2 ± 6.6	< 0.1
HD 155885	–4.60 ± 0.03	6.2 ± 0.1	< 0.1		
HD 224789	–4.43 ± 0.02	7.1 ± 0.9	< 0.1	16.8 ± 0.3	< 0.1
HD 204941	–4.97 ± 0.03	7.2 ± 0.1	< 0.1	26.3 ± 0.2	< 0.1
V 660 Tau		7.1 ± 0.2	< 0.1	0.23 ± 0.01	< 0.1
HD 4628	–4.94 ± 0.05			40.1 ± 0.3	< 1

Continued on next page

Table 3.5 – *Continued from previous page*

HD 40307	–5.05 ± 0.05	10.8 ± 1.6	< 0.1	26.2 ± 10.3	< 0.1
HD 220339	–4.85 ± 0.05	11.2 ± 1.2	< 0.1	32.0 ± 4.6	< 0.1
HD 22049	–4.45 ± 0.03			11.5 ± 0.01	< 0.1
HD 176986	–4.83 ± 0.03	6.8 ± 0.7	< 0.1	30.2 ± 2.0	< 0.1
HD 32147	–5.03 ± 0.05	5.8 ± 0.5	< 0.1		
HD 170493	–4.88 ± 0.06	9.3 ± 0.1	< 0.1	40.6 ± 0.1	< 0.1
HD 45088		7.0 ± 0.1	< 0.1		
HD 104067	–4.75 ± 0.03	7.7 ± 1.3	< 0.1	29.8 ± 3.1	< 1.0
HD 131977	–4.85 ± 0.03	5.1 ± 0.2	< 0.1		
HD 215152	–4.94 ± 0.05	7.7 ± 0.5	< 0.1	36.5 ± 1.7	< 0.1
V 410 Tau				1.9 ± 0.1	< 0.1
HD 125595	–4.77 ± 0.03	5.9 ± 0.6	< 0.1	38.7 ± 1.0	< 0.1
HD 118100		9.3 ± 0.4	< 0.1	3.9 ± 0.1	< 0.1
HD 209100	–4.78 ± 0.03	6.5 ± 1.8	< 0.1	27.0 ± 6.4	< 0.1
HIP 5158	–4.92 ± 0.03	8.7 ± 2.6	< 0.1		
HD 85512	–4.95 ± 0.04	15.1 ± 5.3	< 0.1	45.8 ± 5.2	< 0.1
HD 113538	–4.84 ± 0.05	6.6 ± 0.6	< 0.1	36.3 ± 0.2	< 1
GJ 229	–4.91 ± 0.04	8.4 ± 0.3	< 0.1	26.7 ± 2.4	< 0.1
GJ 846	–4.81 ± 0.03	8.5 ± 1.1	< 0.1	26.3 ± 5.6	< 1
GJ 184	–5.09 ± 0.03			41.5 ± 20.6	< 1
GJ 3942	–4.46 ± 0.03	1.1 ± 0.1	< 1	16.3 ± 0.2	< 0.1
GJ 4057	–5.03 ± 0.03	3.7 ± 0.1	< 0.1	27.0 ± 0.7	< 0.1
GJ 9482	–4.73 ± 0.02	10.0 ± 0.7	< 0.1	15.1 ± 0.3	< 1
GJ 9404	–4.73 ± 0.05	3.1 ± 0.2	< 0.1		
GJ 676 A	–4.96 ± 0.03	9.2 ± 0.6	< 0.1	35.0 ± 11.8	< 0.1
		3.9 ± 0.4	< 0.1		
GJ 119 A	–4.77 ± 0.05	2.0 ± 0.1	< 0.1	30.9 ± 1.0	< 1
GJ 784	–4.83 ± 0.04	1.7 ± 0.1	< 0.1	22.3 ± 0.9	< 0.1
GJ 803	–3.97 ± 0.05	7.6 ± 0.4	< 0.1	4.9 ± 0.1	< 0.1
GJ 740	–4.87 ± 0.04	7.1 ± 0.2	< 0.1	36.8 ± 2.3	< 0.1
GJ 685	–4.78 ± 0.05			18.0 ± 0.1	< 0.1
GJ 720 A	–4.89 ± 0.04	5.4 ± 0.1	< 0.1	35.5 ± 1.6	< 0.1
GJ 4306	–4.45 ± 0.03	6.6 ± 4.0	< 0.1		
GJ 21	–4.73 ± 0.03			17.4 ± 0.1	< 1
GJ 3822	–4.71 ± 0.04	6.9 ± 1.1	< 0.1	18.0 ± 0.6	< 0.1
GJ 694.2	–4.45 ± 0.03			18.4 ± 7.6	< 1
GJ 9689	–4.86 ± 0.04			39.6 ± 3.2	< 1

Continued on next page

Table 3.5 – *Continued from previous page*

GJ 1	–5.53 ± 0.07			56.8 ± 5.5	< 0.1
GJ 514	–5.11 ± 0.04	9.9 ± 3.8	< 0.1	30.0 ± 0.9	< 0.1
GJ 536	–4.99 ± 0.04	2.3 ± 0.2	< 0.1	43.9 ± 1.1	< 0.1
GJ 3997	–5.15 ± 0.05	2.4 ± 0.1	< 0.1	39.8 ± 14.3	< 0.1
GJ 606	–4.89 ± 0.06			21.1 ± 0.1	< 0.1
GJ 3998	–5.00 ± 0.04	1.4 ± 0.1	< 0.1	29.2 ± 1.9	< 0.1
GJ 1074	–4.84 ± 0.04			46.5 ± 2.8	< 0.1
GJ 832	–5.23 ± 0.06	13.2 ± 4.2	< 0.1	39.2 ± 9.4	< 0.1
GJ 239		4.9 ± 0.4	< 0.1		
GJ 205	–4.75 ± 0.03	10.8 ± 1.1	< 0.1	34.8 ± 1.3	< 0.1
		3.9 ± 0.3	< 0.1		
GJ 49	–4.83 ± 0.02			18.7 ± 0.1	< 10
GJ 9138	–4.82 ± 0.04	1.7 ± 0.1	< 0.1	29.3 ± 0.4	< 0.1
GJ 16	–5.02 ± 0.05	5.5 ± 0.4	< 0.1		
GJ 15 A	–5.27 ± 0.05	2.0 ± 0.1	< 0.1	46.5 ± 6.5	< 0.1
GJ 526	–5.06 ± 0.05	9.9 ± 2.8	< 0.1	52.1 ± 12.0	< 0.1
GJ 693	–5.70 ± 0.13	5.6 ± 0.3	< 0.1	88.5 ± 5.3	< 1
GJ 908	–5.38 ± 0.06			50.1 ± 4.6	< 1
GJ 880	–4.92 ± 0.04	9.9 ± 1.0	< 0.1	37.2 ± 6.7	< 0.1
GJ 382	–4.82 ± 0.04	13.6 ± 1.7	< 0.1	21.8 ± 0.1	< 0.1
GJ 2	–4.84 ± 0.04	2.2 ± 0.1	0.2	21.5 ± 1.5	< 0.1
GJ 410	–4.45 ± 0.05	5.6 ± 0.1	< 1		
GJ 47	–4.92 ± 0.06			34.3 ± 0.1	< 0.1
GJ 521	–4.72 ± 0.05			22.6 ± 7.9	< 1
GJ 507.1	–5.30 ± 0.04	2.2 ± 0.2	< 1	61.2 ± 16.9	< 1
GJ 1030	–4.85 ± 0.06			36.1 ± 0.1	< 0.1
GJ 588	–5.21 ± 0.05	5.2 ± 0.7	< 1	51.4 ± 6.1	< 0.1
GJ 176	–5.00 ± 0.05	5.9 ± 0.7	< 10	39.4 ± 1.0	< 0.1
GJ 162	–4.95 ± 0.05	3.9 ± 0.4	< 0.1	34.3 ± 1.7	< 0.1
GJ 552	–5.09 ± 0.04			34.2 ± 7.9	< 0.1
GJ 476	–5.21 ± 0.05			55.3 ± 0.1	< 0.1
GJ 4100	–4.86 ± 0.08			35.9 ± 0.1	< 0.1
GJ 3470	–4.91 ± 0.09			21.1 ± 1.0	< 1
GJ 674	–5.04 ± 0.07	10.1 ± 0.8	< 0.1	33.0 ± 0.7	< 0.1
GJ 388	–4.25 ± 0.12	9.3 ± 2.6	< 0.1	2.4 ± 0.1	< 1
GJ 752 A	–5.16 ± 0.05	9.2 ± 1.4	< 0.1	43.6 ± 4.0	< 0.1
GJ 625	–5.65 ± 0.07	1.5 ± 0.1	< 0.1	96.1 ± 8.4	< 0.1
GJ 408	–5.32 ± 0.05	5.3 ± 0.6	< 10		

Continued on next page

Table 3.5 – *Continued from previous page*

GJ 667 C	–5.61 ± 0.07	3.8 ± 0.1	< 0.1	103.9 ± 1.3	< 0.1
GJ 877	–5.28 ± 0.06	11.0 ± 1.1	< 0.1	58.1 ± 0.4	< 0.1
		1.5 ± 0.1	< 0.1		
GJ 357	–5.65 ± 0.10	7.2 ± 0.3	< 1	88.6 ± 23.4	< 0.1
GJ 358	–4.64 ± 0.05	9.7 ± 0.6	< 0.1	25.2 ± 0.1	< 0.1
		4.6 ± 0.1	< 0.1		
GJ 479	–4.85 ± 0.05	2.0 ± 0.1	< 0.1	26.0 ± 7.2	< 0.1
GJ 680	–5.29 ± 0.05	5.0 ± 0.2	< 0.1	45.3 ± 0.1	< 10
GJ 436	–5.27 ± 0.06	5.6 ± 0.2	< 1	38.8 ± 0.8	< 0.1
GJ 729	–4.35 ± 0.12	7.1 ± 0.1	< 0.1	2.9 ± 0.1	< 0.1
GJ 628	–5.47 ± 0.07	4.4 ± 0.2	< 0.1	64.5 ± 7.0	< 0.1
SkTM 1-1877	–4.32 ± 0.04	3.9 ± 1.1	< 0.1	7.6 ± 0.1	< 10
GJ 163	–5.30 ± 0.05			43.6 ± 3.6	< 0.1
GJ 273	–5.44 ± 0.05	6.6 ± 1.3	< 0.1	75.5 ± 16.0	< 0.1
GJ 849*	–5.14 ± 0.04	10.2 ± 0.9	< 0.1	39.2 ± 6.3	< 0.1
GJ 317	–5.26 ± 0.09	5.2 ± 0.3	< 0.1		
GJ 699	–5.93 ± 0.08	5.2 ± 0.8	< 0.1	148.6 ± 0.1	< 0.1
GJ 54.1	–5.11 ± 0.09			69.2 ± 0.1	< 0.1
GJ 234	–4.41 ± 0.22	5.9 ± 0.5	< 0.1	8.1 ± 0.1	< 1
LP 816-60	–5.14 ± 0.08	10.6 ± 1.7	< 10	51.9 ± 12.5	< 0.1
GJ 447	–5.62 ± 0.09	4.1 ± 0.3	< 10	165.1 ± 0.8	< 1
GJ 754	–5.59 ± 0.18	2.3 ± 0.5	< 0.1	131.5 ± 0.2	< 1
GJ 285	–3.99 ± 0.04	10.6 ± 0.4	< 0.1	2.8 ± 0.1	< 0.1
GJ 1214	–5.48 ± 0.14			78.2 ± 17.0	< 1
GJ 406		8.9 ± 0.2	< 0.1		
GJ 876	–5.30 ± 0.05	4.5 ± 0.2	< 0.1	84.1 ± 6.0	< 0.1
GJ 581	–5.75 ± 0.08	6.2 ± 0.9	< 0.1	132.5 ± 6.3	< 0.1
GJ 551	–5.15 ± 0.09	6.8 ± 0.3	< 0.1	83.2 ± 0.1	< 0.1

In order to put these results on a broader context we include in the discussion and and in the plots other FGKM stars with known cycles and rotation periods selected from Noyes et al. (1984), Baliunas et al. (1995), Lovis et al. (2011a) and Robertson et al. (2013). In total we will compare 320 stars with similar number of G-, K-, and M-type and far fewer F-type stars, with cycle measurements for 229 stars and rotation periods for 234 stars. Our aim is to study the distribution of cycle lengths and rotation periods for the different spectral types and the activity-rotation relationships.

Table 3.6: Statistics of the length of measured cycles after combining our measurements with the measurements from the literature

Sp. Type	N	Mean (yr)	Median (yr)	Dispersion (yr)
F	9	10.3	7.4	4.9
G	70	7.5	6.8	4.1
K	61	8.8	7.7	3.7
Early M	73	6.2	5.3	5.0
Mid M	16	6.0	5.9	2.4

3.3.1 Stellar Cycles

Figure 3.43 shows the distribution histogram of cycles by length and spectral type. We find that, like G-type stars, early M-type stars present a rather broad distribution with a peak at the 2-4 year bins, but K-type stars peak at the 6 year bin. The double peak seen in the K-type distribution might reveal information about global cycles (10 yr) and flip-flop cycles (6 yr). There are too few detections to see any particular behaviour for F-type and mid M-type stars. Table 3.6 shows the main statistics of the typical cycle for each spectral type.

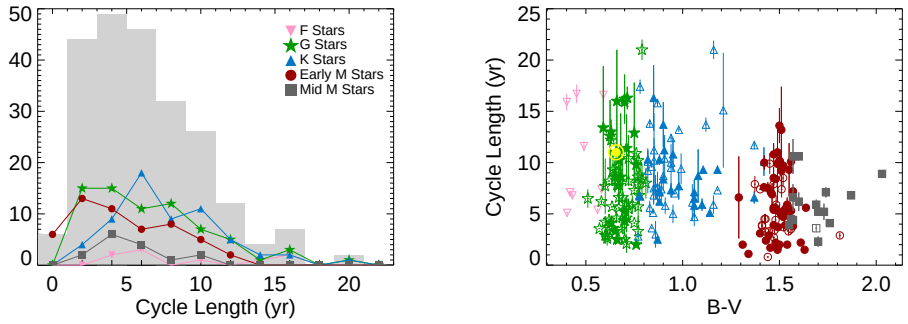

Figure 3.43: Distribution of cycle lengths (left panel) and evolution of the cycle lengths with the B-V colour (right panel) of the stars analysed in this work (filled symbols) and stars from the literature (open symbols). Grey filled columns show the global distribution while coloured lines the individual distributions.

Notes on individual stars

HD10180: Lovis et al. (2011a) provides a cycle measurement of 7.4 ± 1.2 yr by studying the variations in the Ca II $H\&K$ emission cores. Instead of that we find a 13.0 ± 1.2 and a 4.1 ± 0.4 yr variations. The 7.4 ± 1.2 yr signal was detected using considerably less data. It could by the first harmonic of the 13 yr signal.
HD155885: Hempelmann et al. (1995) and Saar & Brandenburg (1999) proposed cycles ranging from 5 to 6 yr, with large associated uncertainty. Our measurement of a 6.2 ± 0.1 yr photometric periodicity supports their previous claims.
HD63765: While we retrieve a 12.9 ± 4.9 yr cycle in the photometric light curve, Lovis et al. (2011a) found a periodicity of 6.1 ± 2.8 yr in the Ca II $H\&K$ emission time series. We did not find a 6 yr periodicity, but this measurement is compatible with the first harmonic of our measurement.
HD32147: Baliunas et al. (1995) found a 11.1 ± 0.2 yr cycle studying the Ca II $H\&K$ emission time series. Our 5.8 ± 0.5 yr measurement is compatible with the first harmonic of that cycle.
HD82558: Previous studies have reported different cycle lengths for this star, ranging from $\sim$ 2.5 up to $\sim$ 12 yr (Oláh et al. 2009). In our data we recover the $\sim$ 2.5 yr cycle, which might be a flip-flop cycle, and also evidence for an additional long-term trend.
GJ205: Savanov (2012) finds a 3.7 yr period cycle and some shorter periods. Our best fit comes from the superposition of two cycles, one of 10.8 ± 1.1 yr and another one of 3.9 ± 0.3 yr cycle. The short period cycle might be a flip-flop cycle.
GJ729: For this star we find two superimposed cycles. One of 7.1 ± 0.1 yr and a shorter cycle of 2.1 ± 0.1 yr. Again the short period cycle might be a flip-flop cycle.
GJ234: This is a close binary system composed of two low mass stars with a brightness difference of $\Delta m_K \sim 1.6$ and a separation of $\sim$ 1 arcsec (Ward-Duong et al. 2015). Although the photometric light curve is for the unresolved binary, the signal is likely dominated by the primary component given its dominance in the visible range. We ascribe the periodic signals detected in the light curve to the primary.
GJ581: Robertson et al. (2013) detects a 4.5 ± 0.3 yr cycle analysing the H_α time series whereas we detect a 6.2 ± 0.9 yr cycle in the photometry light curve.
GJ551: Cincunegui et al. (2007) claimed a 1.2 yr cycle for which we find no evidence in the photometric light curve. Instead we measure a clear 6.8 ± 0.3 yr cycle. Savanov (2012) found a 7.9 yr cycle.

Table 3.7: Statistics of rotation periods after combining our measurements with the measurements from the literature

Sp. Type	N	Mean (d)	Median (d)	Dispersion (d)
F	26	8.4	7.6	5.6
G	56	20.6	22.9	10.1
K	64	27.8	29.8	14.6
Early M	73	35.0	33.0	24.5
Mid M	15	71.6	69.2	54.4

3.3.2 Stellar Rotation

Figure 3.44 shows the distribution of rotation periods and Table 3.7 lists the typical periods and measured scatter. When looking at the rotation periods we find the envelope of the distribution growing steadily towards longer periods for later spectral types, and saturating at ~ 50 days K-type stars(see Fig. 3.44). M-type stars, especially mid-Ms, show larger scatter reaching periods longer than 150 days. This behaviour is also reflected in their extremely low chromospheric activity levels. Figure 3.8 shows the distribution of the $\log_{10} R'_{HK}$ against the colour B-V. For solar-type stars the lower envelope of the distribution goes around ~ -5.0, but M dwarfs reach a very low level of ~ -6.

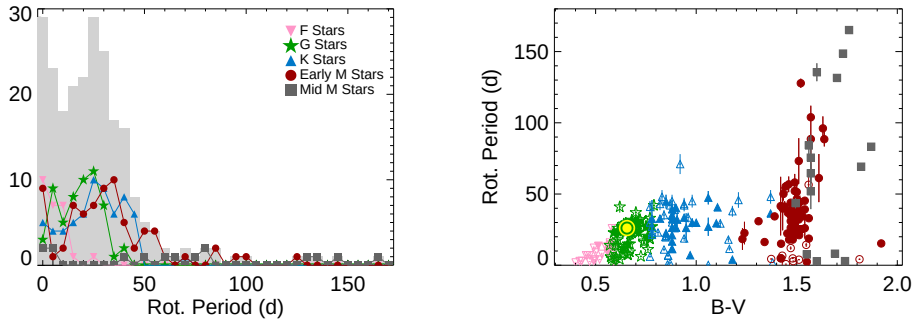

Figure 3.44: Distribution of rotation periods (left panel) and rotation periods vs B-V colour (right panel) of stars analysed in this work (filled symbols) and stars from the literature (open symbols).

3.4 Activity - rotation relation

Suárez Mascareño et al. (2015) proposed a rotation-activity relation for late-F- to mid-M-type main-sequence stars with $\log_{10} R'_{HK} \sim -4.50$ up to ~ -5.85. The new measurements presented in Tables 3.5, and the data from Noyes et al. (1984), Baliunas et al. (1995), and Lovis et al. (2011a) serve to extend and better define the relationship. Figure 3.45 shows the new measurements along with those the literature. These measurements are compatible for almost all late spectral types and levels of chromospheric activity, as F-type stars are the only clear outliers. Combining all data we can extend the relationship to faster rotators with levels of chromospheric activity up to $\log_{10} R'_{HK} \sim -4$ and we are able to give an independent relationship for each spectral type. The evolution of the duration of the rotation period as a function of the activity level has two different sl, with a turning point at $\log_{10} R'_{HK} \sim -4.5$. Figure 3.46 shows the measurements for every individual spectral type. Table 3.8 shows the coefficients of the best fit for every individual dataset assuming a relationship such as:

$$\log_{10}(P_{rot}) = A + B \cdot \log_{10} R'_{HK}, \tag{3.16}$$

where P_{rot} is in days. The typical residuals of the fit are smaller than 23 per cent of the measured periods for a given level of activity, for stars from G to mid M, and with residuals smaller than 39 per cent in the case of F-type stars. This relationship can be used to estimate the rotation period of stars with low levels of chromospheric activity for stars of F-M types.

Table 3.8: Parameters for Eq. 3.16. σ P is the typical residuals after the fit as a % of the measured rotation period.

Dataset	N	A	B	σP [%]
GKM ($\log_{10} R'_{HK} > -4.5$)	22	–5.933 ± 0.040	–1.574 ± 0.009	27
GKM ($\log_{10} R'_{HK} \leq -4.5$)	164	–2.428 ± 0.001	–0.791 ± 0.001	19
F	26	-2.336 ± 0.052	–0.693 ± 0.011	40
G ($\log_{10} R'_{HK} > -4.7$)	15	–11.092 ± 0.052	–2.695 ± 0.011	15
G ($\log_{10} R'_{HK} \leq -4.7$)	53	0.772 ± 0.003	–0.449 ± 0.001	17
K ($\log_{10} R'_{HK} > -4.6$)	18	–9.722 ± 0.070	–2.466 ± 0.016	22
K ($\log_{10} R'_{HK} \leq -4.6$)	43	–1.496 ± 0.004	–0.620 ± 0.001	16
M ($\log_{10} R'_{HK} > -4.5$)	8	–6.795 ± 0.046	–1.792 ± 0.010	55
M ($\log_{10} R'_{HK} \leq -4.5$)	67	–2.521 ± 0.002	–0.808 ± 0.001	21

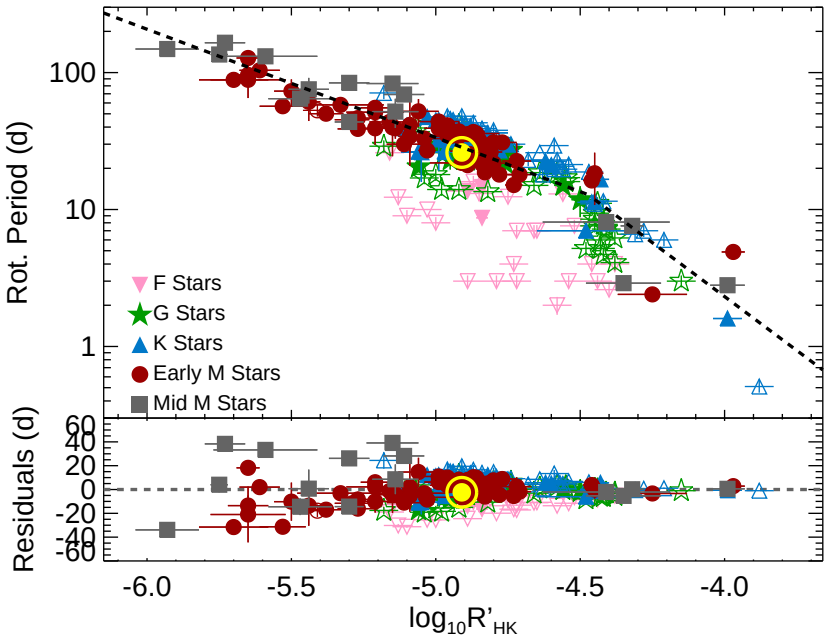

Figure 3.45: Rotation period vs. chromospheric activity level $\log_{10} R'_{HK}$. Filled symbols show the stars analysed in this work. The dashed line shows the best fit to the data, leaving out the F-type stars.

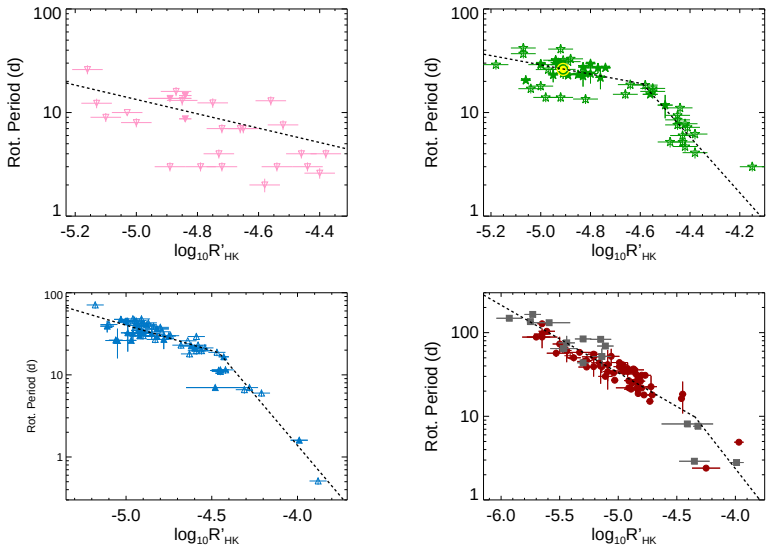

Figure 3.46: Rotation period vs. chromospheric activity level $\log_{10} R'_{HK}$ for each spectral type. Filled symbols show the stars analysed in this work. The dashed line shows the best fit to the data for each individual dataset.

3.5 Activity - amplitude of cycle relation

A relation between the cycle amplitude in Ca II$_{HK}$ data series and the mean activity level of the stars was proposed by Saar & Brandenburg (2002). It was found that stars with a higher mean activity level show also larger cycle amplitudes. We investigate in our sample the behaviour of the photometric amplitude of the cycle with the mean activity level.

Comparing the cycle amplitude with the $\log_{10} R'_{HK}$ we are able to see a weak tendency. Even if there is a large scatter, a trend such that the photometric amplitude of the cycle increases towards higher activity stars is found (see Figure 3.47). This agrees with the Saar & Brandenburg (2002) work.

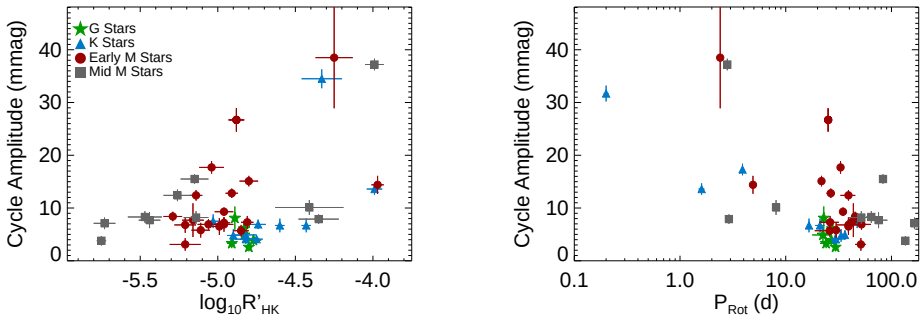

Figure 3.47: Measured cycle photometric amplitude vs. chromospheric activity level $\log_{10} R'_{HK}$.

When comparing the cycle amplitude with the rotation period we found a more clear correlation. While the scatter remains large, it is clear that the cycle amplitude decreases longer periods (see Figure 3.47). This is different to what Saar & Brandenburg (2002) found when studying the Ca II variations, where cycle amplitude saturation may occur.

3.6 Rotation-cycle relation

The existence of a relationship between the length of the magnetic cycle and the rotation period of stars has been studied for a long time. Baliunas et al. (1996) suggested P_{cyc}/P_{rot} as an observable to study how both quantities relate to each other. It was suggested that the length of the cycle scales as $\sim D^l$, where l is the slope of the relation and D is the dynamo number. Slopes that are different from ~ 1 would imply a correlation between the length of the cycle and the rotation period.

Figure 3.48 shows results on a log-log scale of P_{cyc}/P_{rot} versus $1/P_{rot}$ for all the stars for which we were able to determine both the rotation period and length of the cycle. The slope for our results is 1.01 ± 0.06, meaning no correlation between both quantities. However, we cover from early-G to late-M stars, including main-sequence and pre-main-sequence stars, with rotation periods ranging from ~ 0.2 to more than ~ 160 days. Previous works that found correlations were based on more homogeneous, and thus suitable samples, to study this relationship. For stars with multiple cycles we choose the global cycle (longer cycle), but the possibility of some of the short period cycles being flip-flop cycles cannot be ruled out.

If we restrict our analysis to main-sequence FGK stars, we obtain a slope of 0.84 ± 0.05, meaning that there is a weak correlation between both quantities. This is compatible with the result of 0.81 ± 0.05 from Oláh et al. (2009) and implies a weaker correlation in our sample than that found by Baliunas et al. (1996) who measured a slope of 0.74. This supports the idea that there is a common dynamo behaviour for FGK stars, which does not apply to the M-dwarf stars for which we, as Savanov (2012), do not find a correlation.

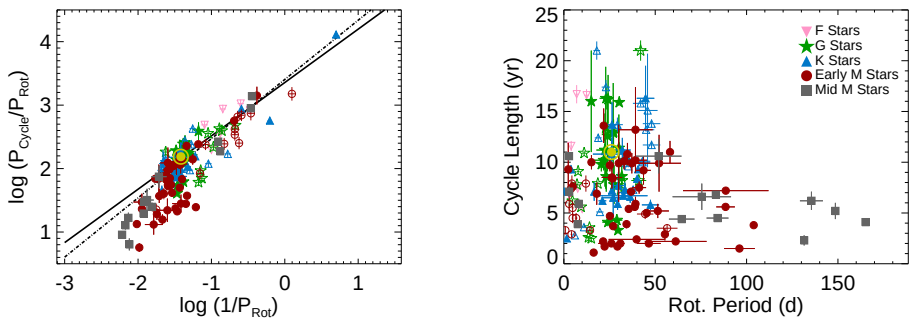

Figure 3.48: P_{cyc}/P_{rot} versus $1/P_{rot}$ in log-log scale. Filled dots represent main-sequence stars while empty circles stand for pre-main-sequence stars. The dashed line shows the fit to the full dataset. The solid line shows the fit to the main-sequence stars with radiative core.

In a direct comparison of the length of the cycle with the rotation period, we see an absence of long cycles for extreme slow rotators. Figure 3.48 shows the distribution of cycle lengths against rotation periods. While the cycle lengths of those stars with rotation periods below the saturation level of ~ 50 days distribute approximately uniformly from ~ 2 to ~ 20 years, stars rotating slower than ~ 50 days show only shorter cycles. At this point, it is unclear whether or not this behaviour is real or is related to a selection or observational

bias. The number of stars with both rotation and cycle measured in this region is small, and the time span of the observation is shorter than 10 years. Further investigation is needed to clarify the actual distribution.

4

Radial Velocity Analysis

We analyse the radial velocity time series of 133 stars of our sample searching for planetary induced signals and stellar activity induced signals. We report the detection of 6 new planets around the stars HD 1581, HD 161098, HD 176986, GJ 536 and GJ3998 and the tentative detection of a 7th planet around the star HD 161098. We also suggest the possible presence of 5 additional candidates that still require further analysis and observations. We investigate the activity induced signals related to rotation and magnetic cycles in late type stars (FGKM). We determine that 46 stars have a measurable signal induced by its rotation, Being 1 of them F-type stars, 8 of them G-type stars, 11 of them K-type, 23 early M-type stars and 3 mid-M type. We report an empirical relationship, with some degree of spectral type dependency, between the level of chromospheric emission measured by the $\log_{10}(R'_{\rm HK})$ and the measured amplitude. We report also a strongly spectral type dependent relationship between the amplitude of the chromospheric measured signal and the amplitude of the radial velocity activity induced signal. We find that for a given degree of chromospheric activity (i.e. a given rotational period) M-type stars tend to induce larger rotational related radial velocity signals than G and K-type stars.

4.1 Radial Velocities

Radial velocity (RV) measurements in the HARPS standard pipeline are determined by a Gaussian fit of the cross correlation function of the spectrum with a stellar template (Pepe et al. 2000) which has a value of 0 for the continuum and a certain height for each individual line. There is one mask available for G-type stars, another one for K-type stars and a third one for M-type stars. Every line is at laboratory wavelength. The mask is shifted a certain velocity and at every step the spectrum is projected through the mask and integrated giving the sum of all the information projected through the lines. When the shift matches the

real shift of the spectrum we get a minimum of the function. The process is performed order by order, and then the cross correlation functions (CCF) of each individual order are summed to average the line shifts of the whole spectrum. The sum is a weighted sum using the flux of the individual orders as the weight. A template for every individual star built using the co-added spectra of all the observations of a given star, and its flux distribution is used to ensure that every order has the same weight for each individual observation. This ensures that the spectral spectral flux distribution does not change depending on the atmospheric conditions, which could affect the radial velocities by up to 1 m/s. The process also rejects the orders affected by strong telluric lines, and the first orders in blue part of the CCD in the case of the M-dwarfs, as the flux is too low to perform an accurate measurement.

The CCF has a Gaussian shape for the case of FGK stars, allowing for a straightforward Gaussian fit to measure the minimum of the function. In the case of M-dwarfs, due to the huge number of line blends, the cross correlation function is not Gaussian resulting in a less precise Gaussian fit which might cause distortions in the radial velocity measurements and FWHM of the CCF. To deal with this issue we relied in using a slightly more complex model for the CCF fitting, a Gaussian function plus a second order polynomial (Fig. 4.1) using only the central region of the CCF function. We re-calculated the velocities for every star, independently of its stellar type. We use different windows centred at the minimum of the CCF for the fit depending on the spectral type of the star. A 22.5 kms^{-1} window for F-type stars, a 20.0 kms^{-1} window for G-type stars, a 17.5 kms^{-1} window for K-type stars and a 14 kms^{-1} window for M-type stars. These configurations provide the best stability of the measurements, while ensuring the convergence of the fitting process even in the cases of the widest CCFs. Along with the measurements of the radial velocity we obtain the FWHM of the cross correlation function which we also use to track variations in the activity level of the star.

For the bisector span measurement we rely on the pipeline results, as it does not depend on the fit but on the CCF itself. The bisector has been since more than 10 years ago a standard activity diagnostic tool for solar type stars. Unfortunately its behaviour in slow rotating stars is not as informative as it is for fast rotators (Saar & Donahue 1997; Bonfils et al. 2007). The line distortion measured in the bisector span is proportional to the $v \cdot sin(i)$ of the stars. As most of the stars in our sample have a $v \cdot sin(i)$ smaller than 2-3 km s^{-1} the bisector gives no information for most of them.

Figure 4.2 shows the relation between the HARPS and HARPS-N mean radial velocities for the different stars with data in common. The slope is exactly 1.00. Figure 4.3 shows the measurement RMS of the radial velocities

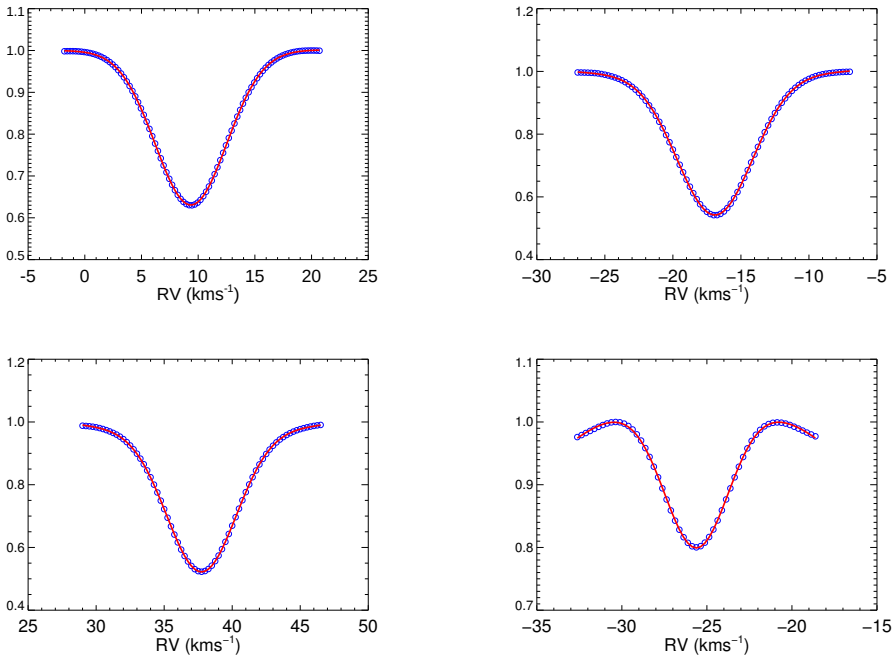

Figure 4.1: Cross correlation functions for the F-type stars HD 1581 (top-left panel), the G-type star HD 161098 (top-right panel), the K-type star HD 176986 (bottom-left panel) and the M-type star GJ 536 (bottom-right panel). The red line shows the best fit using the Gaussian function plus a second order polynomial.

for all the stars in the sample. Table 4.1 shows the measurements for the mean radial velocity, radial velocity RMS and typical measured error for the stars in our sample for which radial velocity measurements could be performed.

4.2 Searching for radial velocity variability

To search for periodic radial velocity signals in our spectroscopic time-series we follow a similar procedure as the one explained before. We search for periodic signals using a Generalised Lomb Scargle Periodogram Zechmeister & Kürster (2009) and if there is any significant periodicity we fit the detected signal. We sequentially find the dominant component in the time series and remove them, until there are no more significant signals.

Table 4.1: Relevant information for the stars of the sample. Full table in Appendix C.1

Star	Sp. Type	RMS(V_r) [ms^{-1}]	σ V$_r$* [ms^{-1}]
HD 1581	F9.5	2.70	0.79
HD 161098	G8	2.00	0.99
HD 176986	K2.5	3.90	0.92
GJ 536	M1	3.41	1.31
GJ 3998	M1	3.18	2.22

* Median error of the individual measurements.

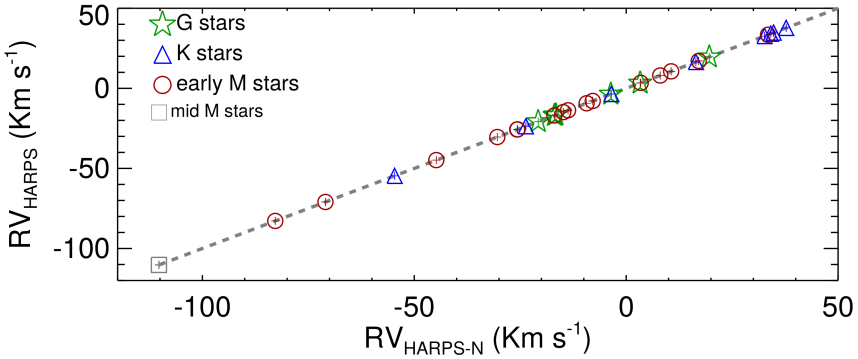

Figure 4.2: Mean RV measurements of HARPS and HARPS-N compared for the stars with data in common.

The significance of the periodogram peak is evaluated using the Cumming (2004) modification of the Horne & Baliunas (1986) formula to obtain the spectral density thresholds for a desired false alarm level. The false alarm probability is defined as $FAP = 1 - [1 - P(z > z_0)]^M$ where $P(z > z_0)$ is the probability of z, the target spectral density, being greater than z_0, the measured spectral density, and M the number of independent frequencies, approximated as $\Delta T/\delta t$, with the time span of periodogram going from 1.5 to 10 000 days and the number of frequency steps fixed at 10 000.

We have data from many different sources with very different observational cadences. For instance, in the case of HARPS and HARPS-N data for the brightest stars, we even have multiple exposures every day of observations. In these cases we rebin the data into daily measurements. The Nyquist frequency

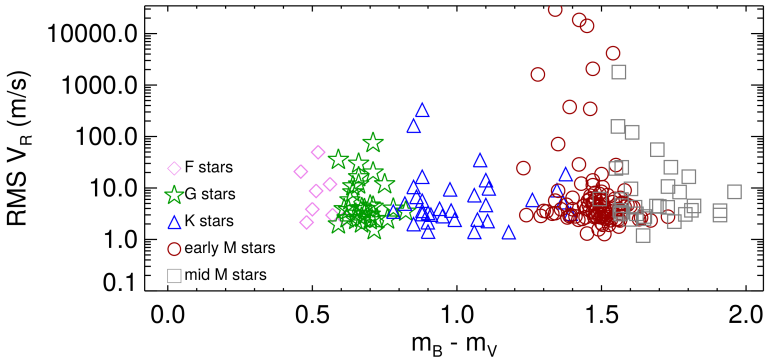

Figure 4.3: RV RMS for all the stars with HARPS or HARPS-N data.

of our data is hard to determine, as it varies from star to star and from dataset to dataset. However none of the datasets is well suited to measure very high frequency signals. We limit the search for variability to periods longer than 1.5 days. On the low frequency side we limit the search to 10 000 days, that is approximately 3 times longer than the longest time span of the HARPS N/S or ASAS observations. This allows us to measure incomplete signals, obviously involving large uncertainties, as in the previous chapter.

When finding a signal the first step is assessing its origin. For most of the stars we know the possible activity induced signals that we might have. In the previous chapter we measured magnetic cycles, rotation periods and possible situations of differential rotation.

Finding a radial velocity signal at the same period (or one of the harmonics) of and activity signal does not automatically eliminate the signal as a planet candidate. As a planet can orbit synchronized with the rotation of its parent star. But it automatically puts the signal in quarantine. Its amplitude, phase, the possible correlations with the activity data and the stability over time of the signal are taking into account in order to see the origin of the signal.

Activity signals are modelled by least squares minimization with the MPFIT routine (Markwardt 2009) using Eq. 4.1 as test model, as in the case of the signals in the activity proxies.

$$\begin{aligned} y(t) &= A_1 \cdot sin(2 \cdot \pi \cdot t/P + \phi_1) \\ &+ A_2 \cdot sin(2 \cdot \pi \cdot t/(0.5 \cdot P) + \phi_2) + C \end{aligned} \tag{4.1}$$

Planetary signals are modelled by Keplerian models using the RVLIN package (Wright & Howard 2012). Uncertainties are calculated using the BOOT-

TRAN package (Wang & Wright 2012). BOOTTRAN takes the best-fit parameters and radial velocity data and calculates the error bars from sampling distribution estimated via bootstrapping. It re-samples the original data to create multiple data replicates and derives again the orbital parameters in all of them. The ensemble of parameters obtained gives the approximate sampling distribution for each estimated parameter. The standard deviation of the distribution is the standard error for the estimate.

We searched for radial velocity variability in a sample of 133 stars with more than 30 radial velocity measurements available. The same as in section 3.2 we perform a pre-screening of all the targets using our home-made automatic tool, in this case to study the radial velocity signals. The capabilities of the program are weaker when analysing radial velocity data that it is when analysing activity indicators. It is able to identify significant periodic signals in the data, but nothing else. Even this way it is a very helpful tool to narrow down the sample.

In order to illustrate the method, we describe below in detail the cases of the same five stars analysed in section 3.2. Those are the five stars were new planetary companions have been finally detected (HD 1581, HD 161098, HD 176986, GJ 536 and GJ3998). In total we detect 6 robust planetary signals. In addition, we find one tentative planetary signal and a many cases of activity induced periodic radial velocity signals.

HD 1581

The radial velocity measurements of the F-type star HD 1581 show a rms of the radial velocities of 2.70 ms^{-1} with a typical uncertainty of the individual measurements of 0.79 ms^{-1}. An F-test gives a negligible probability of the measurement errors being the origin of the detected variability. We used 1728 spectra taken during 201 individual nights over 9.9 years. The error after the nightly binning gets reduced to a typical uncertainty of 0.30 ms^{-1}. The radial velocity time series show a long term modulation with a period longer than 16 years (Fig. 4.4) with a shape similar to the activity cycle seen in Fig. 3.14.

The data shows a clear correlation between the radial velocity variations and the variations in the FWHM of the CCF ($r = 0.69$). Implying that the main source of variation is the activity of the star. The long-term variation seen in Fig. 3.14 is probably the radial velocity signal induced by the long term magnetic cycle of the star.

De-trending the data with respect to the FWHM greatly reduces the amplitude of the radial velocity measurements to an RMS of 1.75 ms^{-1}. Analysing the de-trended data we find a 15.678 $\pm$ 0.001 days periodic signal with a semi-amplitude of 0.99 $\pm$ 0.03 ms^{-1} detected with a FAP better than the 0.1%

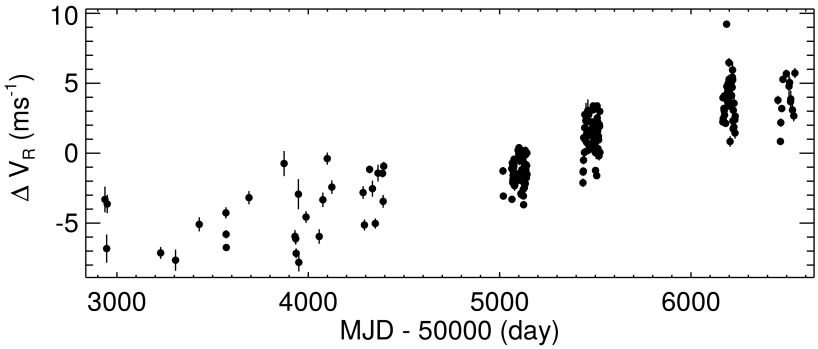

Figure 4.4: V_R time series for the star HD 1581

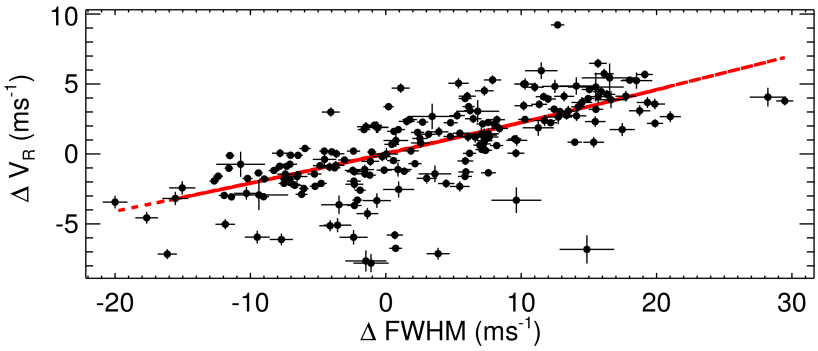

Figure 4.5: ΔV_R against ΔFWHM for the star HD 1581. The red line shows the best fit to the data.

(Fit. 4.6). This signal is probably the radial velocity induced signal of the stellar rotation, which has a measured period of 14.65 days from the previous chapter. Further support to this interpretation is the fact that before subtracting this signal there is a weak anti-correlation between the bisector span of the CCF (r = -0.11) that vanishes once the signal is subtracted. A second evidence would be the shape of the signal. Phased Keplerian signals usually have "cleaner" shapes. The shape of the best fit to the data for this signal is closer to what would be expected for a rotation induced signal according to SOAP (Dumusque et al. 2014).

The RV residuals after the subtraction of the rotation induced signal unveils another significant signal. This time is a 64.702 $\pm$ 0.033 days with a semi-amplitude of 0.93 $\pm$ 0.03 ms^{-1} detected with a FAP better than the 0.1%

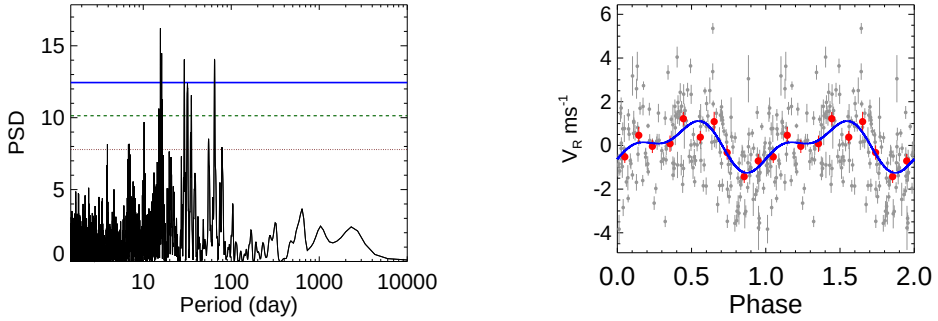

Figure 4.6: Periodogram of the de-trended V_r time series of the star HD 1581(left panel) and phased curve using the 15.68 days periodicity (right panel). For a detailed description see Fig. 3.16.

(Fit. 4.7). In this curve there is no clear correlation between the radial velocities and any activity proxy. The phased curve is very scattered, which is a typical scenario when dealing with sub-ms signals, specially after correcting from activity signals, as happens in Pepe et al. (2011). We interpret this signal as evidence for a planetary companion.

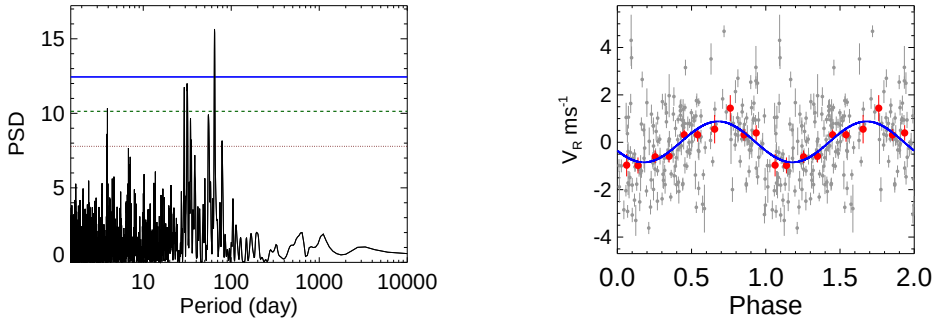

Figure 4.7: Periodogram of the residuals of the V_r time series of the star HD 1581(left panel) and phased curve using the 64.70 days periodicity (right panel). For a detailed description see Fig. 3.16.

No more significant signals are found in the data.

The F-type star HD 1581 exhibits three significant signals in its radial velocity time series. Two of intrinsic origin, one long term signal and one that matches the rotation of the star, and the last one of probable Keplerian origin. Table 4.2 shows the parameters of the planet candidate using a simultaneous

Table 4.2: Parameters for the new planet candidate orbiting HD 1581

Parameter	HD 1581 b	
P [d]	64.629 ± 0.152	
e	0.00 ± 0.20	(fixed)
K [ms^{-1}]	0.863 ± 0.176	
$M \cdot sin(i)$ [M$_\oplus$]	5.62 ± 1.08	
Semimajor axis [au]	0.322 ± 0.005	
RMS Res [ms^{-1}]	1.30	

fit of all signals, using a polynomial for the long term signal and two sinusoidals for the short term signals.

The planet candidate HD 1581 b would be a super-Earth with a minimum mass of 5.62 ± 1.08 M$_\oplus$ orbiting at 0.322 ± 0.005 au. A rough estimate of the equilibrium temperatures of the planets, from the Stefan–Boltzmann law assuming uniform equilibrium temperature over the entire planet and Earth albedo, gives an equilibrium temperature 508 K.

HD 161098

For the G-type star HD 161098 we have 127 HARPS and 137 HARPS-N spectra taken during 180 individual nights over 10.4 years. The radial velocities show a scatter of 2.00 ms^{-1} with a median error bar of 0.88 ms^{-1} (Fig. 4.8). An F-test returns a negligible probability of the RV variations being explained by the measurement errors.

HD 161098 shows a long term RV variation with a period of 1606 ± 20 days with a semi-amplitude of 1.46 ± 0.09 ms^{-1} detected with a FAP smaller than the 0.1% (Fig. 4.9). The radial velocity data shows a significant correlation with the FWHM data ($r = 0.40$), but this does not seem to imply that this signal is of stellar origin. The most significant peak in the FWHM periodogram is at 26.3 days, very similar to the rotation period that we measured in the previous chapter. Subtracting the correlation as a lineal or quadratic dependence between the two variables enhances the significance of the detection in radial velocity, suggesting the correlation with the activity indicators is probably unrelated with this signal or spurious. The length of the signal also does not coincide with the magnetic cycle measured in the previous chapter.

The residuals after the fit show a second signal at the 1% FAP threshold with a period of 70.60 ± 0.60 days and a semi amplitude of 0.87 ± 0.08

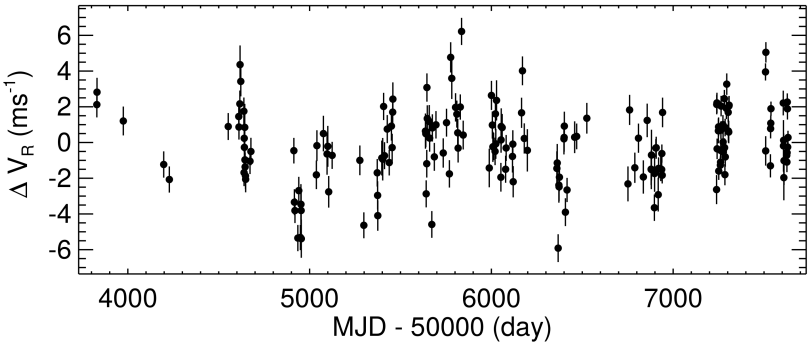

Figure 4.8: V_R time series for the star HD 161098.

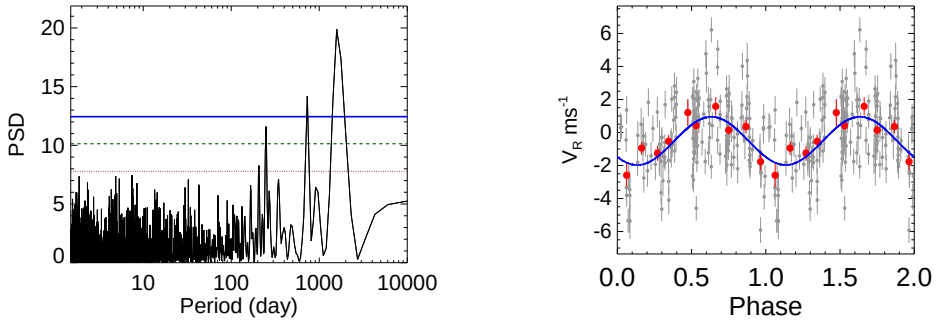

Figure 4.9: Periodogram of the V_r time series of the star HD 161098(left panel) and phased curve using the 1606 days periodicity (right panel). For a detailed description see Fig. 3.16.

ms^{-1}(Fig. 4.10). Nothing in the activity indicators, nor in the previous activity analysis suggests that this could be an activity induced signal. The signal is at the edge of the 1% FAP threshold, meaning is not a conclusive detection but a suggestion of a tentative planet candidate.

No more significant signals are found in the radial velocity data.

Table 4.3 shows the final parameters of the stated planet candidates with uncertainties calculated using the BOOTRAN routine (Wang & Wright 2012).

In summary, for the star HD 161098 we find two significant signals that do not seem to be of stellar origin. First a 1569 days signal with a semi-amplitude of 1.46 ms^{-1} that would correspond to a planet of 26.6 $M_\oplus$ orbiting at 2.50 au of its parent star. The second one is a 70 days signal with a semi amplitude of 0.87 ms^{-1} that, in the case of being confirmed with future observations, would

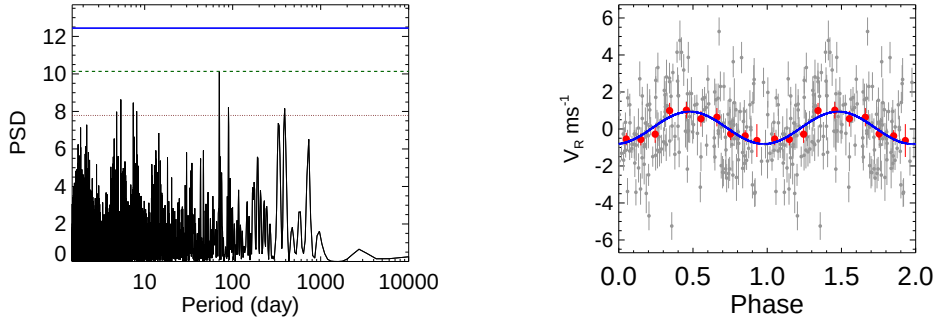

Figure 4.10: Periodogram of the residuals of the V_r time series of the star HD 161098 (left panel) and phased curve using the 70.60 days periodicity (right panel). For a detailed description see Fig. 3.16.

Table 4.3: Parameters for the new planet candidate orbiting HD 161098

Parameter	HD 161098 b	HD 161098 c
P [d]	1569.005 ± 53.043	70.601 ±0.179
e	0.24 ± 0.13	0.05 ± 0.30
K [ms^{-1}]	1.682 ± 0.233	0.915 ± 0.269
$M \cdot sin(i)$ [M$_\oplus$]	26.60 ± 4.39	5.30 ± 1.22
Semimajor axis [au]	2.503 ± 0.072	0.317 ± 0.006
RMS Res [ms^{-1}]	1.74	

correspond to a planet of 5.3 M$_\oplus$ orbiting at 0.32 au of its parent star. The estimates for the equilibrium temperatures of both planets would be 158 and 443 K respectively.

HD 176986

For the case of the K-type star HD 176986 we have 134 HARPS and 146 HARPS-N spectra taken during 190 individual nights over 12.1 years. The radial velocities show a scatter of 3.90 ms^{-1} with a median error bar of 0.92 ms^{-1} (Fig. 4.11). An F-test returns the probability of the variation being explained by the measurement errors much smaller than the 0.1%.

The analysis of the radial velocity data shows several significant signals in the periodograms at very different time-scales. One of them, although not the

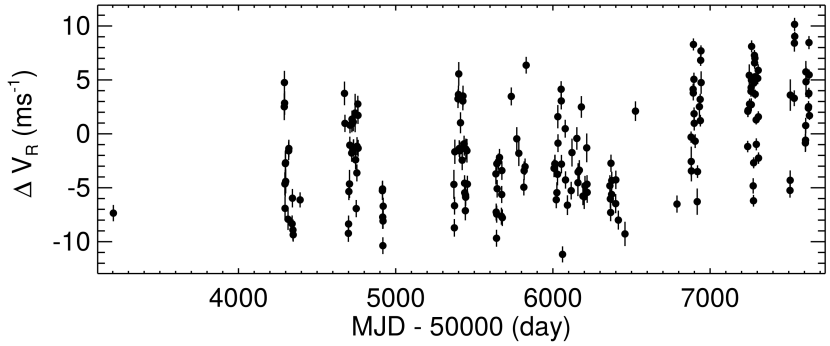

Figure 4.11: V_R time series for the star HD 176986

most significant, is a long term signal comparable with the magnetic cycle measured in the previous chapter. Long term signals are usually easier to subtract before short term signals, even if the amplitudes are smaller. Removing them usually cleans the periodograms and helps fitting the other signals. We fit a 2583 ± 33 days signal with a semi amplitude of 1.94 ± 0.13 ms^{-1}, detected with a FAP of 0.2% (Fig. 4.12). We use the double sinusoidal model, as the signal matches the magnetic cycle period.

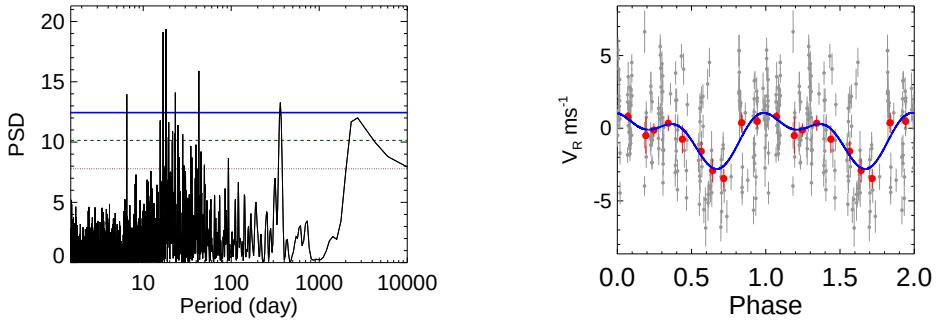

Figure 4.12: Periodogram of the V_r time series of the star HD 176986(left panel) and phased curve using the 7.07 years periodicity (right panel). For a detailed description see Fig. 3.16.

The subtraction of the 2600 days signal leaves once again with several significant signals. Being the most significant one a 16.827 ± 0.001 days signal with a semi amplitude of 2.75 ± 0.12 ms^{-1} detected with a FAP smaller than the 0.1% (Fig. 4.13). The period of this signal is very close to being half of the

measured rotation period. The fact that a good fit to the data requires two sinusoidals and the presence of many significant peaks around it that continue being significant after subtracting the main peak suggests a stellar origin for this signal.

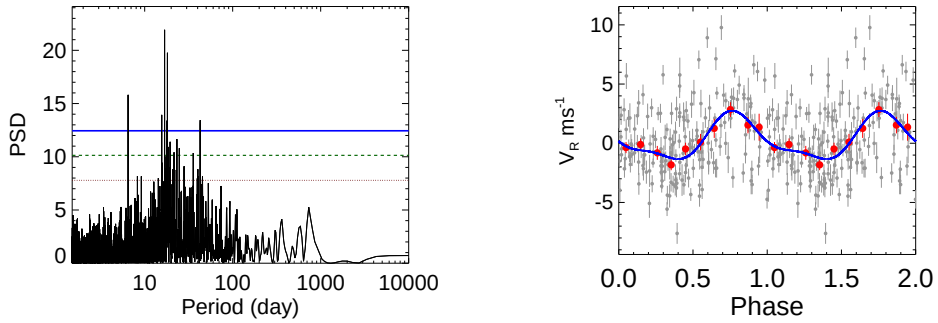

Figure 4.13: Periodogram of the residuals of the V_r time series of the star HD 176986 (left panel) and phased curve using the 16.9 days periodicity (right panel). For a detailed description see Fig. 3.16.

The residuals after fitting the harmonic of the stellar rotation continue showing several significant periodic signals. The most prominent peak in the periodogram corresponds to a 6.491 $\pm$ 0.001 days signal with a semi-amplitude of 2.25 $\pm$ 0.11 ms^{-1} detected with a FAP better than the 0.1% (Fig. 4.14). For this signal there is no corresponding signal in the activity analysis of the previous chapter and nothing in the activity proxies suggests a stellar origin. The shape of the phased plot is sinusoidal even when trying to fit it with the double-sinusoidal model. This signal is probably of Keplerian origin.

Another significant signal appears at 18.118 $\pm$ 0.002 days with a semi amplitude of 2.05 $\pm$ 0.11 ms^{-1} detected with a FAP better than the 0.1% (Fig. 4.15). This signal is very close in period to the 16.9 days signal detected before. The shape is also not completely sinusoidal, although it does not deviates as much as the previous one.

HD 176986 showed a somewhat complex activity behaviour, with several signals arising in the S_{MW} index and the H_α index, implying a strong case of activity signals induced at different latitudes. This could lead to several activity signals in the radial velocity time series, with periods very close to each other, instead of having one dominant signal at the rotation or its first harmonic. The origin of this signal at this point is hard to asses, but it is probably of stellar origin.

Then we find two new close signals. One at 40.878 $\pm$ 0.011 days signal with

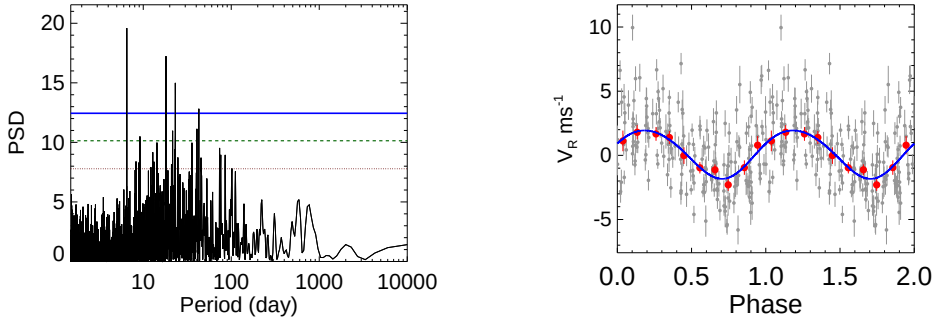

Figure 4.14: Periodogram of the residuals of the V_r time series of the star HD 176986 (left panel) and phased curve using the 6.49 days periodicity (right panel). For a detailed description see Fig. 3.16.

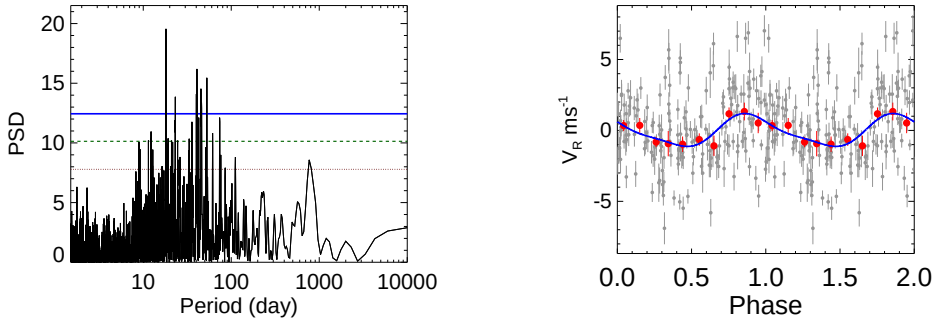

Figure 4.15: Periodogram of the residuals of the V_r time series of the star HD 176986 (left panel) and phased curve using the 18.1 days periodicity (right panel). For a detailed description see Fig. 3.16.

a semi-amplitude of 1.34 ± 0.11 ms^{-1} (Fig. 4.16) and the other one at 42.669 ± 0.017 days with a semi-amplitude of 1.00 ± 0.11 ms^{-1} (Fig. 4.17), both detected with FAPs better than the 0.1%. Both signals show very scattered phase folded fits with a very similar shape. The signals are not aliases of each other and are probably not planetary signals. The relation to the detected activity signals suggests that this might the mark of surface features at polar latitudes.

No more significant signals are detected in the radial velocity data.

Once all the significant signals have been detected we go the other way around and proceed to clean the time series from all the activity signals in order to isolate the planetary signal. Fig 4.18 shows the periodogram and the fit of the planetary signal. The significance of the detection in this case

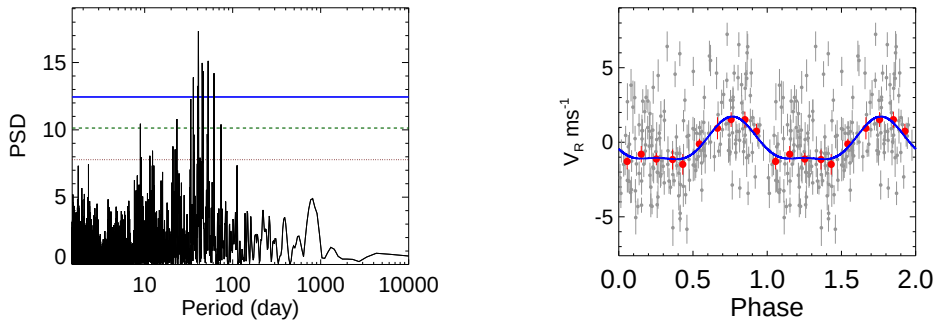

Figure 4.16: Periodogram of the residuals of the V_r time series of the star HD 176986 (left panel) and phased curve using the 40.9 days periodicity (right panel). For a detailed description see Fig. 3.16.

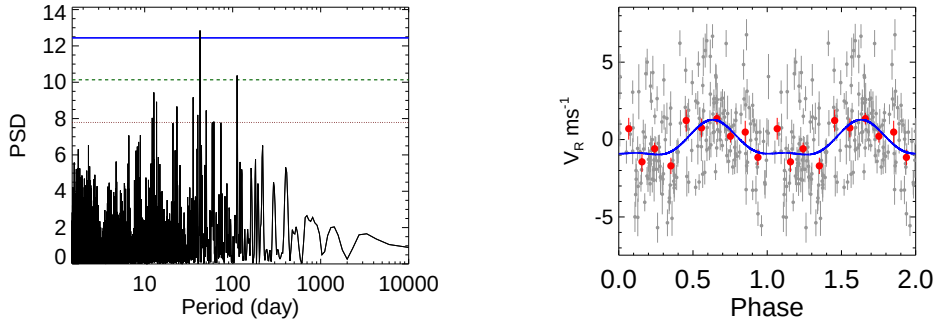

Figure 4.17: Periodogram of the residuals of the V_r time series of the star HD 176986 (left panel) and phased curve using the 42.7 days periodicity (right panel). For a detailed description see Fig. 3.16.

increases, and the amplitude of the signal gets slightly smaller.

HD 176986 is a moderately quiet K-type stars that exhibits a very complex activity pattern in its radial velocity. We detect 5 signals for which the origin is probably intrinsic to the star. One of them is related to a magnetic cycle, two at the first harmonic of its rotation and two more which could be due to rotation at polar latitudes. Hidden among them we find a planet of 4.86 $M_\oplus$ orbiting at 0.06 au of its parent star, with an estimated equilibrium temperature of 923 K. Table 4.4 shows the parameters of HD 176986 b.

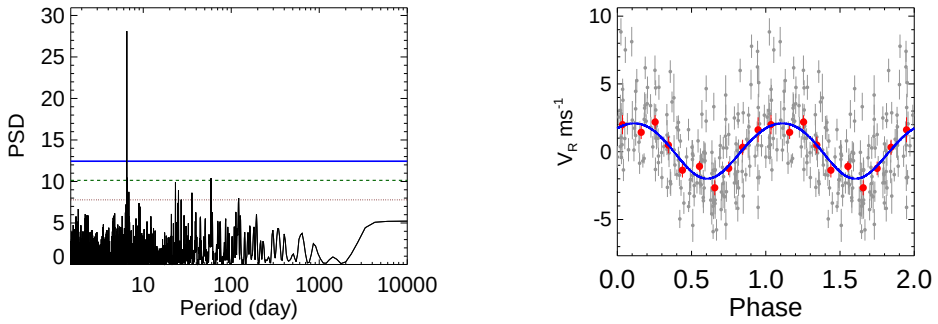

Figure 4.18: Periodogram of the cleaned V_r time series of the star HD 176986 (left panel) and phased curve using the 6.49 days periodicity (right panel). For a detailed description see Fig. 3.16.

Table 4.4: Parameters for the planet candidate orbiting HD 176986

Parameter	HD 176986 b
P [d]	6.493 ± 0.001
e	0.00 ± 0.12
K [ms^{-1}]	2.056 ± 0.260
$M \cdot sin(i)$ [M$_\oplus$]	4.86 ± 0.66
Semimajor axis [au]	0.061 ± 0.001
RMS Res [ms^{-1}]	2.45

GJ 536

For the early M-type star GJ 536 we have 141 HARPS and 12 HARPS-N spectra taken during 145 individual nights over 11.9 years. The radial velocities show a disperssion of 3.43 ms^{-1} with a median error bar of 1.33 ms^{-1} (Fig. 4.19). An F-test returns a probability of the variation being explained by the measurement errors much smaller than the 0.1%.

The most significant signal is a 8.709 ± 0.001 days signal with a semi amplitude of 3.02 ± 0.21 ms^{-1} detected with a FAP smaller than the 0.1% (Fig. 4.20). This signal is far from the rotation period measured for this star, or its first or second harmonics. Nothing in the activity proxies indicate that it might be of stellar origin. It is probably a planetary companion.

Subtracting the first signals shows a 43.814 ± 0.017 days signal with a semi amplitude of 2.39 ± 0.22 ms^{-1} detected also with a FAP better than the 0.1%

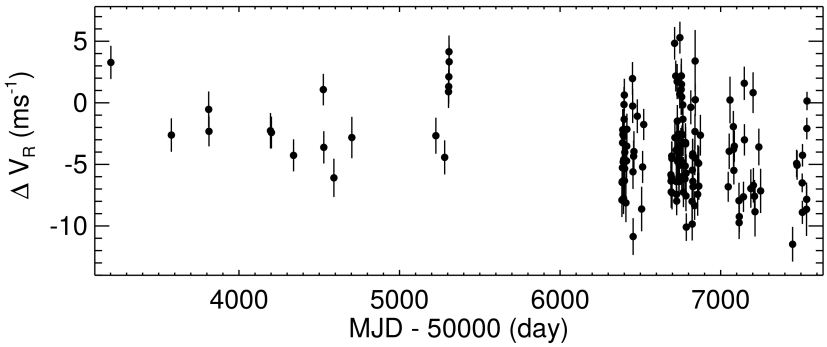

Figure 4.19: V_R time series for the star GJ 536

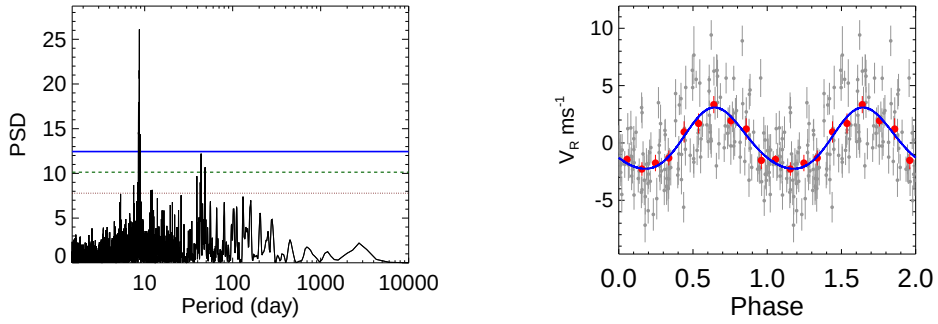

Figure 4.20: Periodogram of the V_r time series of the star GJ 536(left panel) and phased curve using the 8.71 days periodicity (right panel). For a detailed description see Fig. 3.16.

(Fig. 4.21). The period of this signal perfectly matches the rotation period of the star, and isolating it shows a strong correlation between the radial velocities and all the activity proxies.

No more significant signals are found in the radial velocity time series.

Going the other way around, i.e. subtracting the rotational signal beforehand leaves a extremely clean periodogram with a single isolated signal (Fig. 4.22). The 8.7 days signal appears as significant as before and the fit gets less scattered, with a slightly reduced amplitude.

GJ 536 is a moderately quiet star with two significant signals in its radial velocity data. One at 44 days corresponding to the rotation of the star, with a semi amplitude of 2.39 ms^{-1}. The other, with a semi amplitude of 2.7 ms^{-1} and a period of 8.7 days, corresponds to a planet of 5.47 $M_\oplus$ orbiting at 0.07 au

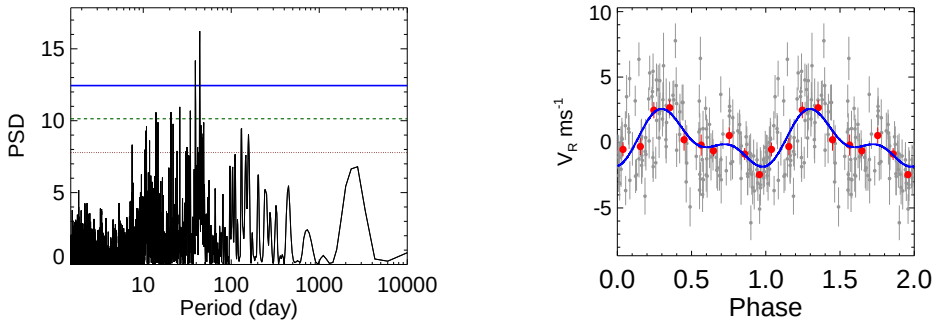

Figure 4.21: Periodogram of the residuals of the V_r time series of the star GJ 536(left panel) and phased curve using the 43.8 days periodicity (right panel). For a detailed description see Fig. 3.16.

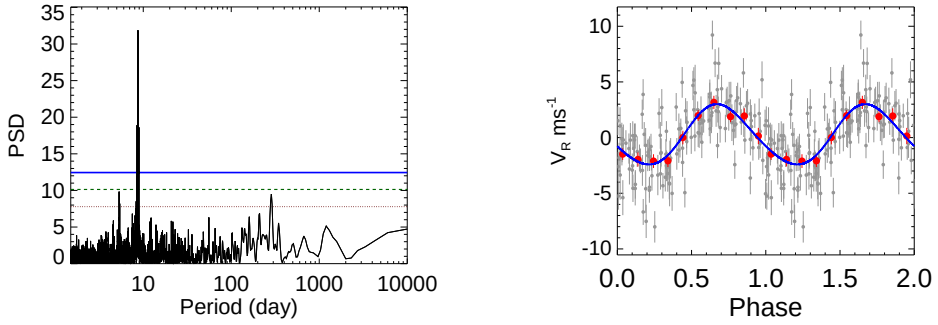

Figure 4.22: Periodogram of the cleaned V_r time series of the star GJ 536(left panel) and phased curve using the 8.71 days periodicity (right panel). For a detailed description see Fig. 3.16.

of its parent star with an estimated equilibrium temperature of 672 K. Table 4.5 shows the parameters of the planet.

GJ 3998

The radial velocity measurements of the M-type star GJ 3998 show rms of the measurements of 3.18 ms^{-1} with a median uncertainty of 2.22 ms^{-1}. It comes from 6 HARPS and 129 HARPS-N spectra taken during 129 individual nights over 7.5 years, with most of the observations taking place in the last three years (Fig. 4.23). An F-test returns a negligible probability of the variability being explained by the measurement uncertainties. This star has two small planet

Table 4.5: Parameters for the planet candidate orbiting GJ 536

Parameter	GJ 536 b
P [d]	8.709 ± 0.002
e	0.07 ± 0.09
K [ms^{-1}]	2.708 ± 0.256
$M \cdot sin(i)$ [$M_\oplus$]	5.47 ± 0.84
Semimajor axis [au]	0.066 ± 0.002
RMS Res [ms^{-1}]	2.07

(Affer et al. 2016) published in the framework of the HADES RV program (sec. 2.1.1). The following analysis was performed independently at the same time and confirmed the published planets.

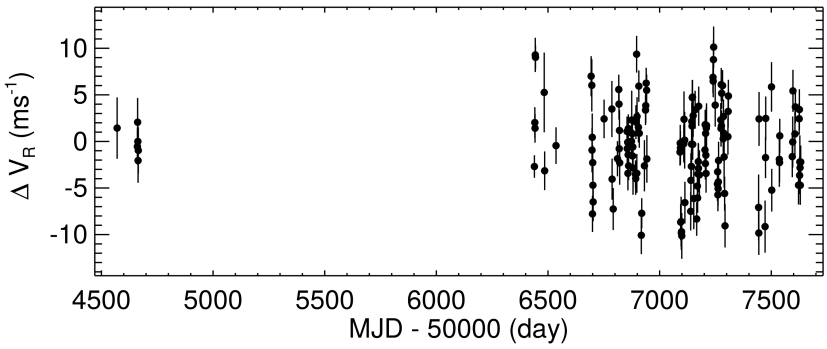

Figure 4.23: V_R time series for the star GJ 3998

The analysis of the radial velocities shows the presence of several significant signals, being the most prominent of them a 30.778 ± 0.019 days signal with a semi-amplitude of 3.30 ± 0.32 ms^{-1} detected with a FAP smaller than the 0.1% (Fig. 4.24). This signal almost perfectly matches the rotation period measured in the previous chapter, suggesting its probable stellar origin. The data also shows a weak correlation between the radial velocity and the S_{MW} index that vanishes once the 30.8 days signal is subtracted, supporting the idea that it is a rotation induced signal.

The next significant signal is a 13.737 ± 0.005 days signal with a semi-amplitude of 2.56 ± 0.22 ms^{-1} detected with a FAP smaller than the 0.1%

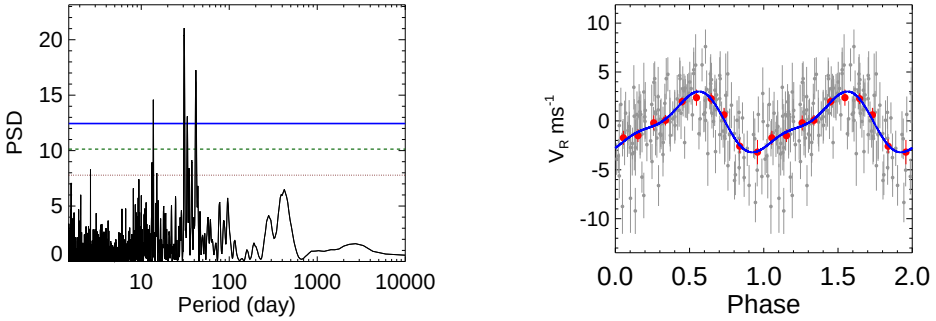

Figure 4.24: Periodogram of the V_r time series of the star GJ 3998 (left panel) and phased curve using the 30.8 days periodicity (right panel). For a detailed description see Fig. 3.16.

(Fig. 4.25). This signal is attributed to a planetary companion in Affer et al. (2016). We agree on that interpretation as we do not find any similar signal in the activity indicators or any significant correlation with any of the stellar activity proxies.

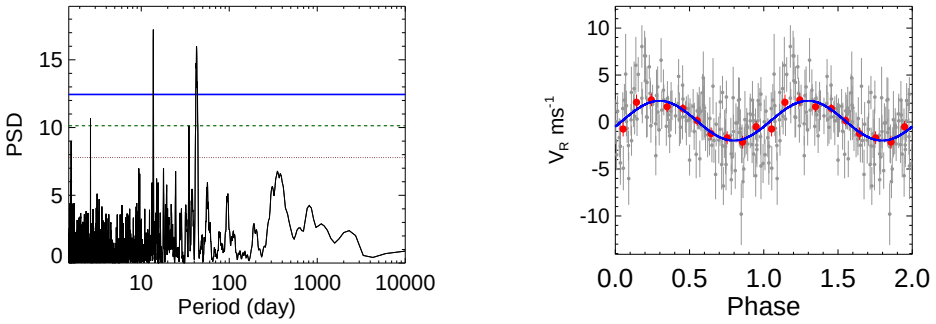

Figure 4.25: Periodogram of the residuals of the V_r time series of the star GJ 3998 (left panel) and phased curve using the 13.8 days periodicity (right panel). For a detailed description see Fig. 3.16.

Subtracting the planetary signal we find a broad feature in the periodogram that corresponds to a signal of a period of 298.2 ± 1.6 days with a semi-amplitude of 2.05 ± 0.35 ms^{-1} detected with a FAP smaller than the 0.1%. The irregular shape of the peak in the periodogram rises concerns on a poorly sampled signal, or a detection distorted by the spectral window function. The peak is very similar in shape to one of the strongest features of the window

function. It is also worth noting that ∼300 days is the 2 years alias of a ∼500 days signal, which is the period of the magnetic cycle measured in the S_{MW} index time series. De-trending the data with respect to the S_{MW} index severely weakens this signal, supporting the idea that the long term magnetic cycle and this ∼300 days signals are linked.

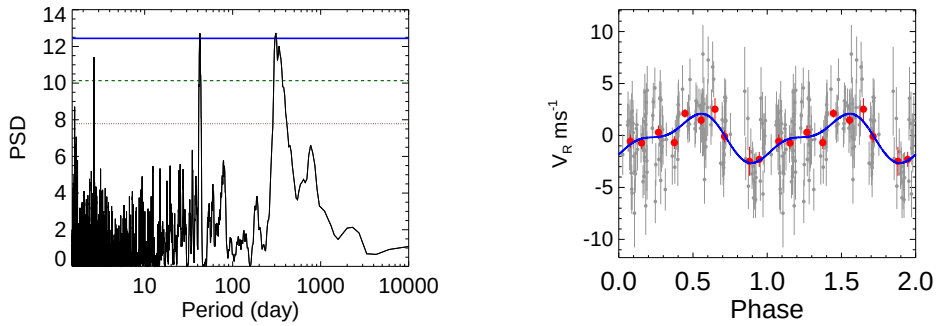

Figure 4.26: Periodogram of the residuals of the V_r time series of the star GJ 3998 (left panel) and phased curve using the 298.2 days periodicity (right panel). For a detailed description see Fig. 3.16.

The following significant periodicity is a 42.154 ± 0.060 days signal with a semi amplitude of 1.61 ± 0.32 ms^{-1} detected with a FAP better than the 0.1% (Fig. 4.27). The origin of this signal is somewhat troublesome. Affer et al. (2016) interpreted it as a sign of differential rotation but, while the time-scale is perfectly reasonable for a differential rotation effect, we do not find any significant periodicity in the activity indicators that could support that interpretation. On the other hand one there is a significant feature in the window function at ∼ 120 days (1/3 of a year). The signal at 42 days is very close to the 120 days alias of ∼ 31 days ($1/42 + 1/120 = 1/31$), suggesting it could be an alias of the rotational signal. That would also explain why the signal lost strength after subtracting the ∼31 days signal.

Subtracting the signal we are left with a 2.651 ± 0.001 days signal with an amplitude of 1.51 ± 0.32 ms^{-1} detected with a FAP smaller than the 0.1% (Fig. 4.28). We interpret this as a signal induced by a planetary companion, as nothing in the data suggests otherwise.

No more significant signals are found in the data.

The step by step analysis of the radial velocity data unveiled the presence of 5 periodic signals, 2 of them are attributed to planetary companions. As in the previous cases we proceed with the analysis by first subtracting all the non-planetary signals. We see then two clear signals in the periodogram, or

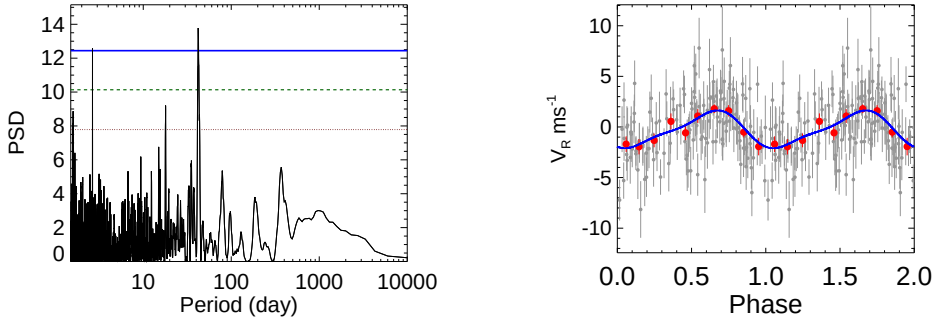

Figure 4.27: Periodogram of the residuals of the V_r time series of the star GJ 3998 (left panel) and phased curve using the 42.2 days periodicity (right panel). For a detailed description see Fig. 3.16.

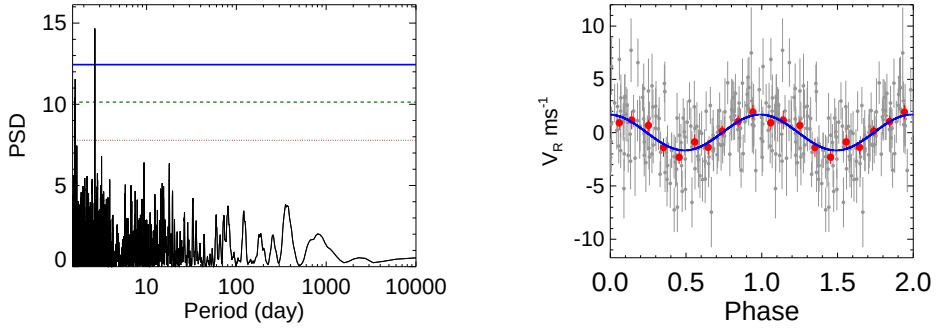

Figure 4.28: Periodogram of the residuals of the V_r time series of the star GJ 3998 (left panel) and phased curve using the 2.65 days periodicity (right panel). For a detailed description see Fig. 3.16.

13.7 and 2.65 days, for the two signals previously identified as planetary signals. No more significant signals appear in the periodogram. Table 4.6 shows the parameters of a simultaneous fit of the two planets after cleaning the data from activity signals.

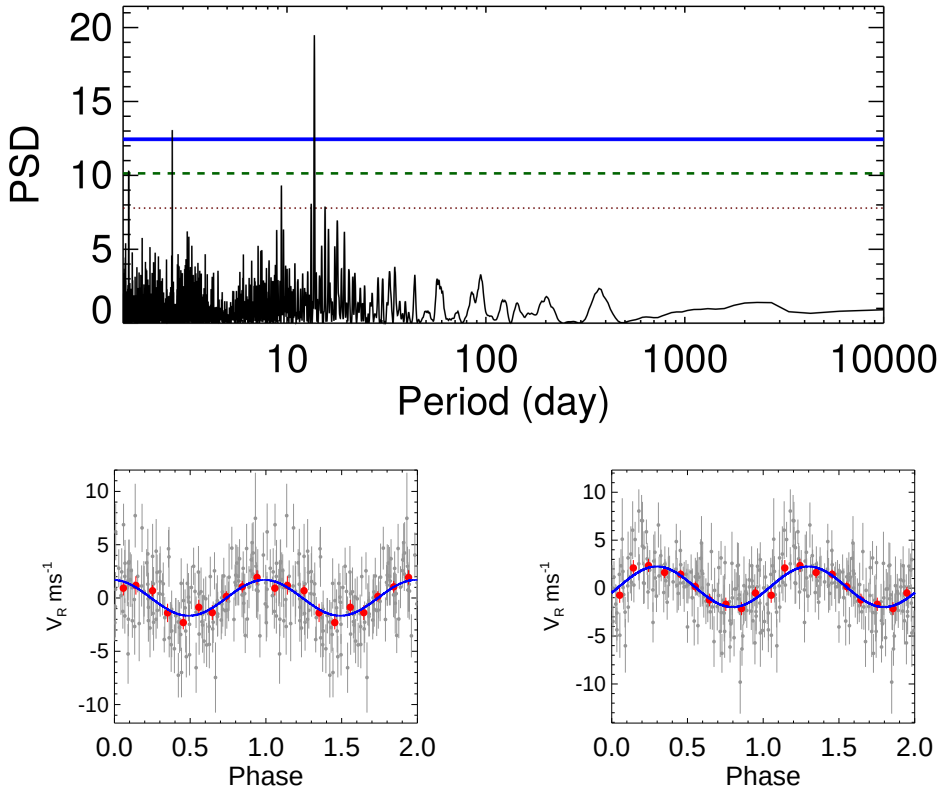

Figure 4.29: Periodogram of the cleaned V_r time series of the star GJ 3998 (top panel) and phased curve using the 2.65 days periodicity (bottom left panel) and phased curve using the 13.8 days periodicity (bottom right panel). For a detailed description see Fig. 3.16.

Table 4.6: Parameters for the planet candidates orbiting GJ 3998

Parameter	GJ 3998 b	GJ 3998 c
P [d]	2.650 ± 0.001	13.725 ± 0.011
e	0[1]	0.03 ± 0.11
K [ms^{-1}]	1.727 ± 0.323	2.597 ± 0.332
$M \cdot sin(i)$ [$M_\oplus$]	2.35 ± 0.42	6.12 ± 1.11
Semimajor axis [au]	0.029 ± 0.001	0.089 ± 0.003
RMS Res [ms^{-1}]	2.63	

[1] Fixed

Summarizing, GJ 3998 is an M-dwarf of average activity for which we find two planetary companions of masses of 2.35 $M_\oplus$ and 6.12 $M_\oplus$ orbiting at 0.029 and 0.089 au respectively, with equilibrium temperatures of 1004 K and 573 K respectively.

4.3 Activity Induced Signals

The previous analysis of radial velocity signals was carried out systematically for the 133 stars in the sample which had an adequate number of RV measurements. This lead to a set of 41 stars where we found the radial velocity induced signal by the stellar rotation and/or one of its harmonics. Tab 4.7 show these results. The distribution of radial velocity induced signals peaks at 1-2 ms^{-1}.

Table 4.7: Rotation induced radial velocity signals and their semi amplitudes. Stars are grouped by spectral type.

Name	$\log_{10}(R'_{\rm HK})$	P_{Rot} [d]	P_{RV} [d]	K_{RV} $[ms^{-1}]$
HD 1581	–4.84 ± 0.01	13.7 ± 0.1	15.7 ± 0.1	0.99 ± 0.23
HD 134060	–4.91 ± 0.01	23.7 ± 1.2	18.3 ± 0.1	0.91 ± 0.07
HD 1388	–4.89 ± 0.01	22.9 ± 0.1	21.7 ± 0.1	1.08 ± 0.12
HD 30495	–4.50 ± 0.03	11.8 ± 3.0	10.5 ± 0.1	7.05 ± 0.16
HD 2071	–4.83 ± 0.02	23.5 ± 4.7	24.3 ± 0.1	1.92 ± 0.16*
HD 41248	–4.80 ± 0.03	23.8 ± 4.7	25.6 ± 0.1	2.43 ± 0.13
HD 1461	–4.95 ± 0.02	31.7 ± 0.1	32.9 ± 0.1	0.67 ± 0.06
HD 59468	–4.95 ± 0.02	23.1 ± 3.5	24.9 ± 0.1	0.51 ± 0.09
HD 63765	–4.77 ± 0.05	27.0 ± 3.0	25.3 ± 0.1	3.34 ± 0.18*
HD 220256	–5.00 ± 0.04	44.7 ± 4.8	43.1 ± 0.1	1.05 ± 0.19*
CoRoT-7	–4.62 ± 0.07	22.5 ± 0.7	22.9 ± 0.1	6.67 ± 0.25
HD 128621	–4.93 ± 0.04	34.7 ± 3.9	31.2 ± 0.7	1.81 ± 0.10
HD 224789	–4.43 ± 0.02	16.8 ± 0.3	16.9 ± 0.1	16.40 ± 0.24*
HD 40307	–5.05 ± 0.05	26.2 ± 10.3	35.0 ± 0.1	0.50 ±0.06
HD 176986	–4.83 ± 0.03	31.5 ± 3.5	40.9 ± 0.1	1.34 ±0.11
HD 170493	–4.88 ± 0.06	40.6 ± 0.1	43.9 ± 0.1	1.42 ± 0.15[1]
HD 215152	–4.94 ± 0.05	36.5 ± 1.7	41.1 ± 0.1	0.51 ± 0.07*
HD 125595	–4.77 ± 0.03	38.7 ± 1.0	36.7 ± 0.1	2.11 ± 0.19

Continued on next page

Table 4.7 – *Continued from previous page*

HD 209100	–4.78 ± 0.03	27.0 ± 6.4	24.9 ± 0.1	1.41 ± 0.11
HD 85512	–4.95 ± 0.04	45.8 ± 5.2	46.1 ± 0.2	0.30 ± 0.05
GJ 229	–4.91 ± 0.04	26.7 ± 2.4	29.4 ± 0.1	1.29 ± 0.14
GJ 846	–4.81 ± 0.03	26.3 ± 5.6	22.3 ± 0.1	3.42 ± 0.33
GJ 3942	–4.46 ± 0.03	16.3 ± 0.2	16.3 ± 0.1	4.54 ± 0.28
GJ 676 A	–4.96 ± 0.03	35.0 ± 11.8	35.4 ± 0.1	2.37 ± 0.28*
GJ 740	–4.87 ± 0.04	36.8 ± 2.3	35.02 ± 0.1	3.15 ± 0.16
GJ 21	–4.73 ± 0.03	17.4 ± 0.1	16.8 ± 0.1	2.56 ± 0.32**
GJ 9689	–4.86 ± 0.04	39.6 ± 3.2	43.1 ± 0.2	3.54 ± 0.45
GJ 514	–5.11 ± 0.04	20.0 ± 0.9	30.8 ± 0.1	2.06 ± 0.16
GJ 536	–4.99 ± 0.04	43.9 ± 1.08	43.8 ± 0.1	1.62 ± 0.33
GJ 205	–4.75 ± 0.03	34.8 ± 1.3	32.6 ± 0.1	5.97 ± 0.20
GJ 667 C	–5.61 ± 0.07	103.9 ± 1.3	91.3 ± 0.2	1.42 ± 0.17
GJ 1	–5.53 ± 0.07	56.8 ± 5.6	59.0 ± 0.2	1.67 ± 0.28**
GJ 880	–4.92 ± 0.04	37.2 ± 6.7	36.4 ± 0.1	2.93 ± 0.19
GJ 382	–4.82 ± 0.04	21.8 ± 0.1	19.3 ± 0.1	5.69 ± 0.38 *
GJ 2	–4.84 ± 0.04	21.5 ± 1.5	22.4 ± 0.1	2.43 ± 0.19
GJ 47	–4.92 ± 0.06	34.4 ± 0.1	34.2 ± 0.1	2.33 ± 0.29
GJ 832	–5.23 ± 0.06	39.2 ± 9.4	39.1 ± 0.1	1.59 ± 0.22*
GJ 176	–5.00 ± 0.05	39.4 ± 1.0	39.2 ± 0.1	4.01 ± 0.27
GJ 162	–4.95 ± 0.05	34.3 ± 1.7	29.4 ± 0.1	3.51 ± 0.31
GJ 358	–4.64 ± 0.05	25.2 ± 0.1	26.3 ± 0.1	8.64 ± 0.42*
GJ 479	–4.85 ± 0.05	26.0 ± 7.2	23.1 ± 0.1	4.24 ± 0.30
GJ 674	–5.04 ± 0.07	33.0 ± 0.7	36.2 ± 0.1	2.87 ± 0.15
GJ 388	–4.25 ± 0.12	2.4 ± 0.1	2.3 ± 0.1	33.16 ± 3.32
GJ 273	–5.44 ± 0.05	93.5 ± 16.0	77.3 ± 0.1	1.30 ± 0.13
GJ 526	–5.06 ± 0.05	52.1 ± 12.0	49.2 ± 0.1	3.81 ± 0.38*
GJ 876	–5.30 ± 0.05	90.9 ± 16.5	106.2 ± 0.2	1.99 ± 0.12

* Signals detected with FAPs bigger than 0.1% but smaller than 1%

** Signals detected with FAPs smaller than 10%

When analysing the data we found that there is a clear relationship between the activity level of the star and the amplitude of the rotation induced signal. Figure 4.30 shows a linear relationship between the activity level of the star and the logarithm of the amplitude of its induced signal. This relationship is different for M-dwarfs than for FGK stars. We added three extra points from the literature (see table 4.8) in order to populate a bit more the plot and to increase the activity coverage. FGK and M-type stars are fit independently

Table 4.8: Rotation induced radial velocity signals from the literature

Name	$\log_{10}(R'_{\rm HK})$	P_{Rot} [d]	P_{RV} [d]	K_{RV} $[ms^{-1}]$
HD166435	–4.26	3.80	3.80	83.0
Sun	–4.91	26.1		2.3
GJ 15 A	–5.27 ± 0.05	46.5 ± 6.5	44.8	1.8

References: Queloz et al. (2001), Haywood et al. (2012), Howard et al. (2014)

Table 4.9: Parameters for equation 4.2

Dataset	a	b
GK-type Stars	2.59 ± 0.03	12.68 ± 0.13
M-type Stars	0.89 ± 0.03	4.85 ± 0.13

using the following equation:

$$\log_{10}(K_{V_r}) = a \cdot \log_{10}(R'_{\rm HK}) + b \tag{4.2}$$

Table 4.9 shows the parameters for the different fits for the two groups of stars.

Even in the case of slow rotators the radial velocity induced signals have amplitudes larger than those typically expected for terrestrial planets. In the case of FGK stars these activity induced signals can drop below the 1 ms^{-1} threshold for stars more quiet than the Sun, reaching sometimes the HARPS precision measurement limit. For M-dwarfs even in the case of very slow rotators these signals are larger than 1 ms^{-1}. There are no detected signals below this limit.

A selection criteria is not enough to avoid radial velocity induced signals. Even in the case of the most quiet stars this signal is still bigger than those of terrestrial planets. Modelling and removing the activity induced radial velocity signals becomes mandatory.

Figure 4.31 shows the strong correlation found between the semi amplitude of the Ca II H&K index modulation and the radial velocity induced signal. The stars in this case are split in two populations. One for the late F to early K stars and another from mid K stars to mid M dwarfs. In both situations the relationship is clear. The sudden split hints a different origin to the radial

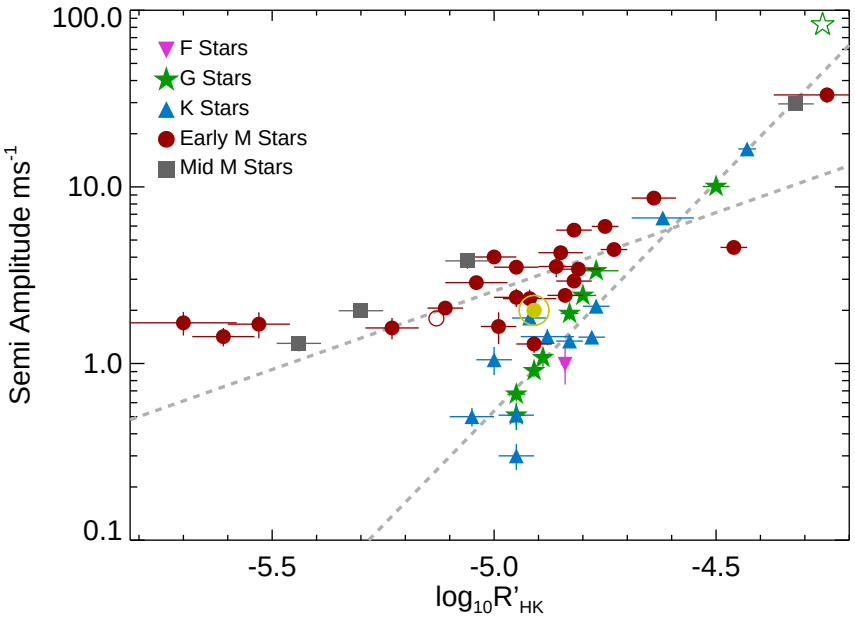

Figure 4.30: Semi-amplitude of the rotation induced signal versus chromospheric activity level $\log_{10}(R'_{\rm HK})$. Filled symbols correspond to our data, empty symbols to literature data.

velocity variations. A bigger sample is needed in order to investigate the origin of this split.

Additionally we studied the relationship between the amplitude of the radial velocity signals and the amplitude of their counterpart activity signals. We found that the amplitude in radial velocity correlates with the amplitude in the S_{MW} index. Figure 4.31 shows how the semi amplitude of the radial velocity signals compare with the semi amplitude of the S_{MW} index signals. Even with our limited sample two distinct populations seem apparent. The jump happens at spectral type K2.5, which would correspond to an effective temperature of 4800K. This is the surface temperature when the relative abundance of Ca II drops dramatically until being marginal at ∼4000K. FG and early M in one side, and late-K and M-type stars on the other are fit independently using the following equation:

$$K_{V_r} = a \cdot K_{S_{MW}} + b \tag{4.3}$$

Table 4.10: Parameters for equation 4.3

Dataset	a	b
FG and early K-type stars	0.72 ± 0.02	2.36 ± 0.04
Late K and M-type stars	0.89 ± 0.02	1.41 ± 0.02

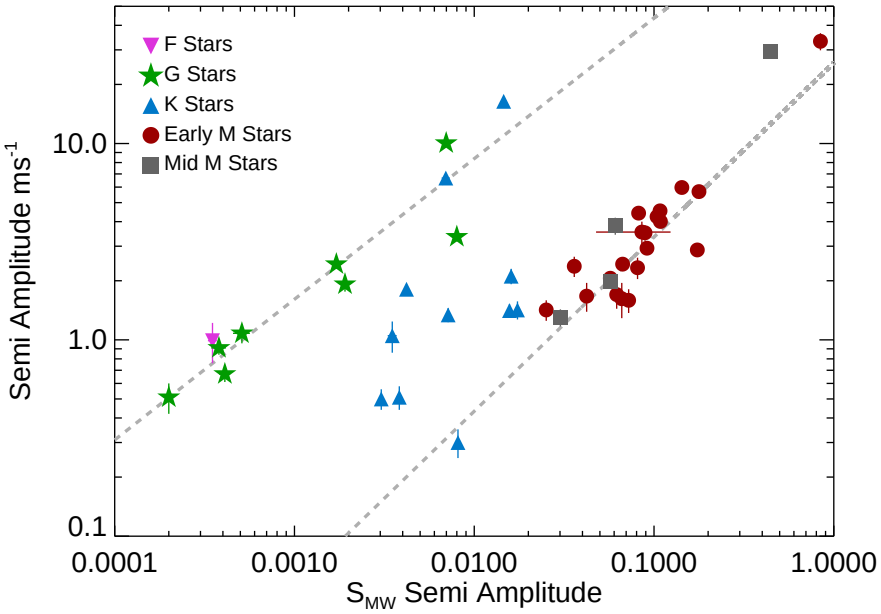

Figure 4.31: Semi-amplitude of the rotation induced signal versus the semi-amplitude of the rotation signal in the S_{MW} index. There are two distinct populations: one for stars with spectral types earlier than K1 stars, and another one for stars with spectral types later than K 4 stars. Stars with spectral types between K 1.5 and K 3.5 do not seem to align in any of those groups.

Finally we studied the phase difference between the induced radial velocity signals and the signals in the activity indicators. Bonfils et al. (2007) and Santos et al. (2014) found that the rotation induced radial velocity signal is not necessary in phase with the equivalent signal in the activity indicators. We measured the phase difference for all the signals in our results, finding

that indeed the signals are not necessary in phase. The phase difference of the signals in our sample cover the whole spectrum, and do not show a clear behaviour or correlation with any other studied parameter.

4.3.1 Harmonics of the Rotation Period

When measuring rotation induced signals it is expected to find also modulation with periods around the first harmonics of the rotation period. The relative strength of every of the present signals depends on the surface configuration and the inclination of the rotation axis related to our line of sight. For some particular configurations the signals at the harmonics of the rotation are dominant (Boisse et al. 2011). The previous radial velocity analysis provided us with some periodic signals compatible with the first harmonics of the rotation period. There is no reason why a planet cannot orbit synchronized with the first harmonic of the rotation of the star, so in order to consider a signal at one of these harmonics an activity induced signal we required the presence of an equivalent signal in any of the available activity indicators or a strong correlation between the radial velocity signal and at least one activity indicator.

We found signals compatible with activity induced signals at the harmonics of the rotation period in 15 of the 133 stars of the sample, 12 of them with FAPs smaller than the 1%. Table 4.11 shows the periods and amplitudes of the detected signals. Only one of the detections corresponds to a star not included in Table 4.7. The star GJ 581 shows a radial velocity induced signal at half the rotation period but not at the rotation – which is clear in the analysis of the activity indicators. Of the 9 stars where we detect a signal both at the rotation period and at one of its harmonics only two of them shows the signal larger for the harmonic. The star HD1461 shows a RV signal of 0.49 ms^{-1} at the rotation period and a 0.72 ms^{-1} signal at the harmonic, and the star GJ 2 show a RV signal of 2.43 ms^{-1} at the rotation period and a 2.81 ms^{-1} the signal at the harmonic. In the 13 remaining stars the RV signal is always smaller at the harmonic.

4.3.2 Implications for planet-hosting candidates

Previous studies of rotational modulation have questioned the existence of some planets through the use of periodograms of time-series measurements of activity indicators (e.g. Robertson et al. 2014). We have examined the orbital periods of exoplanet claims for our sample of stars in the light of the rotational periods that we have measured and found periodic signals in the activity time-series of several stars that are very similar to the orbital periods of planet candidates

Table 4.11: Radial velocity induced signals and their semi amplitudes for the activity induced signals at the harmonics of the stellar rotation

Name	Harm.	P_{RV} [d]	K_{RV} $[ms^{-1}]$	FAP [%]
HD 134060	$P_{Rot}/2$	10.4 ± 0.1	0.78 ± 0.08	< 0.1
HD 41248	$P_{Rot}/2$	13.4 ± 0.1	1.76 ± 0.14	< 0.1
HD 1461	$P_{Rot}/2$	15.0 ± 0.1	0.72 ± 0.02	< 0.1
Corot-7	$P_{Rot}/3$	7.5 ± 0.1	4.28 ± 0.24	< 0.1
HD 128621	$P_{Rot}/2$	17.9 ± 0.1	1.81 ± 0.08	< 0.1
GJ 740	$P_{Rot}/2$	18.0 ± 0.1	2.54 ± 0.17	< 0.1
GJ 720 A	$P_{Rot}/2$	9.3 ± 0.1	4.59 ± 0.32	< 0.1
GJ 21	$P_{Rot}/2$	9.4 ± 0.1	4.42 ± 0.32	< 0.1
GJ 9689	$P_{Rot}/2$	18.3 ± 0.1	2.78 ± 0.49	< 10
GJ 880	$P_{Rot}/2$	18.8 ± 0.1	1.89 ± 0.19	< 10
GJ 2	$P_{Rot}/2$	10.8 ± 0.1	2.81 ± 0.21	< 0.1
GJ 514	$P_{Rot}/2$	15.2 ± 0.1	1.55 ± 0.18	< 0.1
GJ 205	$P_{Rot}/3$	11.8 ± 0.1	1.92 ± 0.21	< 1
GJ 358	$P_{Rot}/2$	13.1 ± 0.1	3.61 ± 0.38	> 10
GJ 581	$P_{Rot}/2$	66.9 ± 0.1	1.41 ± 0.13	< 0.1

previously reported in the literature. We comment below on these, stars which are also listed in Table 4.12:

GJ 581: this star hosts a multi-planetary system, the real existence of some of the planets is being questioned from the analysis of chromospheric activity-time series. It was originally claimed to have 6 planets: planet b at $\sim 5.4d$ (Bonfils et al. 2005), planet c at $\sim 12.9d$ and d at $\sim 66.6d$ (Udry et al. 2007), planet e at $\sim 3.1d$ (Mayor et al. 2009b), and planets f $\sim 436d$ and g at $\sim 36d$ (Vogt et al. 2010). Planets d and g have been challenged as artefacts of stellar rotation (Robertson et al. 2014). Our own analysis of time series using HARPS spectra gives a rotation period of ~ 132 d for this star. This is about twice and 4 times the orbital periods of planet d and g, respectively (see Table 4.12). Boisse et al. (2011) explains the possible origin of this kind of signals as an effect of the latitude of the stellar structures and the line of sight. Our independent measurement of rotation period adds support to the conclusion of Robertson et al. (2014).

GJ 667C: this is a 5-planet candidate system: planets b at $\sim 7.2d$ and c at $\sim 28.1d$ (Bonfils et al. 2013), and planets d at $\sim 91.6d$, e at $\sim 62.2d$ and f at $\sim 39.0d$ (Gregory 2012; Anglada-Escudé et al. 2013). Recently, Robertson & Mahadevan (2014) and Feroz & Hobson (2014) claimed that planets d and e are artefacts induced by stellar rotation. Delfosse et al. (2013) had already identified the $91d$ signal as an alias of an $\sim 106d$ activity signal. Planet d, at 91 d, is relatively close to our rotational period of $103d$, but we also found a power excess at $\sim 91d$ in the $S_{\rm MW}$ periodogram, supporting the idea that the the signal is in fact an alias of the stellar rotation. For planet e, the claimed 62 d orbital period is very close to $P_{\rm rot} \cdot 2/3$ (Santos et al. 2014), casting doubts on its existence.

GJ 676A: this star has 4 detected planets: planet b at $\sim 1050d$ (Forveille et al. 2011), planet c at $\sim 4400d$, planet d at $\sim 3.6d$ and planet e at $\sim 35.4d$ (Anglada-Escudé & Tuomi 2012). The latter, planet e, has an orbital period compatible with our measured stellar rotation period ($41.2d$). This makes us suspect that it could be an activity-induced signal and not a real planet.

GJ 832: there are 2 potential planets: planet b at $\sim 3416d$ (Bailey et al. 2009) and planet c at $\sim 35.7d$ (Wittenmyer et al. 2014). The latter has an orbital period that falls inside the error bar of our value of stellar rotation period of $45.7d$, being really close to the Ca II H&K period measurement. Bonfils et al. (2013) also found the signal of planet c, but noticed a power excess at ~ 40 days in the bisector periodogram. Further investigation is needed in order to confirm or reject the existence of planet c.

HD 40307:After Mayor et al. (2009a) initial claim of 3 super-Earths at $40.3, 9.6$ and $20.4d$, Tuomi et al. (2013) expanded the system to six planets,

Table 4.12: Planet candidates with orbital periods close to rotation periods or harmonics of the rotation periods of stars in the sample

Star	P_{Rot} [d]	Planet	$P_{Orb.}$ [d]	K [ms^{-1}]	Ref
GJ581	132.5 ± 6.3	d	66.64 ± 0.08	2.63	1,8
		g	36.65 ± 0.52	1.5	2,8
GJ667C	103.9 ± 0.7	d	91.61 ± 0.89	1.52	3,9
		e	62.2 ± 0.55	0.92	3,9
GJ676A	41.2 ± 3.8	e	35.7 ± 0.07	2.62	4
GJ832	45.7 ± 9.3	c	35.68 ± 0.03	1.6	5
HD40307	31.8 ± 6.7	e	36.64 ± 0.20	0.85	6
HD41248	26.4 ± 1.1	b	18.36 ± 0.07	2.93	7,10
		c	25.65 ± 1.13	1.84	7,10

Ref: 1 - Udry et al. (2007), 2 – Vogt et al. (2010), 3 – Anglada-Escudé et al. (2013), 4 – Anglada-Escudé & Tuomi (2012), 5 – Wittenmyer et al. (2014), 6 – Tuomi et al. (2013) 7 – Jenkins et al. (2013) 8 – Robertson et al. (2014) 9 – Robertson & Mahadevan (2014), 10 – Santos et al. (2014)

planet e being a small super-Earth at ∼34.6 day orbital period. This period coincides within the uncertainties with our stellar rotation period measurement ($31.8d$) and therefore the existence of the planet is in question.

HD 41248: Jenkins et al. (2013) claimed the detection of two super-Earths, at periods ∼18 and ∼25 days. However, Santos et al. (2014) attributed these signals to the rotation period of the star at ∼25 d and to differential rotation (∼18 days) across different latitudes. Our analysis of time series of activity indicators confirm the stellar rotation period of ∼25 d and therefore adds support to the doubts raised concerning the existence of at least one of these planets.

4.4 Detected planetary signals

Along this work we analysed a sample of 133 stars with radial velocity data searching for signals with planetary origin. We recovered all the previously published planetary systems, and confirm all of them except for those cases stated in section 4.3.2. We detected 6 previously unreported planetary signals in 5 stars, along with several other tentative signals that require further investigation.

4.4.1 New Planets

We detect 5 new planetary signals in the stars HD 1581, HD 161098, HD 176986 and GJ 536 stars. In sec. 4.2 we show the detailed analysis of their radial velocity curves, and in sec. 3.2 the analysis of their activity behaviour. These detections are solid, except the second planet in HD 161098 for which we would still need more data to be confirmed. We also confirm the two planetary companions published by Affer et al. (2016) in the framework of this project.

Four of the detected planets are probably rocky planets, with minimum masses below 6 $M_\oplus$, being the most massive one (HD 161098 b) likely a Neptune-sized planet with a minimum-mass of 26.6 $M_\oplus$. Four of them are detected in close orbits, at period shorter than the stellar rotation period (HD 176986 b, GJ 536 b, GJ 3998 b & c). Two more at medium orbits, longer than the measured rotation period (HD 1581 b, HD 161098 c). And the last one at a very long orbit (HD 161098 b).

None of the solid detections is a potentially habitable planet. HD 1581 b, HD 176986 b, GJ 536 b and GJ 3998 b & c are too hot, with temperatures over 390 K even in situations of high albedo. HD 161098 b is too cold, with a temperature below 160 K. The only possible exception would be HD 161098 c, which in a high-albedo scenario (> 0.65) might reach temperatures below 360 K.

Table. 4.13 shows the parameters for the proposed new planets.

Additionally we detect 5 more radial velocity signals which seem to be originated by planetary companions. For the case of these signals the performed analysis is not as detailed, and therefore have to be considered tentative candidates. Table 4.14 shows the parameters for the suggested tentative candidates.

These tentative candidates require further investigation in order to validate their planetary origin and to properly characterise them. The cases of GJ 3942 b, GJ 521 b, GJ 507.1 b and GJ 552 b require more observations as the main limitation at this point is the lack of data.

The case of GJ 273 b, which is the most interesting of the pack, is different.

Table 4.13: Parameters for the new robust planet candidates

Star	$M \cdot sin(i)$ [$M_\oplus$]	Orbital Period [$days$]	Semimajor axis [a]	T^1_{EQ} [K]	T^2_{EQ} [K]
HD 1581 b	5.87 ± 0.99	64.434 ± 0.103	0.321 ± 0.005	510	390
HD 161098 b	26.60 ± 4.39	1569.005 ± 53.043	2.503 ± 0.072	160	120
HD 161098 c	5.30 ± 1.22	70.601 ± 0.179	0.317 ± 0.006	440	340
HD 176986 b	4.86 ± 0.66	6.493 ± 0.001	0.061 ± 0.001	920	710
GJ 536 b	5.47 ± 0.84	8.709 ± 0.002	0.066 ± 0.002	670	510
GJ 3998 b	2.35 ± 0.42	2.650 ± 0.001	0.029 ± 0.001	1000	770
GJ 3998 c	6.12 ± 1.11	13.725 ± 0.011	0.089 ± 0.003	570	440

Equilibrium temperatures are a rough estimate using the Stefan–Boltzmann law and assuming circular orbits and uniform equilibrium temperature over the entire planet for the case of [1] Earth albedo (0.29) and[2] high albedo (0.75).

Table 4.14: Parameters for the tentative candidates

Star	$M \cdot sin(i)$ [$M_\oplus$]	Orbital Period [$days$]	Semimajor axis [a]	T^1_{EQ} [K]	T^2_{EQ} [K]
GJ 3942 b	6.92 ± 1.42	6.90 ± 0.01	0.061 ± 0.019	820	630
GJ 521 b	13.92 ± 5.02	68.59 ± 0.27	0.255 ± 0.011	320	250
GJ 507.1 b	12.71 ± 3.02	19.50 ± 0.02	0.113 ± 0.005	520	400
GJ 552 b	5.11 ± 1.65	7.54 ± 0.01	0.059 ± 0.002	670	520
GJ 273 b	2.29 ± 0.64	18.48 ± 0.01	0.088 ± 0.007	360	280

Equilibrium temperatures are a rough estimate using the Stefan–Boltzmann law and assuming circular orbits and uniform equilibrium temperature over the entire planet for the case of [1] Earth albedo (0.29) and[2] high albedo (0.75).

The available data seems to be enough, but the system very complex. There are several radial velocity signals with different origins, whose origin is not trivial to asses. Much like the case of HD 176986 it requires a careful work in order to confirm that GJ 273 b is indeed a planet.

5

Conclusions and future work

5.1 Conclusions

Using more than 65 000 high resolution spectra from HARPS and HARPS-N, more than 71 000 photometric data from the ASAS survey and more than 21 000 S_{MW} measurements from the Mount Wilson HK Project, we have studied the stellar activity and radial velocities of a sample of 228 stars. We have calibrated the HARPS S_{MW} index into the Mount Wilson scale. We have measured the mean activity levels for the whole sample and used it to re-calibrate the $\log_{10}(R'_{\rm HK})$ with the goal of extending it into the realm of M-dwarfs.

We have analysed the photometric variations and the modulations in spectroscopic indicators of 176 stars to study magnetic cycles and rotation periods.

We present new measurements of magnetic cycles for 105 stars and rotation periods of 123 stars. The length of the detected magnetic cycles ranges from less than 2 years to more than 15 years. No correlation is found between length of cycles and the spectral type. We found some stars that show multiple cycles in which the short-term cycles are possibly flip-flop cycles. The length of the measured rotation periods goes from a fraction of a day up to more than 150 days. We do not find FGK stars with rotation periods longer than $\sim$ 50 days, only for M-dwarfs, specially fully convective M-dwarfs.

We have investigated the correlation between the chromospheric emission, represented by the $\log_{10}(R'_{\rm HK})$ index, and the derived rotation periods, and we have obtained a relationship between this index and the logarithm of the rotation period, which is valid for G,K and M-type stars in the range $\log_{10}(R'_{\rm HK}) \sim$ –4.0 to $\sim$ –6. This relationship allows us to predict the rotational period of late type stars with an accuracy better than the 23%.

A weak relationship between the activity level and the amplitude of the sun-like cycles can also be found when analysing photometric light curves of G to mid-M dwarfs. A relation is determined between the amplitudes and the rotation period. We find that the faster a star rotates the larger the amplitude of its cycle.

We find evidence for a correlation between the cycle length and the rotation period for the F, G and K main-sequence stars. For these stars the length of the cycle scales as D^l with $l = 0.89$.

We have analysed the radial velocity time series of 133 of those stars, finding new planet candidates and a number of activity induced radial velocity signals.

We provide measurements of 46 rotation-induced radial velocity signals along with 15 radial velocity signals at the harmonics of the rotation periods. We have investigated the correlation between the chromospheric emission, represented by the $\log_{10}(R'_{\rm HK})$ index and the measured semi amplitude of these RV signals, and we have obtained a specific linear relationship between this index and the logarithm of the amplitude for each spectral type. We have also investigated the correlation between the amplitude of the radial velocity signals and the amplitude in the activity signals, finding two different populations both with a strong correlation between the two amplitudes.

We see that M-type stars show a larger radial velocity amplitude for their induced signals than G and K-type stars. It has been stated that K-type stars show the smallest activity jitter Santos et al. (2000) but in our data we are not able to distinguish them from the G-type stars. Given their smaller mass this still makes K-type stars the best candidates to search for low mass exoplanets.

We report the discovery of 6 new planets around the stars HD 1581, HD 161098, HD 176986 and GJ 536 with the presence of another promising planetary signal in the data of HD 161098. HD 1581 is a 5.87 $M_\oplus$ planet orbiting at 0.321 au of its parent star with an equilibrium temperature of 510 K. HD 161098 b is a super-Neptune planet of 26.60 $M_\oplus$ orbiting at 2.503 au of its planets with an equilibrium temperature of 160 K. The hypothetical HD 161098 c would be a 5.30 $M_\oplus$ planet orbiting at 0.317 au of its star with an equilibrium temperature of 440 K, that would decrease to 340K in a high-albedo scenario. More observations are needed to confirm this object. HD 176986 b is a 4.86 $M_\oplus$ super-Earth located at 0.061 au of its star with an equilibrium temperature of 920 K. GJ 536 is a 5.3 $M_\oplus$ super-Earth located at 0.066 au of its parent star with an equilibrium temperature of 670 K. We confirm in an independent analysis the discovery of the two planets of the star GJ 3998 presented in Affer et al. (2016). GJ 3998 b is a small 2.35 $M_\oplus$ planet orbiting at 0.029 au of its star with an equilibrium temperature of 1000 K, and GJ 3998 c is a 6.12 $M_\oplus$ super-Earth located at 0.089 au from its star with an equilibrium temperature

of 570K.

We identify 5 tentative planet candidates around the stars GJ 3942, GJ 521, GJ 507.1, GJ 552 and GJ 273. The planet around GJ 273, if confirmed, would be particularly interesting as it would be a small 2.29 $M_{\oplus}$ planet in the habitable zone of the system. GJ 521 b would also be a planet in the habitable zone of the system.

5.2 Future work

The extensive dataset used in this study still has not been completely exploited. There are some systems where careful analysis might unveil new planet candidates, some where the complex activity patterns did not allowed us to see the planets yet. And some were new observations will increase the significance of the suggested signals.

The full HARPS dataset, ASAS archive and Mount Wilson data release are under-used assets so far. For the next years I plan on taking full advantage of the combined information those databases give, along with our own observations, in order to characterize the population of exoplanets and the stellar behaviour of the solar neighbourhood. Considering the huge amount of data of those archives, and the size of the Kepler or COROT archives, the upcoming GAIA data releases or the future ESPRESSO archive, it is very important to advance towards automatic tools of global analysis. They should be capable of taking all the information of a single star at once, identify the different periodic behaviours and analyse them together, separating the Keplerian and intrinsic components. A first draft of this kind of tool is used in this work, but so far its only useful as a pre-screening tool to identify interesting targets. Results require *human analysis* before being considered reliable. The obvious next step is to create an automatic tool capable of analysing combined data (spectroscopic, photometric, astrometric...) of large sets of stars, and to study the statistical properties of the sample.

The next year will also see the arrival of ESPRESSO and the 10 cm s^{-1} precision. We will not only see a huge number of new tiny extrasolar planets, but also the stellar induced radial velocity signals with a detail never seen before. At this point is not clear what are we going to encounter, but the scenario will probably be complicated. In order to take full advantage of the precision of ESPRESSO a very careful selection has to be made, taking into account both the long term and short term behaviour of the targets. Choosing between "high activity" and "low activity" targets will not be enough any more. As this work has shown even quiet stars induce radial velocity signals. Even a

state of the art selection will not free us from the stellar influence, and a very careful analysis of stellar activity will be necessary for every single target. As I expect to be linked to the ESPRESSO project I would like to continue the study of the activity induced signals with the improved precision of ESPRESSO to better characterize them and separate them from planetary signals.

Bibliography

Abt, H. A. 2009, ApJS, 180, 117

Abt, H. A., & Morrell, N. I. 1995, ApJS, 99, 135

Affer, L., Micela, G., Damasso, M., et al. 2016, ArXiv e-prints, arXiv:1607.03632

Anglada-Escudé, G., & Tuomi, M. 2012, A&A, 548, A58

Anglada-Escudé, G., Tuomi, M., Gerlach, E., et al. 2013, A&A, 556, A126

Anglada-Escudé, G., Amado, P. J., Barnes, J., et al. 2016, Nature, 536, 437

Astudillo-Defru, N., Bonfils, X., Delfosse, X., et al. 2015, A&A, 575, A119

Bailey, J., Butler, R. P., Tinney, C. G., et al. 2009, ApJ, 690, 743

Balachandran, S. 1990, ApJ, 354, 310

Baliunas, S. L., Henry, G. W., Donahue, R. A., Fekel, F. C., & Soon, W. H. 1997, AJ, 474, L119

Baliunas, S. L., Nesme-Ribes, E., Sokoloff, D., & Soon, W. H. 1996, ApJ, 460, 848

Baliunas, S. L., & Vaughan, A. H. 1985, ARA&A, 23, 379

Baliunas, S. L., Hartmann, L., Noyes, R. W., et al. 1983, ApJ, 275, 752

Baliunas, S. L., Donahue, R. A., Soon, W. H., et al. 1995, ApJ, 438, 269

Barclay, T., Rowe, J. F., Lissauer, J. J., et al. 2013, Nature, 494, 452

Barnard, E. E. 1916, AJ, 29, 181

Benedict, G. F., McArthur, B. E., Forveille, T., et al. 2002, ApJ, 581, L115

Berdyugina, S. V., & Järvinen, S. P. 2005, Astronomische Nachrichten, 326, 283

Berdyugina, S. V., & Tuominen, I. 1998, A&A, 336, L25

Berdyugina, S. V., & Usoskin, I. G. 2003, A&A, 405, 1121

Berta-Thompson, Z. K., Irwin, J., Charbonneau, D., et al. 2015, Nature, 527, 204

Boisse, I., Bouchy, F., Hébrard, G., et al. 2011, A&A, 528, A4

Bonanno, A., Elstner, D., Rüdiger, G., & Belvedere, G. 2002, A&A, 390, 673

Bonfils, X., Forveille, T., Delfosse, X., et al. 2005, A&A, 443, L15

Bonfils, X., Mayor, M., Delfosse, X., et al. 2007, A&A, 474, 293

Bonfils, X., Delfosse, X., Udry, S., et al. 2013, A&A, 549, A109

Boyajian, T. S., von Braun, K., van Belle, G., et al. 2012, ApJ, 757, 112

Brandt, P. N., & Solanki, S. K. 1990, A&A, 231, 221

Bubar, E. J., & King, J. R. 2010, AJ, 140, 293

Butler, R. P., Marcy, G. W., Fischer, D. A., et al. 1999, ApJ, 526, 916

Campbell, B., Walker, G. A. H., & Yang, S. 1988, ApJ, 331, 902

Catalano, S., & Marilli, E. 1983, AAP, 121, 190

Cayrel de Strobel, G., Lebreton, Y., Perrin, M.-N., & Cayrel, R. 1989, A&A, 225, 369

Chugainov, P. F. 1971, Information Bulletin on Variable Stars, 520, 1

Cincunegui, C., Díaz, R. F., & Mauas, P. J. D. 2007, A&A, 461, 1107

Corbally, C. J. 1984, ApJS, 55, 657

Corben, P. M., Carter, B. S., Banfield, R. M., & Harvey, G. M. 1972, Monthly Notes of the Astronomical Society of South Africa, 31, 7

Cosentino, R., Lovis, C., Pepe, F., et al. 2012, in Proc. SPIE, Vol. 8446, Ground-based and Airborne Instrumentation for Astronomy IV, 84461V

Cousins, A. W. J., & Stoy, R. H. 1962, Royal Greenwich Observatory Bulletins, 64

Crossfield, I. J. M., Petigura, E., Schlieder, J. E., et al. 2015, ApJ, 804, 10

Cumming, A. 2004, MNRAS, 354, 1165

Datson, J., Flynn, C., & Portinari, L. 2015, A&A, 574, A124

Delfosse, X., Forveille, T., Perrier, C., & Mayor, M. 1998, A&A, 331, 581

Delfosse, X., Bonfils, X., Forveille, T., et al. 2013, A&A, 553, A8

Donahue, R. A., Saar, S. H., & Baliunas, S. L. 1996, ApJ, 466, 384

Dorren, J. D., & Guinan, E. F. 1982, AJ, 87, 1546

Drake, S. A., Simon, T., & Linsky, J. L. 1989, ApJS, 71, 905

Dravins, D. 1982, ARA&A, 20, 61

Dravins, D. 1985, in Stellar Radial Velocities, ed. A. G. D. Philip & D. W. Latham, 311–320

Dravins, D., Lindegren, L., & Nordlund, A. 1981, A&A, 96, 345

Dressing, C. D., & Charbonneau, D. 2013, ApJ, 767, 95

Dressing, C. D., Charbonneau, D., & Newton, E. R. 2015, in AAS/Division for Extreme Solar Systems Abstracts, Vol. 3, AAS/Division for Extreme Solar Systems Abstracts, 501.03

Ducati, J. R. 2002, VizieR Online Data Catalog, 2237, 0

Dumusque, X., Boisse, I., & Santos, N. C. 2014, ApJ, 796, 132

Dumusque, X., Pepe, F., Lovis, C., & Latham, D. W. 2015, ApJ, 808, 171

Dumusque, X., Santos, N. C., Udry, S., Lovis, C., & Bonfils, X. 2011, A&A, 527, A82

Dumusque, X., Pepe, F., Lovis, C., et al. 2012, Nature, 491, 207

Ehrenreich, D., & Désert, J.-M. 2011, A&A, 529, A136

Favata, F., Micela, G., & Sciortino, S. 1997, A&A, 323, 809

Feroz, F., & Hobson, M. P. 2014, MNRAS, 437, 3540

Fisher, R. 1925, Statistical methods for research workers (Edinburgh Oliver & Boyd)

Forveille, T., Bonfils, X., Lo Curto, G., et al. 2011, A&A, 526, A141

Franchini, M., Morossi, C., Marcantonio, P. D., Malagnini, M. L., & Chavez, M. 2014, MNRAS, 442, 220

Frasca, A., Fröhlich, H.-E., Bonanno, A., et al. 2011, A&A, 532, A81

Gaidos, E. 2013, ApJ, 770, 90

Gomes da Silva, J., Santos, N. C., Bonfils, X., et al. 2011, A&A, 534, A30

—. 2012, A&A, 541, A9

Gray, R. O., Corbally, C. J., Garrison, R. F., et al. 2006, AJ, 132, 161

Gray, R. O., Corbally, C. J., Garrison, R. F., McFadden, M. T., & Robinson, P. E. 2003, AJ, 126, 2048

Gregory, P. C. 2012, ArXiv e-prints, arXiv:1212.4058

Hall, D. S., & Henry, G. W. 1994, International Amateur-Professional Photoelectric Photometry Communications, 55, 51

Hartmann, L., Soderblom, D. R., Noyes, R. W., Burnham, N., & Vaughan, A. H. 1984, ApJ, 276, 254

Hatzes, A. P. 2013, ApJ, 770, 133

Hatzes, A. P., Cochran, W. D., Endl, M., et al. 2003, ApJ, 599, 1383

Haywood, R. D., Cameron, A. C., Queloz, D., et al. 2012, in UK-Germany National Astronomy Meeting, Nam2012

Hempelmann, A., Schmitt, J. H. M. M., Schultz, M., Ruediger, G., & Stepien, K. 1995, A&A, 294, 515

Henry, T. J., Walkowicz, L. M., Barto, T. C., & Golimowski, D. A. 2002, AJ, 123, 2002

Herbig, G. H. 1977, ApJ, 214, 747

Høg, E., Fabricius, C., Makarov, V. V., et al. 2000, A&A, 355, L27

Horne, J. H., & Baliunas, S. L. 1986, ApJ, 302, 757

Houk, N., & Cowley, A. P. 1975, University of Michigan Catalogue of two-dimensional spectral types for the HD stars. Volume I. Declinations -90° to -53°

Houk, N., & Smith-Moore, M. 1988, Michigan Catalogue of Two-dimensional Spectral Types for the HD Stars. Volume 4, Declinations -26°.0 to -12°.0.

Houk, N., & Swift, C. 1999, in Michigan Spectral Survey, Ann Arbor, Dep. Astron., Univ. Michigan, Vol. 5, p. 0 (1999), Vol. 5, 0

Howard, A. W., Marcy, G. W., Bryson, S. T., et al. 2012, ApJS, 201, 15

Howard, A. W., Marcy, G. W., Fischer, D. A., et al. 2014, ApJ, 794, 51

Huélamo, N., Figueira, P., Bonfils, X., et al. 2008, A&A, 489, L9

Irwin, J., Berta, Z. K., Burke, C. J., et al. 2011, ApJ, 727, 56

Irwin, J., Berta-Thompson, Z. K., Charbonneau, D., Dittmann, J., & Newton, E. R. 2015, in American Astronomical Society Meeting Abstracts, Vol. 225, American Astronomical Society Meeting Abstracts, 258.01

Jacob, W. S. 1855, MNRAS, 15, 228

Jenkins, J. S., Tuomi, M., Brasser, R., Ivanyuk, O., & Murgas, F. 2013, ApJ, 771, 41

Jérémy Coffinet, A. 2015, IAU General Assembly, 22, 2254909

Johnson, H. L. 1966, ARA&A, 4, 193

Kiraga, M. 2012, Acta Astron., 62, 67

Kiraga, M., & Stepien, K. 2007, Acta Astron., 57, 149

Kirkpatrick, J. D., Henry, T. J., & McCarthy, Jr., D. W. 1991, ApJS, 77, 417

Koen, C., Kilkenny, D., van Wyk, F., & Marang, F. 2010, MNRAS, 403, 1949

Koleva, M., & Vazdekis, A. 2012, A&A, 538, A143

Kopparapu, R. K. 2013, ApJ, 767, L8

Kron, G. E. 1947, PASP, 59, 261

Lagrange, A.-M., Gratadour, D., Chauvin, G., et al. 2009, A&A, 493, L21

Lake, R. 1963, Monthly Notes of the Astronomical Society of South Africa, 22, 79

Léger, A., Rouan, D., Schneider, J., et al. 2009, A&A, 506, 287

Lépine, S., & Gaidos, E. 2013, Astronomische Nachrichten, 334, 176

Lépine, S., Hilton, E. J., Mann, A. W., et al. 2013, AJ, 145, 102

Lindegren, L., & Dravins, D. 2003, A&A, 401, 1185

Livingston, W. C. 1982, Nature, 297, 208

Lovis, C., & Pepe, F. 2007, A&A, 468, 1115

Lovis, C., Ségransan, D., Mayor, M., et al. 2011a, A&A, 528, A112

Lovis, C., Dumusque, X., Santos, N. C., et al. 2011b, ArXiv e-prints, arXiv:1107.5325

Maldonado, J., Affer, L., Micela, G., et al. 2015, A&A, 577, A132

Mann, A. W., Feiden, G. A., Gaidos, E., Boyajian, T., & von Braun, K. 2015, ApJ, 804, 64

Marcy, G. W., Butler, R. P., Vogt, S. S., Fischer, D., & Lissauer, J. J. 1998, ApJL, 505, L147

Markwardt, C. B. 2009, in Astronomical Society of the Pacific Conference Series, Vol. 411, Astronomical Data Analysis Software and Systems XVIII, ed. D. A. Bohlender, D. Durand, & P. Dowler, 251

Mayor, M., & Queloz, D. 1995, Nature, 378, 355

Mayor, M., Pepe, F., Queloz, D., et al. 2003, The Messenger, 114, 20

Mayor, M., Udry, S., Lovis, C., et al. 2009a, A&A, 493, 639

Mayor, M., Bonfils, X., Forveille, T., et al. 2009b, A&A, 507, 487

Mayor, M., Marmier, M., Lovis, C., et al. 2011, ArXiv e-prints, arXiv:1109.2497

Mekkaden, M. V. 1985, Ap&SS, 117, 381

Messina, S., & Guinan, E. F. 2002, A&A, 393, 225

Meunier, N., Desort, M., & Lagrange, A.-M. 2010, A&A, 512, A39

Middelkoop, F. 1982, A&A, 107, 31

Middelkoop, F., Vaughan, A. H., & Preston, G. W. 1981, A&A, 96, 401

Mishenina, T. V., Pignatari, M., Korotin, S. A., et al. 2013, A&A, 552, A128

Montes, D., Crespo-Chacón, I., Gálvez, M. C., et al. 2004, Lecture Notes and Essays in Astrophysics, 1, 119

Montet, B. T., Crepp, J. R., Johnson, J. A., Howard, A. W., & Marcy, G. W. 2014, ApJ, 781, 28

Morgan, W. W., & Keenan, P. C. 1973, ARA&A, 11, 29

Moss, D. 2004, MNRAS, 352, L17

Neves, V., Bonfils, X., Santos, N. C., et al. 2014, A&A, 568, A121

Noyes, R. W., Hartmann, L. W., Baliunas, S. L., Duncan, D. K., & Vaughan, A. H. 1984, ApJ, 279, 763

Oja, T. 1985, A&AS, 61, 331

—. 1993, A&AS, 100, 591

Oláh, K., Kolláth, Z., Granzer, T., et al. 2009, A&A, 501, 703

Pallavicini, R., Golub, L., Rosner, R., et al. 1981, ApJ, 248, 279

Parker, E. N. 1955, ApJ, 122, 293

Pepe, F., Mayor, M., Delabre, B., et al. 2000, in SPIE, Vol. 4008, Optical and IR Telescope Instrumentation and Detectors, ed. M. Iye & A. F. Moorwood, 582–592

Pepe, F., Lovis, C., Ségransan, D., et al. 2011, A&A, 534, A58

Pepe, F., Cristiani, S., Rebolo, R., et al. 2013, The Messenger, 153, 6

Petigura, E. A., Howard, A. W., & Marcy, G. W. 2013, Proceedings of the National Academy of Science, 110, 19273

Pojmanski, G. 1997, Acta Astron., 47, 467

Pont, F., Aigrain, S., & Zucker, S. 2011, MNRAS, 411, 1953

Prugniel, P., Vauglin, I., & Koleva, M. 2011, A&A, 531, A165

Queloz, D., Henry, G. W., Sivan, J. P., et al. 2001, A&A, 379, 279

Radick, R. R., & Lockwood, G. W. 1983, in BAAS, Vol. 15, Bulletin of the American Astronomical Society, 655

Radick, R. R., Skiff, B. A., & Lockwood, G. W. 1990, ApJ, 353, 524

Ramírez, I., Allende Prieto, C., & Lambert, D. L. 2013, ApJ, 764, 78

Rivera, E. J., Lissauer, J. J., Butler, R. P., et al. 2005, ApJ, 634, 625

Robertson, P., Endl, M., Cochran, W. D., & Dodson-Robinson, S. E. 2013, ApJ, 764, 3

Robertson, P., Endl, M., Henry, G. W., et al. 2015, ArXiv e-prints, arXiv:1501.02807

Robertson, P., & Mahadevan, S. 2014, ApJ, 793, L24

Robertson, P., Mahadevan, S., Endl, M., & Roy, A. 2014, Science, 345, 440

Rojas-Ayala, B., Covey, K. R., Muirhead, P. S., & Lloyd, J. P. 2012, ApJ, 748, 93

Rutten, R. G. M. 1984, A&A, 130, 353

Saar, S. H., & Brandenburg, A. 1999, ApJ, 524, 295

—. 2002, Astronomische Nachrichten, 323, 357

Saar, S. H., & Donahue, R. A. 1997, ApJ, 485, 319

Santos, N. C., Mayor, M., Naef, D., et al. 2000, A&A, 361, 265

Santos, N. C., Sousa, S. G., Mortier, A., et al. 2013, A&A, 556, A150

Santos, N. C., Mortier, A., Faria, J. P., et al. 2014, A&A, 566, A35

Savanov, I. S. 2012, Astronomy Reports, 56, 716

Simon, T., & Fekel, Jr., F. C. 1987, ApJ, 316, 434

Skumanich, A. 1972, ApJ, 171, 565

Sousa, S. G., Santos, N. C., Israelian, G., Mayor, M., & Udry, S. 2011, A&A, 533, A141

Sousa, S. G., Santos, N. C., Mayor, M., et al. 2008, A&A, 487, 373

Steenbeck, M., Krause, F., & Rädler, K.-H. 1966, Zeitschrift Naturforschung Teil A, 21, 369

Stephenson, C. B. 1986, AJ, 92, 139

Strassmeier, K. G., Bartus, J., Cutispoto, G., & Rodono, M. 1997, A&AS, 125, 11

Suárez Mascareño, A., Rebolo, R., & González Hernández, J. I. 2016, ArXiv e-prints, arXiv:1607.03049

Suárez Mascareño, A., Rebolo, R., González Hernández, J. I., & Esposito, M. 2015, MNRAS, 452, 2745

Tsantaki, M., Sousa, S. G., Adibekyan, V. Z., et al. 2013, A&A, 555, A150

Tuomi, M., Anglada-Escudé, G., Gerlach, E., et al. 2013, A&A, 549, A48

Udry, S., Bonfils, X., Delfosse, X., et al. 2007, A&A, 469, L43

Upgren, A. R., Grossenbacher, R., Penhallow, W. S., MacConnell, D. J., & Frye, R. L. 1972, AJ, 77, 486

van de Kamp, P. 1963, AJ, 68, 515

van Leeuwen, F. 2007, A&A, 474, 653

Vaníček, P. 1971, Ap&SS, 12, 10

Vaughan, A. H., Preston, G. W., Baliunas, S. L., et al. 1981, ApJ, 250, 276

Vilhu, O. 1984, A&A, 133, 117

Vogt, S. S., Butler, R. P., Rivera, E. J., et al. 2010, ApJ, 723, 954

Walter, F. M., & Bowyer, S. 1981, ApJ, 245, 671

Wang, S. X., & Wright, J. T. 2012, BOOTTRAN: Error Bars for Keplerian Orbital Parameters, Astrophysics Source Code Library, ascl:1210.030

Ward-Duong, K., Patience, J., De Rosa, R. J., et al. 2015, MNRAS, 449, 2618

West, A. A., Weisenburger, K. L., Irwin, J., et al. 2015, ApJ, 812, 3

Wildi, F., Pepe, F., Chazelas, B., Lo Curto, G., & Lovis, C. 2010, in SPIE, Vol. 7735, Ground-based and Airborne Instrumentation for Astronomy III, 77354X

Wilken, T., Curto, G. L., Probst, R. A., et al. 2012, Nature, 485, 611

Wittenmyer, R. A., Tuomi, M., Butler, R. P., et al. 2014, ApJ, 791, 114

Wolszczan, A., & Frail, D. A. 1992, Nature, 355, 145

Wright, D. J., Wittenmyer, R. A., Tinney, C. G., Bentley, J. S., & Zhao, J. 2016, ApJL, 817, L20

Wright, J., & Howard, A. 2012, RVLIN: Fitting Keplerian curves to radial velocity data, Astrophysics Source Code Library, ascl:1210.031

Zechmeister, M., & Kürster, M. 2009, A&A, 496, 577

A

Sample and data

Table A.1: Relevant information for the stars of the sample.

Star	Sp. Type	m_B	m_V	$T_{\rm eff}$ (K)	Mass ($M_\odot$)	[Fe/H] (dex)	Dist. (pc)
HD 73262	A0	4.16	4.14				49.2
HD 216956	A4	1.25	1.16				7.7
HD 135559	A5	5.80	5.63				46.1
HD 16555	A6	5.56	5.30				45.6
HD 129926	F0	5.29	4.94				30.3
HD 40136	F2	4.05	3.72	6989	1.45	–0.10	14.9
HD 157950	F3	4.93	4.54				30.1
HD 77370	F4	5.58	5.16				26.4
HD 7439	F5	5.59	5.13			–0.02	23.4
HD 30652	F6	3.63	3.19	6470	1.28	0.00	8.1
HD 101198	F6.5	6.00	5.48	6184		-0.27	26.7
HD 222368	F7	4.62	4.12	6211	1.19	–0.12	13.7
HD 25171	F8	8.29	7.78	6160	1.41	–0.11	55.0
HD 19994	F8.5	5.63	5.07	6315	1.31	0.27	22.6
HD 203608	F9	4.70	4.22	6150	0.93	–0.63	9.3
HD 1581	F9.5	4.80	4.23	5990	1.03	–0.18	8.6
HD 4307	F9.5	6.76	6.15	5840	0.99	–0.21	31.0
HD 2151	G0	3.41	2.79	5819	1.15	–0.13	7.5

Continued on next page

Table A.1 – *Continued from previous page*

HD 134060	G0	6.91	6.29	5966	1.05	0.14	24.2
HD 1388	G0	79	6.50	5954	1.05	–0.01	27.2
HD 197210	G0	8.31	7.61	5563	0.94	–0.03	30.6
HD 10180	G1	7.95	7.32	5898	1.06	0.07	39.0
HD 7134	G1	8.05	7.46	5979	0.95	–0.27	40.7
HD 30495	G1.5	6.14	5.50	5790	1.01	0.02	13.3
HD 128620	G2	0.72	0.01	5809	1.11	0.23	1.3
HD 2071	G2	7.95	7.27	5719	0.95	–0.09	27.2
HD 1320	G2	8.63	7.98	5699	0.91	–0.27	36.4
HD 213575	G2	7.62	6.95	5676	0.94	–0.15	36.4
HD 21019	G2	6.90	6.20	5468	1.02	–0.45	37.1
HD 41248	G2	9.42	8.81	5713	0.86	–0.37	52.4
HD 217014	G2.5	6.12	5.46	5752	1.08	0.19	15.6
HD 1835	G3	7.05	6.39	5849		0.22	20.9
HD 1461	G3	7.14	6.46	5765	1.11	0.19	23.2
HD 20766	G4	6.18	5.54	5712	0.92	–0.24	12.0
HD 146233	G5	6.15	5.50	5810	1.05	0.05	13.9
HD 12264	G5	8.64	7.98	5781	0.98	–0.06	42.7
HD 4915	G6	7.64	6.97	5660	0.94	–0.21	21.5
HD 59468	G6.5	7.43	6.71	5820	0.92	0.01	22.7
HD 115617	G7	5.44	4.74	5537	0.89	–0.03	8.6
HD 20794	G8	4.98	4.27	5398		–0.46	6.0
HD 190248	G8	4.32	3.56	5566	0.97	0.33	6.1
HD 210277	G8	7.34	6.63	5470	0.92	0.15	21.6
HD 161098	G8	8.31	7.67	5560	0.82	–0.27	30.2
HD 10700	G8.5	4.22	3.50	5322		–0.52	3.7
HD 7438	G9	8.65	7.87	5325		–0.24	31.2
HD 63765	G9	8.85	8.10	5432	0.83	–0.16	33.3
HD 20781	G9.5	9.26	8.44	5236	0.82	–0.12	35.4
HD 165341 A	K0	4.89	4.03	5306		0.00	5.1
HD 8389 A	K0	8.74	7.84	5182	0.90	0.36	30.5
HD 220256	K0	9.41	8.56	5090	0.79	–0.14	33.6
HD 203384	K0	8.80	8.02	5564	0.99	0.26	39.0
CoRoT-7	K0	12.52	11.67	5288	0.85	02	149.9
HD 26965	K0.5	5.25	4.43	5098	0.75	–0.31	5.0
HD 82558	K0.5	8.76	7.89				18.6
HD 128621	K1	2.21	1.33	5230	0.91	0.27	1.3

Continued on next page

Table A.1 – *Continued from previous page*

HD 155885	K1	5.93	5.08	5091		–0.30	6.0
HD 20165	K1	8.68	7.80	5148		–0.08	18.1
HD 224789	K1	9.12	8.24	5185	0.78	–03	29.9
HD 22049	K2	4.61	3.73	5049	0.78	–0.15	3.2
HD 204941	K2	9.39	8.48	4997	0.76	–0.20	26.9
V 660 Tau	K2	13.66	12.60				
HD 191408	K2.5	6.19	5.31	4969	0.69	–0.52	6.0
HD 4628	K2.5	6.64	5.74	4905		–0.36	7.5
HD 40307	K2.5	8.10	7.15	4977	0.77	–0.31	13
HD 176986	K2.5	9.39	8.45	5018	0.73	00	26.4
HD 220339	K2.5	8.70	7.80	4938	0.72	–0.37	19.1
HD 215152	K2.5	9.12	8.13	4935	0.70	–0.10	
HD 16160	K3	6.81	5.83	4829		–0.16	7.3
HD 32147	K3	7.27	6.21	4745	0.78	0.19	8.7
HD 170493	K3	9.11	8.00	4658	0.77	0.22	18.6
HD 104067	K3	8.90	7.92	4888	0.78	–0.04	21.1
V 410 Tau	K3	12.13	10.75				98.2
HD 82342	K3.5	9.31	8.32	4470		–0.54	19.3
HD 131977	K4	6.83	5.72	4683		–0.24	5.8
HD 216803	K4	7.58	6.48	4710			7.6
HD 125595	K4	10.13	93	4691	0.76	0.08	28
HD 118100	K4	10.55	9.37	4313		-0.16	20.2
HD 101581	K4.5	8.83	7.76	4615	0.7	–0.51	12.4
HD 209100	K5	5.75	4.69	4649	0.71	–0.20	3.6
HD 156026	K5	7.50	6.34	4600	0.65	–0.34	6.0
HIP 5158	K5	11.29	10.21	4813		0.17	41.2
HD 120467	K5.5	9.43	8.17				14.3
HD 85512	K6	8.83	7.65	4715	0.74	–0.32	11.2
HD 203040	K6.5	10.45	9.09	4005		-0.05	16.2
HD 211970	K7	10.34	8.99				13.5
StKM 1-347	K7	12.20	11.06	3774			50.0
HD 132683	K8	10.87	9.47				19.3
HD 113538	K9	10.43	9.06	4685		–0.17	15.9
GJ 229	M0	9.61	8.12	3799	0.55	–0.10	5.8
GJ 884	M0	9.25	7.87	3894		–0.47	8.2
GJ 846	M0	10.62	9.15	3835	0.59	–0.09	10.2
GJ 184	M0	11.36	9.94	3752	0.54	–0.10	13.6

Continued on next page

Table A.1 – *Continued from previous page*

GJ 731	M0	11.59	10.10	3844	0.57	–0.16	15.5
GJ 548 A	M0	11.17	9.72	3903	0.63	–0.13	16.4
GJ 3942	M0	11.59	10.25	3867	0.63	–0.04	16.9
GJ 4057	M0	12.26	10.77	3873	0.59	–0.15	21.8
GJ 9482	M0	11.80	10.38				23.6
GJ 9404	M0	12.04	10.64	3875	0.45	–0.20	25.4
TYC 743-1836-1	M0	12.03	10.79	3846	0.62	–0.03	25.6
GJ 4092	M0	12.24	10.86	3858	0.62	–0.06	26.0
TYC 3973-2034-1	M0	12.24	10.90	3720			28.6
G 125–69	M0	12.26	10.98				28.6
GJ 119 A	M0	11.77	10.46	3761	0.55	–0.08	30.2
TYC 694–1183–1	M0	12.66	11.21				33.3
GJ 9793	M0	11.90	10.51	3881			33.9
HIP 17248	M0	12.69	11.24	3822			35.2
2MASS J22+37[1]	M0	13.33	12.00	3891	0.62	–0.13	40.0
K2–3	M0	13.52	12.17				50.0
GJ 784	M0.5	9.42	7.97				6.2
GJ 803	M0.5	10.05	8.63		0.75		9.9
GJ 740	M0.5	10.67	9.22	3845	0.58	–0.14	10.9
GJ 507 A	M0.5	11.09	9.62	3550			13.3
GJ 685	M0.5	11.45	9.97	3816	0.55	–0.15	14.1
GJ 4306	M0.5	11.76	10.47	3763	0.53	–0.13	15.4
GJ 21	M0.5	12.03	10.56	6746	0.53	–0.12	16.5
GJ 3822	M0.5	12.10	10.64	3821	0.56	–0.13	19.9
GJ 694.2	M0.5	12.09	10.86	3847	0.55	–0.21	21.5
Wolf 59	M0.5	12.65	11.19	3810	0.59	–0.06	25.0
GJ 9689	M0.5	12.67	11.23	3824	0.57	–0.13	26.2
GJ 191	M1	10.43	8.85	3587	0.35	–0.39	3.9
GJ 1	M1	102	8.56	3482	–0.27	0.33	4.3
GJ 412 A	M1	10.27	8.78	3631	0.38	–0.38	4.8
GJ 393	M1	11.15	9.65	3544	0.41	–0.17	7.1
GJ 514	M1	10.52	93	3728	0.51	–0.14	7.7
GJ 686	M1	11.11	9.58	3663	0.42	–0.30	8.1
GJ 536	M1	11.18	9.71	3685	0.52	–0.08	10.1
GJ 3997	M1	11.80	10.37	3754	0.49	–0.24	12.5
GJ 606	M1	12.00	10.49	3665	0.46	–0.21	13.9

Continued on next page

[1] 2MASS J22353504+3712131

Table A.1 – *Continued from previous page*

GJ 3649	M1	12.19	10.85	3691	0.50	–0.14	16.7
GJ 9122 B	M1	12.27	10.76	3730	0.51	–0.16	16.7
GJ 3998	M1	12.34	10.83	3722	0.50	–0.16	17.8
GJ 1074	M1	12.39	10.93	3765	0.52	–0.16	19.3
GJ 119 B	M1	13.00	11.70	3508	0.47	0.05	24.2
GJ 3352	M1	12.56	11.05	3809	0.56	–0.13	25.5
GJ 3186	M1	12.55	11.05	3768	0.53	–0.14	27.7
GJ 4196	M1	12.41	11.11	3666	0.56	0.07	27.9
GJ 832	M1.5	10.18	8.67	3446	0.45	–0.17	5.0
GJ 205	M1.5	9.44	7.97	3800	0.60	0.00	5.7
GJ 185 A	M1.5	10.35	9.00				7.7
GJ 49	M1.5	11.06	9.50	3712	0.55	–0.03	10.0
GJ 16	M1.5	12.39	10.86	3673	0.48	–0.16	16.3
GJ 220	M1.5	12.37	10.80	3570			16.9
LP 198–637	M1.5	12.46	10.90	3728	0.54	–0.06	18.2
GJ 4182	M1.5	12.43	10.89	3650			32.3
GJ 887	M2	8.82	7.34	3507	0.47	–0.24	3.3
GJ 15 A	M2	9.63	8.13	3607	0.38	–0.34	3.6
GJ 526	M2	9.89	8.50	3609	0.47	–0.10	5.4
GJ 693	M2	12.42	10.78	3232	0.26	–0.28	5.8
GJ 908	M2	10.43	8.99	3553	0.42	0.37	6.0
GJ 880	M2	10.14	8.64	3602	0.58	0.03	6.8
GJ 701	M2	10.88	9.36	3510	0.48	–0.27	7.8
GJ 382	M2	10.76	9.26	3653	0.46	–0.06	7.9
GJ 450	M2	11.30	9.72	3649	0.45	–0.20	8.6
GJ 433	M2	11.32	9.81	3618	0.47	–0.13	8.9
GJ 2	M2	11.45	9.97	3713	0.51	–0.14	11.3
GJ 70	M2	12.45	10.91	3511	0.37	–0.21	11.4
GJ 410	M2	11.05	9.57	3640			11.8
GJ 414 B	M2	12.39	10.72	3661	0.50	–0.09	12.5
GJ 47	M2	12.26	10.87	3525	0.36	–0.26	12.8
GJ 3126	M2	12.45	10.95	3505	0.45	0.01	12.8
GJ 895	M2	11.56	10.05	3560			13.0
GJ 521	M2	11.50	10.26	3601	0.47	–0.09	13.0
GJ 272	M2	12.12	10.53	3747	0.50	–0.19	16.4
GJ 507.1	M2	12.16	10.55	3710	0.51	–0.13	17.0
GJ 3014	M2	12.63	11.12	3695	0.48	–0.19	19.6
StKM 1–587	M2	12.86	11.39	3896	0.69	0.04	20.0

Continued on next page

Table A.1 – *Continued from previous page*

GJ 1030	M2	12.91	11.40	3658	0.50	–0.08	22.1
G 215–12	M2	12.94	11.43	3687	0.50	–0.12	26.5
GJ 563.2A	M2	13.13	11.66				28.6
StKM 1–650	M2	13.36	12.03	3874	0.61	–0.11	33.3
GJ 588	M2.5	10.81	9.31	3291	0.47	0.06	5.9
GJ 176	M2.5	11.49	9.95	3603	0.03	0.52	9.3
GJ 162	M2.5	11.69	10.16	3746	0.50	–0.19	13.4
GJ 552	M2.5	12.18	10.68	3589	0.47	–0.09	14.0
GJ 399	M2.5	12.79	11.28	3563	0.55	0.15	16.4
G 234–57	M2.5	12.80	11.30	3616	0.50	–0.05	16.9
GJ 476	M2.5	12.85	11.40	3498	0.38	–0.16	18.3
GJ 3117 A	M2.5	12.92	11.51	3549	0.43	0.09	22.2
G 214–14	M2.5	13.15	11.55	3832	0.58	–0.11	22.7
GJ 4100	M2.5	13.68	12.18				27.8
GJ 3470	M2.5	13.77	12.27	3470		0.08	28.8
GJ 674	M3	10.97	9.41	3334	0.35	–0.23	4.5
GJ 388	M3	10.98	9.43	3473	0.47	0.12	4.7
GJ 752 A	M3	10.63	9.12	3339	0.48	0.05	5.9
GJ 581	M3	12.17	10.57	3248	0.30	–0.20	6.2
GJ 625	M3	11.80	10.17	3499	0.30	–0.38	6.5
GJ 408	M3	11.58	10.02	3472	0.35	–0.19	6.7
GJ 667 C	M3	11.79	10.22	3445	0.30	–0.50	7.1
GJ 480.1	M3	13.97	12.24		0.18		7.8
GJ 793	M3	12.23	10.68	3461	0.33	–0.21	8.0
GJ 438	M3	11.88	10.39	3647	0.43	–0.27	8.4
GJ 877	M3	11.87	10.38	3507	0.43	–0.24	8.6
HIP 31292	M3	12.88	11.42				8.7
GJ 357	M3	12.48	10.92	3477	0.32	–0.27	9.0
GJ 358	M3	12.21	10.69	3450	0.42	0.04	9.5
GJ 479	M3	12.20	10.66	3218	0.43	0.01	9.7
GJ 680	M3	11.67	10.13	3390	0.47	–0.19	9.7
GJ 436	M3	12.06	10.59	3354		–0.03	10.1
GJ 671	M3	12.93	11.37	3422	0.31	–0.17	12.4
GJ 26	M3	12.60	11.24	3484	0.37	–0.17	12.7
GJ 2128	M3	13.09	11.53	3518	0.34	–0.30	14.9
BPM 96441	M3	13.30	11.90	3896	0.50	–0.12	25.0
GJ 729	M3.5	12.23	10.49	3240	0.17	–0.18	3.0
GJ 273	M3.5	11.44	9.87	3090	0.27	–0.01	3.8

Continued on next page

Table A.1 – *Continued from previous page*

GJ 628	M3.5	11.64	10.07	3057	0.30	–0.02	4.3
GJ 682	M3.5	12.59	10.95	2912	0.27	0.10	5.1
GJ 300	M3.5	13.70	12.13	2841	0.26	0.13	8.0
GJ 486	M3.5	12.96	11.39		0.32		8.4
GJ 257 A	M3.5	13.04	11.48	3290			9.5
TYC 2710–691-1	M3.5	13.14	11.52	3867	0.65	0.02	10.0
StKM 1–1877	M3.5	13.24	11.69	3822	0.64	0.06	12.5
GJ 163	M3.5	13.30	11.81	3276		0.07	15.0
GJ 317	M3.5	13.55	11.98	3106		0.22	15.3
GJ 54.1	M4	13.88	12.07	3088	0.13	–0.45	3.7
GJ 234	M4	12.76	11.07	3039		0.13	4.1
GJ 3618	M4	15.74	13.92	3000			4.8
G 99–49	M4	13.01	11.31	3214		0.07	5.2
GJ 3323	M4	13.92	12.20	3143		-0.06	5.3
LP 816–60	M4	13.03	11.46	3405	0.23	0.06	5.7
GJ 213	M4	13.13	11.51	3082	0.22	–0.11	5.8
GJ 555	M4	12.91	11.32	2839	0.28	0.13	6.1
GJ 402	M4	13.32	11.68	3334	0.26	0.20	6.8
GJ 4248	M4	13.45	11.80				7.4
GJ 105 B	M4	13.28	11.66	3284		-0.12	7.7
GJ 447	M4.5	12.90	11.15	3382	0.23	–0.25	3.4
GJ 83.1	M4.5	14.10	12.30	3080		-0.16	4.5
GJ 876	M4.5	11.75	10.19	2954	0.34	0.14	4.7
GJ 754	M4.5	13.93	12.23		0.18		5.9
GJ 285	M4.5	12.83	11.22	3045	0.31	0.40	6.0
GJ 3737	M4.5	14.43	12.74				6.4
GJ 299	M4.5	14.60	12.83	3021	0.14	–0.46	6.8
GJ 4274	M4.5	15.09	13.30	3039	0.34	0.38	7.5
GJ 1224	M4.5	15.44	13.48	3245	0.30	–0.05	7.5
GJ 831 A	M4.5	13.67	12.01				8.3
GJ 1154	M4.5	15.40	13.64	3040		0.28	8.4
GJ 1214	M4.5	16.40	14.67	3245		0.20	14.6
GJ 551	M5.5	13.04	11.13	3050	0.12		1.3
GJ 1061	M5.5	14.98	13.07		0.12		3.7

References for spectral types: Abt & Morrell (1995), Corbally (1984),Ehrenreich & Désert (2011), Gray et al. (2003), Gray et al. (2006), Houk & Cowley

(1975), Houk & Swift (1999), Stephenson (1986), Upgren et al. (1972), Maldonado et al. (2016 *submitted*), Abt (2009),Morgan & Keenan (1973), Houk & Smith-Moore (1988), Herbig (1977),Lépine et al. (2013),Kirkpatrick et al. (1991),Stephenson (1986), Crossfield et al. (2015), ?, Henry et al. (2002),?

References for photometry: Ducati (2002), Høg et al. (2000), Lake (1963), Cousins & Stoy (1962), Léger et al. (2009), Koen et al. (2010), Corben et al. (1972),Oja (1985),Oja (1993)

References for temperatures, masses & metallicities: Balachandran (1990),Datson et al. (2015), Favata et al. (1997),Sousa et al. (2008), Mishenina et al. (2013), Sousa et al. (2011), Santos et al. (2013), Neves et al. (2014), Maldonado et al. (2015), Affer et al. (2016), Ramírez et al. (2013), Tsantaki et al. (2013), Koleva & Vazdekis (2012), Franchini et al. (2014), Bonfils et al. (2013),Rojas-Ayala et al. (2012), Cayrel de Strobel et al. (1989), Maldonado et al. (2016 *submitted*), Prugniel et al. (2011), Bubar & King (2010), Lépine et al. (2013), Mann et al. (2015), Boyajian et al. (2012)

References for distances: van Leeuwen (2007)

Table A.2: Available data for the stars of our sample

Star	Sp. Type	HARPS N_{Meas}	HARPS–N N_{Meas}	MW HK N_{Meas}	ASAS N_{Meas}
HD 73262	A0	4			
HD 216956	A4	10			
HD 135559	A5	7			383
HD 16555	A6	1			
HD 129926	F0	1		3	381
HD 40136	F2	32			
HD 157950	F3	8			
HD 77370	F4	1			
HD 7439	F5	28		12	342
HD 30652	F6	31			425
HD 101198	F6.5	74			
HD 222368	F7	67			
HD 25171	F8	50			485
HD 19994	F8.5	918			

Continued on next page

Table A.2 – *Continued from previous page*

HD 203608	F9	1971			998
HD 1581	F9.5	1728			738
HD 4307	F9.5	72		192	432
HD2151	G0	2711			1018
HD134060	G0	304			487
HD1388	G0	114		224	351
HD197210	G0	18	132		404
HD10180	G1	307			540
HD7134	G1	21	107		435
HD30495	G1.5	82		391	558
HD 128620	G2	4737			1396
HD 2071	G2	51			671
HD 1320	G2	20			644
HD 213575	G2	22			
HD 21019	G2	46		15	373
HD 41248	G2	208			1207
HD 217014	G2.5	81			248
HD 1835	G3	10		2173	
HD 1461	G3	444		210	349
HD 20766	G4	59			
HD 146233	G5	4832		697	
HD 12264	G5	16	129		433
HD 4915	G6	54	150		250
HD 59468	G6.5	472			
HD 115617	G7	1193		1366	407
HD 20794	G8	4949			583
HD 190248	G8	3867			656
HD 210277	G8	21	135	125	307
HD 161098	G8	121	138		471
HD 10700	G9	8117		1764	
HD 7438	G9		142	3	
HD 63765	G9	51			604
HD 20781	G9.5	204			
HD 165341 A	K0	1256		1074	
HD 8389 A	K0	29	145		509
HD 220256	K0	23	137		288

Continued on next page

Table A.2 – *Continued from previous page*

HD 203384	K0	21	135		344
CoRoT–7	K0	163			432
HD 26965	K0.5	325		1155	321
HD 82558	K0.5	1		108	502
HD 128621	K1	8969			1179
HD 155885	K1	4		1493	581
HD 20165	K1		117	93	301
HD 224789	K1	30			505
HD 22049	K2	414	256	4332	637
HD 204941	K2	52	116		652
HD 191408	K2.5	60			
HD 4628	K2.5	144		1660	339
HD 40307	K2.5	365			871
HD 220339	K2.5	12	159		311
HD 176986	K2.5	134	144		425
HD 16160	K3	217		1457	
HD 32147	K3	126		981	493
HD 170493	K3	29	132	3	
HD 104067	K3	84			822
HD 82342	K3.5	44			632
HD 131977	K4	42		3	440
HD 216803	K4	206			
HD 125595	K4	121			736
HD 101581	K4.5	6			
HD 209100	K5	4048			512
HD 156026	K5			1503	
HIP 5158	K5	62			521
HD 120467	K5.5	9			
HD 85512	K6	713			720
HD 203040	K6.5	4			
HD 211970	K7	6			
StKM 1–347	K7		1		
HD 132683	K8	5			
HD 113538	K9	46			1020
GJ 229	M0	101			727
GJ 884	M0	2			
GJ 846	M0	51			316

Continued on next page

Table A.2 – *Continued from previous page*

GJ 184	M0		39		
GJ 731	M0		15		411
GJ 548 A	M0		26		
GJ 3942	M0		91		
GJ 4057	M0		80		327
GJ 9482	M0	36			553
GJ 9404	M0		31		77
TYC 743–1836–1	M0				325
GJ 4092	M0	12	12		386
TYC 3973–2034–1	M0		2		
G 125–69	M0		2		
GJ 119 A	M0		79		
TYC 694–1183–1	M0		2		273
GJ 9793	M0		23		462
HIP 17248	M0		2		
2MASS J22+37[2]	M0		4		
K 2–3	M0		10		457
GJ 784	M0.5	38			575
GJ 803	M0.5	15			461
GJ 740	M0.5	52	73		458
GJ 507 A	M0.5		5		
GJ 685	M0.5		42	154	
GJ 4306	M0.5		104		241
GJ 21	M0.5		74		
GJ 3822	M0.5	62	38		312
GJ 694 2	M0.5		94		
Wolf 59	M0.5		1		
GJ 9689	M0.5		54		273
GJ 191	M1	22			213
GJ1	M1	42			50
GJ412A	M1		61	3	
GJ 393	M1	139			
GJ 514	M1	106			345
GJ 686	M1	19	2		581
GJ 536	M1	141	12		359
GJ 3997	M1		58		455

Continued on next page

[2] 2MASS J22353504+3712131

Table A.2 – *Continued from previous page*

GJ 606	M1	22	24	442
GJ 3649	M1		16	552
GJ 9122B	M1		41	367
GJ 3998	M1	6	129	554
GJ 1074	M1		25	
GJ 119B	M1		3	
GJ 3352	M1		7	
GJ 3186	M1		1	117
GJ 4196	M1		1	
GJ 832	M1.5	53		486
GJ 205	M1.5	71		641
GJ 185A	M1.5	2		922
GJ 49	M1.5		63	
GJ 16	M1.5	8	94	302
GJ 220	M1.5		4	307
LP 198–637	M1.5		1	
GJ 4182	M1.5		9	
GJ 887	M2	74		58
GJ 15 A	M2		78	
GJ 526	M2	29		297
GJ 693	M2	103		185
GJ 908	M2	69	7	319
GJ 880	M2	71		230
GJ 701	M2	108		406
GJ 382	M2	28		501
GJ 450	M2		19	
GJ 433	M2	82		590
GJ 2	M2		78	
GJ 70	M2	9	19	312
GJ 410	M2	10	18	257
GJ 414 B	M2		27	
GJ 47	M2		60	
GJ 3126	M2		2	
GJ 895	M2		2	
GJ 521	M2		49	
GJ 272	M2		6	
GJ 507.1	M2		47	
GJ 3014	M2		1	

Continued on next page

Table A.2 – *Continued from previous page*

StKM 1–587	M2		8	
GJ 1030	M2	7	4	225
G 215–12	M2		1	
GJ 563.2A	M2	9		432
StKM 1–650	M2			
GJ 588	M2.5	176		532
GJ 176	M2.5	63		438
GJ 162	M2.5		52	
GJ 552	M2.5	8	57	323
GJ 399	M2.5	8	27	652
G 234–57	M2.5		31	
GJ 476	M2.5	11	11	372
GJ 3117 A	M2.5		8	
G 214–14	M2.5		7	
GJ 4100	M2.5	50		395
GJ 3470	M2.5	86		326
GJ 674	M3	131		544
GJ 388	M3	40		371
GJ 752A	M3	72		394
GJ 581	M3	185		716
GJ 625	M3		91	
GJ 408	M3		30	279
GJ 667C	M3	172		69
GJ 480.1	M3	8		735
GJ 793	M3		23	
GJ 438	M3	18		610
GJ 877	M3	38		1068
HIP 31292	M3	23		
GJ 357	M3	46		574
GJ 358	M3	33		1001
GJ 479	M3	54		571
GJ 680	M3	34		863
GJ 436	M3	156		210
GJ 671	M3		6	
GJ 26	M3		19	
GJ 2128	M3	6	16	468
BPM 96441	M3		12	
GJ 729	M3.5	8		627

Continued on next page

Table A.2 – *Continued from previous page*

GJ 273	M3.5	242		379
GJ 628	M3.5	128		520
GJ 682	M3.5	18		
GJ 300	M3.5	35		750
GJ 486	M3.5	11		343
GJ 257 A	M3.5	2		
TYC 2710–691–1	M3.5		1	
StKM 1–1877	M3.5		58	
GJ 163	M3.5	160		654
GJ 317	M3.5	75		581
GJ 699	M4	179	10	374
GJ 54.1	M4	15		458
GJ 234	M4	15		459
GJ 3618	M4	5		
G 99–49	M4	1		440
GJ 3323	M4			598
LP 816–60	M4	79		421
GJ 213	M4	34		510
GJ 555	M4	11		504
GJ 402	M4	6		
GJ 4248	M4	5		
GJ 105 B	M4	20		299
GJ 447	M4.5	79		379
GJ 83.1	M4.5	22		234
GJ 876	M4.5	221		387
GJ 754	M4.5	81		283
GJ 285	M4.5	7		535
GJ 3737	M4.5	10		572
GJ 299	M4.5	18		
GJ 4274	M4.5	4		
GJ 1224	M4.5	9		
GJ 831A	M4.5	1		
GJ 1154	M4.5			314
GJ 1214	M4.5	76		24
GJ 551	M5.5	210		1016
GJ 1061	M5.5	4		842

Table A.3: Time span of the observations for the stars of our sample

Star	Sp. Type	HARPS T_{Span} (d)	HARPS–N T_{Span} (d)	MW HK T_{Span} (d)	ASAS T_{Span} (d)
HD 73262	A0	30			
HD 216956	A4	2182			
HD 135559	A5	105			3157
HD 16555	A6	1			
HD 129926	F0	1		1	3160
HD 40136	F2	1395			
HD 157950	F3	367			
HD 77370	F4	1			
HD 7439	F5	1577		3064	3264
HD 30652	F6	388			2648
HD 101198	F6.5	1339			
HD 222368	F7	2533			
HD 25171	F8	4111			3215
HD 19994	F8.5	4035			
HD 203608	F9	104			3273
HD 1581	F9.5	3606			3277
HD 4307	F9.5	1818		3448	2724
HD 2151	G0	1421			3296
HD 134060	G0	3244			3134
HD 1388	G0	3397		865	2715
HD 197210	G0	2831	428		3148
HD 10180	G1	3706			3217
HD 7134	G1	3662	388		3232
HD 30495	G1.5	864		6217	3299
HD 128620	G2	1811			3124
HD 2071	G2	3700			3079
HD 1320	G2	3230			3289
HD 213575	G2	2955			
HD 21019	G2	3259		17	2969
HD 41248	G2	3689			3298
HD 217014	G2.5	113			2372
HD 1835	G3	322		10394	
HD 1461	G3	3958		865	2959

Continued on next page

Table A.3 – *Continued from previous page*

HD 20766	G4	1401			
HD 146233	G5	3887		7344	
HD 12264	G5	710	427		3289
HD 4915	G6	1362	428		3176
HD 59468	G6.5	2754			
HD 115617	G7	4155		6250	3094
HD 20794	G8	3627			3294
HD 190248	G8	3174			3272
HD 210277	G8	3649	428	4909	2950
HD 161098	G8	3027	428		3155
HD 10700	G8.5	3187		10036	
HD 7438	G9		427	1	
HD 63765	G9	2302			3290
HD 20781	G9.5	3782			
HD 165341 A	K0	5		9064	
HD 8389 A	K0	3359	427		3295
HD 220256	K0	2222	428		3273
HD 203384	K0	2890	428		3270
CoRoT–7	K0	1437			3188
HD 26965	K0.5	3262		9983	3162
HD 82558	K0.5	1		2655	3291
HD 128621	K1	1831			3113
HD 155885	K1	1		10214	3150
HD 20165	K1		414	4035	3269
HD 224789	K1	2610			3275
HD 22049	K2	1035	415	9984	3295
HD 204941	K2	2896	415		3238
HD 191408	K2.5	1365			
HD 4628	K2.5	1770		10393	2727
HD 40307	K2.5	3755			3235
HD 176986	K2.5	3585	428		3165
HD 220339	K2.5	3229	428		3239
HD 16160	K3	1776		9972	
HD 32147	K3	1776		9980	3187
HD 170493	K3	2946	428	1	
HD 104067	K3	2270			3294
HD 82342	K3.5	3756			3294

Continued on next page

Table A.3 – *Continued from previous page*

HD 131977	K4	2627		1	3126
HD 216803	K4	200			
HD 125595	K4	2075			3192
HD 101581	K4.5	1155			
HD 209100	K5	4267			2541
HD 156026	K5			10548	
HIP 5158	K5	2933			3296
HD 120467	K5.5	4039			
HD 85512	K6	2055			3262
HD 203040	K6.5	1750			
HD 211970	K7	1378			
StKM 1–347	K7		1		
HD 132683	K8	2167			
HD 113538	K9	3802			3213
GJ 229	M0	4016			3299
GJ 884	M0	2725			
GJ 846	M0	2345			3289
GJ 184	M0		933		
GJ 731	M0		706		2416
GJ 548 A	M0		419		
GJ 3942	M0		869		
GJ 4057	M0		869		2398
GJ 9482	M0	3032			3187
GJ 9404	M0		969		546
TYC 743–1836–1	M0				2543
GJ 4092	M0	280	415		2944
TYC 3973–2034–1	M0		42		
G 125–69	M0		3		
GJ 119 A	M0		873		
TYC 694–1183–1	M0		413		2543
GJ 9793	M0		951		2379
HIP 17248	M0		89		
2MASS J22+37[3]	M0		175		
K 2–3	M0		24		3168
GJ 784	M0.5	3229			3226

Continued on next page

[3] 2MASS J22353504+3712131

Table A.3 – *Continued from previous page*

GJ 803	M0.5	3824			3232
GJ 740	M0.5	1501	869		2950
GJ 507 A	M0.5		12		
GJ 685	M0.5		851	96	
GJ 4306	M0.5		950		2345
GJ 21	M0.5		1010		
GJ 3822	M0.5	1770	800		2389
GJ 694.2	M0.5		868		
Wolf 59	M0.5		1		
GJ 9689	M0.5		917		2379
GJ 191	M1	1782			1079
GJ 1	M1	2063			369
GJ 412 A	M1		1016	1	
GJ 393	M1	4159			
GJ 514	M1	3634			2926
GJ 686	M1	2298	2		2396
GJ 536	M1	4274	30		3153
GJ 3997	M1		863		2411
GJ 606	M1	2256	706		3181
GJ 3649	M1		284		2384
GJ 9122 B	M1		1011		2547
GJ 3998	M1	94	868		2593
GJ 1074	M1		978		
GJ 119 B	M1		140		
GJ 3352	M1		17		
GJ 3186	M1		1		2546
GJ 4196	M1		1		
GJ 832	M1.5	2777			3256
GJ 205	M1.5	1049			3294
GJ 185 A	M1.5	67			3295
GJ 49	M1.5		796		
GJ 16	M1.5	1496	868		3214
GJ 220	M1.5		2		2543
LP 198–637	M1.5		0		
GJ 4182	M1.5		125		
GJ 887	M2	1407			1268
GJ 15 A	M2		868		
GJ 526	M2	1790			2389

Continued on next page

Table A.3 – *Continued from previous page*

GJ 693	M2	3672		2461
GJ 908	M2	2185	866	3279
GJ 880	M2	3636		2345
GJ 701	M2	3930		3147
GJ 382	M2	1187		3294
GJ 450	M2		969	
GJ 433	M2	2490		3178
GJ 2	M2		1008	
GJ 70	M2	1763	823	3248
GJ 410	M2	3324	34	2381
GJ 414 B	M2		424	
GJ 47	M2		792	
GJ 3126	M2		406	
GJ 895	M2		4	
GJ 521	M2		1046	
GJ 272	M2		317	
GJ 507.1	M2		818	
GJ 3014	M2		1	
StKM 1–587	M2		60	
GJ 1030	M2	647	46	2520
G 215–12	M2		1	
GJ 563.2A	M2	90		3133
StKM 1–650	M2			
GJ 588	M2.5	3271		3184
GJ 176	M2.5	2146		2544
GJ 162	M2.5		964	
GJ 552	M2.5	22	952	2389
GJ 399	M2.5	777	737	3288
G 234–57	M2.5		794	
GJ 476	M2.5	1048	331	2932
GJ 3117 A	M2.5		827	
G 214–14	M2.5		410	
GJ 4100	M2.5	1956		3131
GJ 3470	M2.5	1548		2546
GJ 674	M3	3580		3182
GJ 388	M3	3672		2350
GJ 752 A	M3	3609		2944
GJ 581	M3	1889		3179

Continued on next page

Table A.3 – *Continued from previous page*

GJ 625	M3		1064	
GJ 408	M3		950	2381
GJ 667 C	M3	2893		3136
GJ 480.1	M3	1655		3170
GJ 793	M3		868	
GJ 438	M3	2978		3170
GJ 877	M3	2937		3295
HIP 31292	M3	3374		
GJ 357	M3	2521		3294
GJ 358	M3	2656		3278
GJ 479	M3	1060		3188
GJ 680	M3	2961		3189
GJ 436	M3	1531		2383
GJ 671	M3		263	
GJ 26	M3		823	
GJ 2128	M3	94	414	2959
BPM 96441	M3		410	
GJ 729	M3.5	511		3156
GJ 273	M3.5	4157		2932
GJ 628	M3.5	3668		3160
GJ 682	M3.5	2613		
GJ 300	M3.5	2322		3290
GJ 486	M3.5	2533		2932
GJ 257 A	M3.5	372		
TYC 2710–691–1	M3.5		1	
StKM 1–1877	M3.5		908	
GJ 163	M3.5	3704		3263
GJ 317	M3.5	1440		3296
GJ 699	M4	2234	6	2573
GJ 54.1	M4	2163		3287
GJ 234	M4	20		3183
GJ 3618	M4	1906		
G 99–49	M4	1		3202
GJ 3323	M4			3294
LP 816–60	M4	3748		3116
GJ 213	M4	3406		2544
GJ 555	M4	2496		3185
GJ 402	M4	2693		

Continued on next page

Table A.3 – *Continued from previous page*

GJ 4248	M4	2531	
GJ 105 B	M4	2408	3244
GJ 447	M4.5	3206	3168
GJ 83.1	M4.5	1780	2527
GJ 876	M4.5	3088	3286
GJ 754	M4.5	2442	3051
GJ 285	M4.5	71	3187
GJ 3737	M4.5	3153	3170
GJ 299	M4.5	2551	
GJ 4274	M4.5	2527	
GJ 1224	M4.5	2179	
GJ 831 A	M4.5	1	
GJ 1154	M4.5		3162
GJ 1214	M4.5	1207	1545
GJ 551	M5.5	3515	3179
GJ 1061	M5.5	1656	3297

B

Measurement of stellar activity in Late type dwarfs

Table B.1: S_{MW} measurements and S_{MW} RMS for the stars of our sample.

Star	Sp. Type	S_{MW}	RMS (S_{MW})
HD 7439	F5	0.1593	0.0088
HD 30652	F6	0.2257	0.0053
HD 101198	F6.5	0.1469	0.0009
HD 222368	F7	0.1626	0.0022
HD 25171	F8	0.1520	0.0106
HD 19994	F8.5	0.1634	0.0027
HD 203608	F9	0.1656	0.0038
HD 1581	F9.5	0.1638	0.0013
HD 4307	F9.5	0.1465	0.0033
HD 2151	G0	0.1448	0.0008
HD 134060	G0	0.1559	0.0015
HD 1388	G0	0.1553	0.0036
HD 197210	G0	0.1911	0.0059
HD 10180	G1	0.1563	0.0026
HD 7134	G1	0.1611	0.0018
HD 30495	G1.5	0.2948	0.0131
HD 128620	G2	0.1491	0.0010

Continued on next page

Table B.1 – *Continued from previous page*

HD 2071	G2	0.1839	0.0057
HD 1320	G2	0.1852	0.0054
HD 213575	G2	0.1472	0.0024
HD 21019	G2	0.1482	0.0044
HD 41248	G2	0.1788	0.0059
HD 217014	G2.5	0.1518	0.0009
HD 1835	G3	0.3416	0.0156
HD 1461	G3	0.1544	0.0040
HD 20766	G4	0.2492	0.0151
HD 146233	G5	0.1713	0.0066
HD 12264	G5	0.2770	0.0142
HD 4915	G6	0.2019	0.0061
HD 59468	G6.5	0.1607	0.0029
HD 115617	G7	0.1629	0.0039
HD 20794	G8	0.1662	0.0015
HD 190248	G8	0.1451	0.0023
HD 210277	G8	0.1495	0.0030
HD 161098	G8	0.1810	0.0044
HD 10700	G8.5	0.1722	0.0025
HD 7438	G9	0.2478	0.0078
HD 63765	G9	0.2444	0.0181
HD 20781	G9.5	0.1625	0.0040
HD 165341A	K0	0.3701	0.0210
HD 8389A	K0	0.1803	0.0112
HD 220256	K0	0.1799	0.0075
HD 203384	K0	0.1647	0.0062
CoRoT-7	K0	0.3543	0.0453
HD 26965	K0.5	0.1954	0.0180
HD 82558	K0.5	1.3667	0.1088
HD 128621	K1	0.2162	0.0153
HD 155885	K1	0.3949	0.0205
HD 20165	K1	0.2018	0.0139
HD 224789	K1	0.5553	0.0185
HD 22049	K2	0.5255	0.0261
HD 204941	K2	0.2145	0.0105
HD 191408	K2.5	0.1823	0.0055
HD 4628	K2.5	0.2195	0.0175

Continued on next page

Table B.1 – *Continued from previous page*

HD 40307	K2.5	0.2065	0.0177
HD 176986	K2.5	0.2944	0.0160
HD 220339	K2.5	0.2585	0.0176
HD 215152	K3	0.2729	0.0244
HD 16160	K3	0.2311	0.0222
HD 32147	K3	0.2794	0.0236
HD 170493	K3	0.4236	0.0301
HD 104067	K3	0.3782	0.0193
HD 82342	K3.5	0.2292	0.0224
HD 131977	K4	0.4540	0.0236
HD 216803	K4	1.1225	0.0263
HD 125595	K4	0.5212	0.0312
HD 101581	K4.5	0.5157	0.0188
HD 209100	K5	0.4540	0.0224
HD 156026	K5	0.7933	0.1131
HIP 5158	K5	0.3663	0.0547
HD 120467	K5.5	0.6671	0.1259
HD 85512	K6	0.4698	0.0398
HD 203040	K6.5	1.9341	0.0412
HD 211970	K7	1.3088	0.2179
HD 132683	K8	1.7449	0.1368
HD 113538	K9	1.2672	0.1393
GJ 229	M0	1.7427	0.1300
GJ 884	M0	1.7804	0.1748
GJ 846	M0	2.0663	0.1171
GJ 184	M0	0.9037	0.0569
GJ 731	M0	1.4849	0.1336
GJ 548A	M0	1.9611	0.1325
GJ 3942	M0	2.5184	0.1744
GJ 4057	M0	1.3915	0.0957
GJ 9482	M0	1.9503	0.1192
GJ 9404	M0	1.7971	0.1941
GJ 4092	M0	1.2478	0.0988
TYC 3973-2034-1	M0	1.6176	0.6598
G 125-69	M0	0.7444	0.0108
GJ 119 A	M0	1.1285	0.0683
TYC 694-1183-1	M0	2.4726	0.2649

Continued on next page

Table B.1 – *Continued from previous page*

GJ 9793	M0	2.5968	0.1797
HIP 17248	M0	6.8641	0.0921
2MASS J22+37[1]	M0	2.1473	0.1175
K2-3	M0	1.1560	0.1917
GJ 784	M0.5	1.7883	0.1373
GJ 803	M0.5	10.6973	1.0239
GJ 740	M0.5	1.6609	0.1295
GJ 507A	M0.5	1.3578	0.0883
GJ 685	M0.5	2.2628	0.2533
GJ 4306	M0.5	2.0674	0.1479
GJ 21	M0.5	2.4250	0.1575
GJ 3822	M0.5	2.4471	0.2052
GJ 694 2	M0.5	1.6364	0.0945
GJ 9689	M0.5	1.6122	0.1478
GJ 191	M1	0.3039	0.0234
GJ 1	M1	0.4406	0.0581
GJ 412A	M1	0.5371	0.0317
GJ 393	M1	1.1016	0.0994
GJ 514	M1	1.1916	0.0980
GJ 686	M1	0.7744	0.0574
GJ 536	M1	1.3721	0.1189
GJ 3997	M1	0.8304	0.0804
GJ 606	M1	2.0668	0.2479
GJ 3649	M1	2.0969	0.1977
GJ 9122 B	M1	2.0654	0.1704
GJ 3998	M1	1.5696	0.1127
GJ 1074	M1	1.8373	0.1479
GJ 119 B	M1	0.8638	0.0811
GJ 3352	M1	1.8518	0.0730
GJ 832	M1.5	0.8646	0.1025
GJ 205	M1.5	2.3659	0.1583
GJ 185 A	M1.5	1.7750	0.0295
GJ 49	M1.5	2.9560	0.1307
GJ 16	M1.5	1.6744	0.1566
GJ 220	M1.5	1.2024	0.0948
GJ 4182	M1.5	1.4530	0.2438

Continued on next page

[1] 2MASS J22353504+3712131

Table B.1 – *Continued from previous page*

GJ 887	M2	1.3149	0.1378
GJ 15 A	M2	0.5853	0.0566
GJ 526	M2	0.8568	0.0789
GJ693	M2	0.6979	0.1642
GJ 908	M2	0.5316	0.0562
GJ 880	M2	1.8708	0.1657
GJ 701	M2	1.1095	0.1195
GJ 382	M2	2.2414	0.1750
GJ 450	M2	2.2599	0.2926
GJ 433	M2	0.8763	0.0872
GJ 2	M2	1.9963	0.1467
GJ 70	M2	1.1518	0.1566
GJ 410	M2	4.7301	0.4904
GJ 414 B	M2	1.6284	0.1189
GJ 47	M2	1.1333	0.1391
GJ 3126	M2	1.0299	0.0197
GJ 895	M2	1.7099	0.1314
GJ 521	M2	0.9444	0.1010
GJ 272	M2	1.6389	0.3500
GJ 50701	M2	1.0271	0.0719
StKM 1-587	M2	1.7312	0.4443
GJ 1030	M2	2.2284	0.2910
GJ 563.2A	M2	0.6908	0.1336
GJ 588	M2.5	1.0179	0.0944
GJ 176	M2.5	1.8648	0.1799
GJ 162	M2.5	1.9834	0.1916
GJ 552	M2.5	1.2727	0.1040
GJ 399	M2.5	0.9800	0.1560
G 234-57	M2.5	3.7640	0.5991
GJ 476	M2.5	0.7736	0.0778
GJ 3117 A	M2.5	1.6340	0.1595
G 214-14	M2.5	1.2359	0.1599
GJ 4100	M2.5	2.1180	0.3692
GJ 3470	M2.5	1.8853	0.3536
GJ 674	M3	1.9364	0.2889
GJ 388	M3	10.5224	1.0159
GJ 752A	M3	1.1809	0.1212
GJ 581	M3	0.5398	0.0748

Continued on next page

Table B.1 – *Continued from previous page*

GJ 625	M3	0.7292	0.0895
GJ 408	M3	1.0475	0.1036
GJ 667 C	M3	0.6093	0.0778
GJ 480.1	M3	1.0171	0.2121
GJ 793	M3	1.8294	0.2245
GJ 438	M3	0.6737	0.0787
GJ 877	M3	0.8372	0.0940
HIP 31292	M3	1.2050	0.1695
GJ 357	M3	0.5389	0.1021
GJ 358	M3	3.7749	0.4824
GJ 479	M3	2.5301	0.2436
GJ 680	M3	1.0382	0.1100
GJ 436	M3	0.7686	0.0869
GJ 671	M3	0.7168	0.0499
GJ 26	M3	1.2453	0.1688
GJ 2128	M3	0.6820	0.0886
BPM 96441	M3	1.9999	0.0959
GJ 729	M3.5	9.0035	2.4850
GJ 273	M3.5	0.8619	0.0925
GJ 628	M3.5	0.7809	0.1239
GJ 682	M3.5	1.2706	0.1647
GJ 300	M3.5	1.5684	0.2050
GJ 486	M3.5	0.6351	0.1112
GJ 257 A	M3.5	0.6418	0.2476
StKM 1-1877	M3.5	8.9714	0.7581
GJ 163	M3.5	0.7974	0.1121
GJ 317	M3.5	1.2503	0.2355
GJ 699	M4	0.7030	0.0993
GJ 54.1	M4	5.9670	1.1367
GJ 234	M4	15.1398	7.4084
GJ 3618	M4	1.4566	0.9319
LP 816-60	M4	1.6049	0.2576
GJ 213	M4	0.5229	0.1495
GJ 555	M4	1.0576	0.1053
GJ 402	M4	1.2739	0.1563
GJ 4248	M4	0.9809	0.2498
GJ 105 B	M4	0.8321	0.1438
GJ 447	M4.5	1.4314	0.2696

Continued on next page

Table B.1 – *Continued from previous page*

GJ 83.1	M4.5	8.8106	2.0057
GJ 876	M4.5	1.0670	0.1161
GJ 754	M4.5	1.1670	0.4238
GJ 285	M4.5	25.1450	2.2961
GJ 3737	M4.5	0.7677	0.2110
GJ 299	M4.5	1.0202	0.4090
GJ 4274	M4.5	22.1513	2.4504
GJ 1224	M4.5	15.3537	4.0268
GJ 1214	M4.5	1.6999	0.4903
GJ 551	M5.5	13.3804	2.5656
GJ 1061	M5.5	2.5388	0.5318

Table B.2: $\log_{10}$R'$_{HK}$ measurements and RMS for the stars of our sample

Star	Sp. Type	$\log_{10}$R'$_{HK}$	RMS ($\log_{10}$R'$_{HK}$)
HD 7439	F5	-4.846	0.052
HD 30652	F6	-4.562	0.017
HD 101198	F6.5	-4.923	0.006
HD 222368	F7	-4.829	0.012
HD 25171	F8	-4.890	0.064
HD 19994	F8.5	-4.841	0.013
HD 203608	F9	-4.811	0.020
HD 1581	F9.5	-4.842	0.005
HD 4307	F9.5	-4.951	0.019
HD 2151	G0	-4.966	0.005
HD 134060	G0	-4.908	0.008
HD 1388	G0	-4.894	0.019
HD 197210	G0	-4.816	0.020
HD 10180	G1	-4.909	0.013
HD 7134	G1	-4.865	0.009
HD 30495	G1.5	-4.504	0.025
HD 128620	G2	-5.000	0.005
HD 2071	G2	-4.826	0.021
HD 1320	G2	-4.798	0.020
HD 213575	G2	-4.981	0.013
HD 21019	G2	-4.997	0.023

Continued on next page

Table B.2 – *Continued from previous page*

HD 41248	G2	-4.797	0.024
HD 217014	G2.5	-4.951	0.005
HD 1835	G3	-4.439	0.025
HD 1461	G3	-4.951	0.020
HD 20766	G4	-4.601	0.036
HD 146233	G5	-4.853	0.028
HD 12264	G5	-4.555	0.029
HD 4915	G6	-4.757	0.020
HD 59468	G6.5	-4.948	0.013
HD 115617	G7	-4.927	0.017
HD 20794	G8	-4.920	0.006
HD 190248	G8	-5.064	0.012
HD 210277	G8	-4.998	0.016
HD 161098	G8	-4.829	0.017
HD 10700	G8.5	-4.904	0.010
HD 7438	G9	-4.733	0.018
HD 63765	G9	-4.710	0.043
HD 20781	G9.5	-5.044	0.017
HD 165341A	K0	-4.605	0.029
HD 8389A	K0	-5.065	0.040
HD 220256	K0	-5.006	0.027
HD 203384	K0	-4.990	0.026
Corot-7	K0	-4.616	0.067
HD 26965	K0.5	-4.919	0.058
HD 82558	K0.5	-3.993	0.036
HD 128621	K1	-4.927	0.043
HD 155885	K1	-4.559	0.027
HD 20165	K1	-4.969	0.043
HD 224789	K1	-4.426	0.016
HD 22049	K2	-4.453	0.024
HD 204941	K2	-4.970	0.029
HD 191408	K2.5	-5.033	0.020
HD 4628	K2.5	-4.943	0.048
HD 40307	K2.5	-5.046	0.052
HD 176986	K2.5	-4.829	0.030
HD 220339	K2.5	-4.847	0.039
HD 215152	K2.5	-4.940	0.050

Continued on next page

Table B.2 – *Continued from previous page*

HD 16160	K3	-5.020	0.056
HD 32147	K3	-5.031	0.047
HD 170493	K3	-4.883	0.036
HD 104067	K3	-4.746	0.026
HD 82342	K3.5	-5.042	0.057
HD 131977	K4	-4.854	0.026
HD 216803	K4	-4.406	0.011
HD 125595	K4	-4.770	0.029
HD 101581	K4.5	-4.730	0.018
HD 209100	K5	-4.776	0.025
HD 156026	K5	-4.665	0.067
HIP 5158	K5	-4.917	0.078
HD 120467	K5.5	-4.924	0.092
HD 85512	K6	-4.952	0.043
HD 203040	K6.5	-4.625	0.010
HD 211970	K7	-4.765	0.077
HD 132683	K8	-4.725	0.036
HD 113538	K9	-4.838	0.051
GJ 229	M0	-4.906	0.034
GJ 884	M0	-4.694	0.045
GJ 846	M0	-4.804	0.026
GJ 184	M0	-5.085	0.030
GJ 731	M0	-4.978	0.042
GJ 548 A	M0	-4.784	0.031
GJ 3942	M0	-4.457	0.031
GJ 4057	M0	-5.034	0.032
GJ 9482	M0	-4.732	0.028
GJ 9404	M0	-4.725	0.049
GJ 4092	M0	-4.851	0.037
TYC 3973-2034-1	M0	-4.657	0.186
G 125-69	M0	-4.906	0.007
GJ 119 A	M0	-4.765	0.028
TYC 694-1183-1	M0	-4.681	0.048
GJ 9793	M0	-4.539	0.031
HIP 17248	M0	-4.228	0.006

Continued on next page

Table B.2 – *Continued from previous page*

2MASS J22+37[2]	M0	-4.509	0.025
K2-3	M0	-4.830	0.077
GJ 784	M0.5	-4.834	0.035
GJ 803	M0.5	-3.979	0.042
GJ 740	M0.5	-4.874	0.036
GJ 507 A	M0.5	-4.997	0.030
GJ 685	M0.5	-4.783	0.051
GJ 4306	M0.5	-4.452	0.032
GJ 21	M0.5	-4.731	0.029
GJ 3822	M0.5	-4.711	0.038
GJ 694.2	M0.5	-4.450	0.026
GJ 9689	M0.5	-4.855	0.042
GJ 191	M1	-6.046	0.053
GJ 1	M1	-5.534	0.072
GJ 412 A	M1	-5.494	0.031
GJ 393	M1	-5.161	0.043
GJ 514	M1	-5.111	0.039
GJ 686	M1	-5.400	0.037
GJ 536	M1	-4.992	0.040
GJ 3997	M1	-5.147	0.047
GJ 606	M1	-4.892	0.055
GJ 3649	M1	-4.539	0.042
GJ 9122 B	M1	-4.871	0.038
GJ 3998	M1	-5.014	0.033
GJ 1074	M1	-4.836	0.037
GJ 119 B	M1	-4.872	0.045
GJ 3352	M1	-4.938	0.018
GJ 832	M1.5	-5.284	0.058
GJ 205	M1.5	-4.753	0.030
GJ 185 A	M1.5	-4.633	0.008
GJ 49	M1.5	-4.833	0.020
GJ 16	M1.5	-5.019	0.043
GJ 220	M1.5	-5.271	0.038
GJ 4182	M1.5	-5.115	0.078
GJ 887	M2	-5.033	0.049
GJ 15 A	M2	-5.471	0.050

Continued on next page

[2]2MASS J22353504+3712131

Table B.2 – *Continued from previous page*

GJ 526	M2	-5.058	0.044
GJ 693	M2	-5.699	0.124
GJ 908	M2	-5.378	0.055
GJ 880	M2	-4.922	0.041
GJ 701	M2	-5.194	0.051
GJ 382	M2	-4.815	0.035
GJ 450	M2	-4.999	0.059
GJ 433	M2	-5.288	0.049
GJ 2	M2	-4.840	0.033
GJ 70	M2	-5.213	0.065
GJ 410	M2	-4.447	0.046
GJ 414 B	M2	-5.358	0.035
GJ 47	M2	-4.918	0.057
GJ 3126	M2	-5.191	0.009
GJ 895	M2	-4.974	0.035
GJ 521	M2	-4.721	0.050
GJ 272	M2	-5.170	0.100
GJ 507.1	M2	-5.438	0.034
StKM 1-587	M2	-4.884	0.118
GJ 1030	M2	-4.853	0.059
GJ 563.2 A	M2	-5.332	0.097
GJ 588	M2.5	-5.205	0.045
GJ 176	M2.5	-4.997	0.044
GJ 162	M2.5	-4.949	0.044
GJ 552	M2.5	-5.090	0.038
GJ 399	M2.5	-5.234	0.077
G 234-57	M2.5	-4.597	0.071
GJ 476	M2.5	-5.212	0.049
GJ 3117 A	M2.5	-4.788	0.045
G 214-14	M2.5	-5.326	0.062
GJ 4100	M2.5	-4.855	0.079
GJ 3470	M2.5	-4.908	0.086
GJ 674	M3	-5.039	0.069
GJ 388	M3	-4.249	0.042
GJ 752 A	M3	-5.158	0.049
GJ 581	M3	-5.752	0.077
GJ 625	M3	-5.659	0.064
GJ 408	M3	-5.324	0.048

Continued on next page

Table B.2 – *Continued from previous page*

GJ 667 C	M3	-5.610	0.067
GJ 480.1	M3	-5.735	0.107
GJ 793	M3	-5.030	0.057
GJ 438	M3	-5.377	0.059
GJ 877	M3	-5.282	0.055
HIP 31292	M3	-5.034	0.066
GJ 357	M3	-5.652	0.103
GJ 358	M3	-4.640	0.057
GJ 479	M3	-4.849	0.044
GJ 680	M3	-5.288	0.051
GJ 436	M3	-5.268	0.056
GJ 671	M3	-5.503	0.036
GJ 26	M3	-4.815	0.063
GJ 2128	M3	-5.524	0.067
BPM 96441	M3	-4.677	0.022
GJ 729	M3.5	-4.749	0.122
GJ 273	M3.5	-5.435	0.053
GJ 628	M3.5	-5.473	0.080
GJ 682	M3.5	-5.422	0.063
GJ 300	M3.5	-5.143	0.061
GJ 486	M3.5	-5.572	0.092
GJ 257 A	M3.5	-5.560	0.201
StKM 1-1877	M3.5	-4.319	0.037
GJ 163	M3.5	-5.302	0.069
GJ 317	M3.5	-5.252	0.090
GJ 699	M4	-5.928	0.078
GJ 54.1	M4	-5.105	0.085
GJ 234	M4	-4.409	0.214
GJ 3618	M4	-5.786	0.320
LP 816-60	M4	-5.137	0.075
GJ 213	M4	-5.817	0.161
GJ 555	M4	-5.396	0.048
GJ 402	M4	-5.413	0.059
GJ 4248	M4	-5.556	0.127
GJ 105 B	M4	-5.557	0.088
GJ 447	M4.5	-5.620	0.092
GJ 83.1	M4.5	-4.909	0.101
GJ 876	M4.5	-5.299	0.052

Continued on next page

Table B.2 – *Continued from previous page*

GJ 754	M4.5	-5.591	0.180
GJ 285	M4.5	-3.990	0.040
GJ 3737	M4.5	-5.780	0.146
GJ 299	M4.5	-5.836	0.208
GJ 4274	M4.5	-4.473	0.048
GJ 1224	M4.5	-5.066	0.116
GJ 1214	M4.5	-5.482	0.138
GJ 551	M5.5	-4.997	0.085
GJ 1061	M5.5	-5.754	0.101

Table B.3: H_α index measurements for a selection of stars in the sample

Star	Sp. Type	H_α Index	RMS H_α
HD 7439	F5	0.1746	0.0144
HD 30652	F6	0.2188	0.0007
HD 101198	F6.5	0.1688	0.0005
HD 222368	F7	0.1667	0.0009
HD 25171	F8	0.1714	0.0012
HD 19994	F8.5	0.1788	0.0014
HD 203608	F9	0.1767	0.0004
HD 1581	F9.5	0.1779	0.0004
HD 4307	F9.5	0.1743	0.0004
HD 2151	G0	0.1718	0.0008
HD 134060	G0	0.1801	0.0012
HD 1388	G0	0.1780	0.0010
HD 197210	G0	0.1900	0.0010
HD 10180	G1	0.1791	0.0006
HD 7134	G1	0.1730	0.0005
HD 30495	G1.5	0.1928	0.0019
HD 128620	G2	0.1856	0.0004
HD 2071	G2	0.1866	0.0007
HD 1320	G2	0.1858	0.0009
HD 213575	G2	0.1851	0.0007
HD 21019	G2	0.1827	0.0010
HD 41248	G2	0.1847	0.0007
HD 217014	G2.5	0.1861	0.0003

Continued on next page

Table B.3 – *Continued from previous page*

HD 1835	G3	0.2053	0.0024
HD 1461	G3	0.1874	0.0005
HD 20766	G4	0.1950	0.0024
HD 146233	G5	0.1835	0.0005
HD 12264	G5	0.1895	0.0019
HD 4915	G6	0.1875	0.0009
HD 59468	G6.5	0.1923	0.0005
HD 115617	G7	0.1945	0.0005
HD 20794	G8	0.1993	0.0008
HD 190248	G8	0.1977	0.0005
HD 210277	G8	0.1979	0.0005
HD 161098	G8	0.1872	0.0005
HD 10700	G8.5	0.2021	0.0004
HD 7438	G9	0.2084	0.0014
HD 63765	G9	0.2026	0.0018
HD 20781	G9.5	0.2107	0.0006
HD 165341 A	K0	0.2139	0.0005
HD 8389 A	K0	0.2178	0.0014
HD 220256	K0	0.2184	0.0009
HD 203384	K0	0.1954	0.0011
CoRoT-7	K0	0.2171	0.0035
HD 26965	K0.5	0.2187	0.0012
HD 128621	K1	0.2199	0.0008
HD 155885	K1	0.2411	0.0002
HD 20165	K1	0.2153	0.0008
HD 224789	K1	0.2391	0.0024
HD 22049	K2	0.2467	0.0022
HD 204941	K2	0.2207	0.0010
HD 191408	K2.5	0.2317	0.0007
HD 4628	K2.5	0.2286	0.0010
HD 40307	K2.5	0.2380	0.0010
HD 176986	K2.5	0.2287	0.0010
HD 220339	K2.5	0.2264	0.0018
HD 25151	K2.5		
HD 16160	K3	0.2453	0.0014
HD 32147	K3	0.2519	0.0013
HD 170493	K3	0.2553	0.0010

Continued on next page

Table B.3 – *Continued from previous page*

HD 104067	K3	0.2391	0.0013
HD 82342	K3.5	0.2542	0.0015
HD 131977	K4	0.2607	0.0018
HD 216803	K4	0.3020	0.0029
HD 125595	K4	0.2575	0.0014
HD 101581	K4.5	0.2688	0.0016
HD 209100	K5	0.2576	0.0010
HIP 5158	K5	0.2542	0.0021
HD 120467	K5.5	0.2840	0.0015
HD 85512	K6	0.2830	0.0012
HD 203040	K6.5	0.3314	0.0036
HD 211970	K7	0.3319	0.0069
HD 132683	K8	0.3222	0.0045
HD 113538	K9	0.3046	0.0025
GJ 229	M0	0.3563	0.0058
GJ 884	M0	0.3347	0.0166
GJ 846	M0	0.3597	0.0052
GJ 184	M0	0.3598	0.0034
GJ 731	M0	0.3673	0.0038
GJ 548 A	M0	0.3459	0.0078
GJ 3942	M0	0.3807	0.0099
GJ 4057	M0	0.3392	0.0037
GJ 9482	M0	0.3338	0.0054
GJ 9404	M0	0.3387	0.0098
GJ 4092	M0	0.3235	0.0024
TYC 3973-2034-1	M0	0.4615	0.0226
G 125-69	M0	0.3883	0.0043
GJ 119 A	M0	0.3386	0.0023
TYC 694-1183-1	M0	0.3891	0.0260
GJ 9793	M0	0.4409	0.0219
HIP 17248	M0	0.8649	0.0020
2MASS J22+37[3]	M0	0.3583	0.0057
K2-3	M0	0.3407	0.0017
GJ 784	M0.5	0.3534	0.0048
GJ 803	M0.5	1.1353	0.1225

Continued on next page

[3] 2MASS J22353504+3712131

Table B.3 – *Continued from previous page*

GJ 740	M0.5	0.3475	0.0065
GJ 507 A	M0.5	0.3658	0.0047
GJ 685	M0.5	0.3737	0.0103
GJ 4306	M0.5	0.3702	0.0108
GJ 21	M0.5	0.3997	0.0092
GJ 3822	M0.5	0.3832	0.0094
GJ 694.2	M0.5	0.3536	0.0038
GJ 9689	M0.5	0.3390	0.0042
GJ 191	M1	0.4288	0.0066
GJ 1	M1	0.4125	0.0061
GJ 412 A	M1	0.4138	0.0045
GJ 393	M1	0.4013	0.0073
GJ 514	M1	0.3621	0.0036
GJ 686	M1	0.3888	0.0038
GJ 536	M1	0.3747	0.0078
GJ 3997	M1	0.3693	0.0041
GJ 606	M1	0.4125	0.0159
GJ 3649	M1	0.3980	0.0133
GJ 9122 B	M1	0.3894	0.0117
GJ 3998	M1	0.3626	0.0052
GJ 1074	M1	0.3578	0.0055
GJ 119B	M1	0.3830	0.0045
GJ 3352	M1	0.3590	0.0025
GJ 832	M1.5	0.3879	0.0052
GJ 205	M1.5	0.3742	0.0097
GJ 185 A	M1.5	0.3528	0.0060
GJ 49	M1.5	0.4357	0.0139
GJ 16	M1.5	0.3785	0.0059
GJ 220	M1.5	0.3698	0.0007
GJ 4182	M1.5	0.3631	0.0148
GJ 887	M2	0.3771	0.0068
GJ 15 A	M2	0.4052	0.0034
GJ 526	M2	0.3754	0.0039
GJ 693	M2	0.4360	0.0067
GJ 908	M2	0.3915	0.0037
GJ 880	M2	0.3781	0.0095
GJ 701	M2	0.3730	0.0041
GJ 382	M2	0.4064	0.0137

Continued on next page

Table B.3 – *Continued from previous page*

GJ 450	M2	0.4550	0.0241
GJ 433	M2	0.3823	0.0045
GJ 2	M2	0.3910	0.0105
GJ 70	M2	0.4396	0.0143
GJ 410	M2	0.5407	0.0236
GJ 414 B	M2	0.3806	0.0075
GJ 47	M2	0.4156	0.0116
GJ 3126	M2	0.4142	0.0089
GJ 895	M2	0.3650	0.0053
GJ 521	M2	0.3734	0.0024
GJ 272	M2	0.3544	0.0035
GJ 507.1	M2	0.3328	0.0029
StKM 1-587	M2	0.3392	0.0059
GJ 1030	M2	0.3966	0.0095
GJ 563.2 A	M2	0.3928	0.0045
GJ 588	M2.5	0.4157	0.0053
GJ 176	M2.5	0.4166	0.0175
GJ 162	M2.5	0.3822	0.0106
GJ 552	M2.5	0.3969	0.0055
GJ 399	M2.5	0.4046	0.0055
G 234-57	M2.5	0.5805	0.0194
GJ 476	M2.5	0.3907	0.0070
GJ 3117 A	M2.5	0.4094	0.0080
G 214-14	M2.5	0.3646	0.0043
GJ 4100	M2.5	0.3790	0.0094
GJ 3470	M2.5	0.4039	0.0093
GJ 674	M3	0.5260	0.0398
GJ 388	M3	1.4721	0.0940
GJ 752 A	M3	0.4020	0.0098
GJ 581	M3	0.4452	0.0054
GJ 625	M3	0.4129	0.0078
GJ 408	M3	0.4145	0.0104
GJ 667 C	M3	0.4124	0.0068
GJ 480.1	M3	0.4528	0.0096
GJ 793	M3	0.4900	0.0250
GJ 438	M3	0.3884	0.0044
GJ 877	M3	0.4155	0.0100
HIP 31292	M3	0.4349	0.0070

Continued on next page

Table B.3 – *Continued from previous page*

GJ 357	M3	0.4225	0.0048
GJ 358	M3	0.7539	0.0769
GJ 479	M3	0.5393	0.0250
GJ 680	M3	0.3882	0.0039
GJ 436	M3	0.4106	0.0039
GJ 671	M3	0.4148	0.0036
GJ 26	M3	0.4463	0.0214
GJ 2128	M3	0.4053	0.0031
BPM 96441	M3	0.3390	0.0075
GJ 729	M3.5	1.1708	0.2023
GJ 273	M3.5	0.4624	0.0103
GJ 628	M3.5	0.4519	0.0056
GJ 682	M3.5	0.4653	0.0131
GJ 300	M3.5	0.4798	0.0146
GJ 486	M3.5	0.4496	0.0044
GJ 257 A	M3.5	0.4379	0.0032
StKM 1-1877	M3.5	1.0184	0.0802
GJ 163	M3.5	0.4181	0.0057
GJ 317	M3.5	0.4478	0.0108
GJ 699	M4	0.4423	0.0064
GJ 54.1	M4	0.7935	0.1157
GJ 234	M4	1.8282	0.5748
GJ 3618	M4	0.4839	0.0126
LP 816-60	M4	0.4734	0.0151
GJ 213	M4	0.4540	0.0040
GJ 555	M4	0.4682	0.0057
GJ 402	M4	0.4647	0.0117
GJ 4248	M4	0.4467	0.0068
GJ 105 B	M4	0.4468	0.0086
GJ 447	M4.5	0.4672	0.0122
GJ 83.1	M4.5	1.0344	0.0818
GJ 876	M4.5	0.4535	0.0096
GJ 754	M4.5	0.4646	0.0165
GJ 285	M4.5	3.1464	0.2969
GJ 3737	M4.5	0.4564	0.0071
GJ 299	M4.5	0.4678	0.0248
GJ 4274	M4.5	1.7828	0.2074
GJ 1224	M4.5	1.7009	0.3344

Continued on next page

Table B.3 – *Continued from previous page*

GJ 1214	M4.5	0.4892	0.0143
GJ 551	M5.5	1.1846	0.1605
GJ 1061	M5.5	0.5108	0.0074

Table B.4: Mean photometric magnitude and RMS of the measurements for a selection of stars in the sample

Star	Sp. Type	m_V (mag)	$m_{V\ ASAS}$ (mag)	RMS (mmag)	Flag
HD 135559	A5	5.63	6.07	241.49	Bad Photometry
HD 129926	F0	4.94	5.53	168.31	Bad Photometry
HD 7439	F5	5.13	5.52	302.15	Bad Photometry
HD 30652	F6	3.19	3.99	276.07	Bad Photometry
HD 25171	F8	7.78	7.77	12.09	
HD 203608	F9	4.22	4.92	306.96	Bad Photometry
HD 1581	F9.5	4.23	4.96	327.28	Bad Photometry
HD 4307	F9.5	6.15	6.13	21.74	
HD 2151	G0	2.79	4.42	770.96	Bad Photometry
HD 134060	G0	6.29	6.32	14.77	
HD 1388	G0	6.50	6.50	18.58	
HD 197210	G0	7.61	7.60	14.97	
HD 10180	G1	7.32	7.32	14.97	
HD 7134	G1	7.46	7.47	15.05	
HD 30495	G1.5	5.50	5.97	281.17	Bad Photometry
HD 128620	G2	0.01	3.41	437.21	Bad Photometry
HD 2071	G2	7.27	7.27	12.92	
HD 1320	G2	7.98	7.95	12.47	
HD 21019	G2	6.20	6.21	25.28	
HD 41248	G2	8.81	8.81	13.69	
HD 217014	G2.5	5.46	5.89	196.98	Bad Photometry
HD 1461	G3	6.46	6.48	38.37	
HD 12264	G5	7.98	7.97	14.27	
HD 4915	G6	6.97	6.97	12.04	
HD 115617	G7	4.74	5.30	130.28	Bad Photometry

Continued on next page

Table B.4 – *Continued from previous page*

HD 20794	G8	4.27	4.90	246.26	Bad Photometry
HD 190248	G8	3.56	4.51	534.75	Bad Photometry
HD 210277	G8	6.63	6.54	22.94	
HD 161098	G8	7.67	7.68	13.31	
HD 63765	G9	8.10	8.09	11.43	
HD 8389 A	K0	7.84	7.80	15.83	
HD 220256	K0	8.56	8.54	13.33	
HD 203384	K0	8.02	8.01	14.94	
CoRoT-7	K0	11.67	11.62	43.45	
HD 26965	K0.5	4.43	4.96	115.90	Bad Photometry
HD 82558	K0.5	7.89	7.87	57.68	
HD 128621	K1	1.33	3.390	408.24	Bad Photometry
HD 155885	K1	5.08	4.97	145.43	
HD 20165	K1	7.80	7.81	11.05	
HD 224789	K1	8.24	8.24	18.15	
HD 22049	K2	3.73	4.63	397.37	Bad Photometry
HD 204941	K2	8.48	8.43	12.87	
HD 4628	K2.5	5.74	6.04	217.39	Bad Photometry
HD 40307	K2.5	7.15	7.14	14.07	
HD 176986	K2.5	8.45	8.46	13.45	
HD 220339	K2.5	7.80	7.78	14.79	
HD 32147	K3	6.21	6.19	25.51	
HD 104067	K3	7.92	7.91	16.31	
HD 82342	K3.5	8.32	8.32	15.88	
HD 131977	K4	5.72	5.82	186.69	
HD 125595	K4	9.03	8.99	16.34	
HD 209100	K5	4.69	5.40	360.34	Bad Photometry
HIP 5158	K5	10.21	10.13	15.52	
HD 85512	K6	7.65	7.64	14.63	
HD 13538	K9	9.06	9.05	15.76	
GJ 229	M0	8.12	8.13	18.38	
GJ 846	M0	9.15	9.15	15.07	
GJ 731	M0	10.10	10.15	15.01	
GJ 4057	M0	10.77	10.76	19.26	
GJ 9482	M0	10.38	10.374	17.33	
GJ 9404	M0	10.64	10.62	18.16	

Continued on next page

Table B.4 – *Continued from previous page*

TYC 743-1836-1	M0	10.79	10.73	26.47	
GJ 4092	M0	10.86	10.83	20.83	
TYC 694-1183-1	M0	11.21	11.22	27.74	
GJ 9793	M0	10.51	10.59	35.43	
K2-3	M0	12.17	12.15	60.63	
GJ 784	M0.5	7.97	7.95	16.40	
GJ 803	M0.5	8.63	8.63	44.47	
GJ 740	M0.5	9.22	9.22	17.77	
GJ 4306	M0.5	10.47	10.47	16.80	
GJ 3822	M0.5	10.64	10.63	19.91	
GJ 9689	M0.5	11.23	11.29	26.40	
GJ 191	M1	8.85	8.834	11.75	
GJ 1	M1	8.56	8.55	12.91	
GJ 514	M1	9.03	9.04	13.88	
GJ 686	M1	9.58	9.56	14.31	
GJ 536	M1	9.71	9.71	14.29	
GJ 3997	M1	10.37	10.34	18.44	
GJ 606	M1	10.49	10.47	18.31	
GJ 3649	M1	10.85	10.76	25.81	
GJ 9122 B	M1	10.76	10.77	26.90	
GJ 3998	M1	10.83	10.85	23.36	
GJ 3186	M1	11.05	11.08	30.80	
GJ 832	M1.5	8.67	8.67	15.86	
GJ 205	M1.5	7.97	7.95	17.12	
GJ 185 A	M1.5	9.00	8.30	16.52	Bad Photometry
GJ 16	M1.5	10.86	10.88	22.95	
GJ 220	M1.5	10.80	10.82	24.89	
GJ 887	M2	7.34	7.34	21.84	
GJ 526	M2	8.50	8.45	17.15	
GJ 693	M2	10.78	10.06	293.18	Bad Photometry
GJ 908	M2	8.99	8.98	14.38	
GJ 880	M2	8.64	8.66	16.22	
GJ 701	M2	9.36	9.38	16.01	
GJ 382	M2	9.26	9.24	23.95	
GJ 433	M2	9.81	9.80	14.15	
GJ 70	M2	10.91	10.93	27.31	
GJ 410	M2	9.57	9.58	24.68	
GJ 1030	M2	11.40	11.42	27.58	

Continued on next page

Table B.4 – *Continued from previous page*

GJ 563.2 A	M2	11.66	11.25	45.36	Bad Photometry
GJ 588	M2.5	9.31	9.33	12.24	
GJ 176	M2.5	9.95	10.01	23.73	
GJ 552	M2.5	10.68	10.678	15.97	
GJ 399	M2.5	11.28	11.30	39.54	
GJ 476	M2.5	11.40	11.43	35.69	
GJ 4100	M2.5	12.18	12.30	61.20	
GJ 3470	M2.5	12.27	12.36	65.61	
GJ 674	M3	9.41	9.39	21.60	
GJ 388	M3	9.43	9.33	29.60	
GJ 752 A	M3	9.12	9.14	14.47	
GJ 581	M3	10.57	10.57	17.52	
GJ 408	M3	10.02	10.03	16.38	
GJ 667 C	M3	10.22	6.44	422.89	Bad Photometry
GJ 480.1	M3	12.24	12.21	55.80	
GJ 438	M3	10.39	10.07	48.39	Bad Photometry
GJ 877	M3	10.38	10.39	22.48	
GJ 357	M3	10.92	10.91	20.70	
GJ 358	M3	10.69	10.72	40.08	
GJ 479	M3	10.66	10.67	23.51	
GJ 680	M3	10.13	10.13	22.53	
GJ 436	M3	10.59	10.64	19.23	
GJ 2128	M3	11.53	11.47	36.46	
GJ 729	M3.5	10.49	10.55	20.87	
GJ 273	M3.5	9.87	9.88	24.63	
GJ 628	M3.5	10.07	10.12	20.32	
GJ 300	M3.5	12.13	12.08	70.33	
GJ 486	M3.5	11.39	11.41	32.36	
GJ 163	M3.5	11.81	11.82	38.34	
GJ 317	M3.5	11.98	12.07	51.63	
GJ 699	M4	9.51	9.55	18.40	
GJ 54.1	M4	12.07	12.10	54.75	
GJ 234	M4	11.07	11.08	27.54	
G 99-49	M4	11.31	11.30	34.48	
GJ 3323	M4	12.20	12.19	63.92	
LP 816-60	M4	11.46	11.44	32.18	
GJ 213	M4	11.51	11.51	38.29	
GJ 555	M4	11.32	11.34	32.59	

Continued on next page

Table B.4 – *Continued from previous page*

GJ 105 B	M4	11.66	11.70	40.28
GJ 447	M4.5	11.15	11.12	26.04
GJ 83.1	M4.5	12.30	12.35	58.73
GJ 754	M4.5	12.23	12.28	53.03
GJ 285	M4.5	11.22	11.23	49.39
GJ 3737	M4.5	12.74	12.78	82.71
GJ 1154	M4.5	13.64	13.53	140.59
GJ 1214	M4.5	14.67	14.82	652.04
GJ876	M5	10.19	10.20	18.77
GJ 551	M5.5	11.13	11.23	38.80
GJ 1061	M5.5	13.07	13.08	131.48

C

Radial Velocity Analysis

Table C.1: Long-term cycles and rotation periods measured in this work for the stars in our sample. Periods are the mean periods of the measurements of the different activity proxies. Errors are the standard deviation of the different measurements.

Star	Sp. Type	RMS(V_r) [ms^{-1}]	σ V$_r$* [ms^{-1}]
HD 101198	F6.5	49.34	1.11
HD 222368	F7	3.75	1.20
HD 25171	F8	8.94	2.19
HD 19994	F8.5	11.89	1.27
HD 203608	F9	2.31	1.65
HD 1581	F9.5	2.70	0.79
HD 4307	F9.5	2.38	0.83
HD 2151	G0	2.64	0.73
HD 134060	G0	3.67	0.80
HD 1388	G0	36.36	0.80
HD 197210	G0	2.43	0.84
HD 10180	G1	5.77	0.84
HD 7134	G1	2.01	0.98
HD 30495	G1.5	11.22	1.06
HD 128620	G2	69.75	1.02
HD 2071	G2	3.76	0.80

Continued on next page

Table C.1 – *Continued from previous page*

HD 1320	G2	3.05	0.92
HD 213575	G2	2.49	0.79
HD 21019	G2	3.18	0.78
HD 41248	G2	3.91	1.41
HD 217014	G2.5	16.22	1.04
HD 1835	G3	29.82	1.78
HD 1461	G3	2.94	0.77
HD 20766	G5	7.90	0.94
HD 146233	G5	2.26	1.14
HD 12264	G5	11.76	1.15
HD 4915	G6	3.93	0.82
HD 59468	G6.5	1.38	0.73
HD 115617	G7	4.37	0.71
HD 20794	G8	4.19	0.70
HD 190248	G8	2.29	0.69
HD 210277	G8	20.13	0.71
HD 161098	G8	1.99	0.88
HD 10700	G8.5	2.38	0.71
HD 7438	G9	3.92	0.99
HD 63765	G9	11.67	0.82
HD 20781	G9.5	3.50	0.92
HD 165341A	K0	6.79	0.75
HD 8389A	K0	3.37	0.81
HD 220256	K0	2.12	0.98
HD 203384	K0	3.67	0.91
CoRoT-7	K0	10.71	2.15
HD 26965	K0.5	4.86	0.73
HD 128621	K1	332.08	1.02
HD 155885	K1	162.03	1.16
HD 20165	K1	3.53	0.88
HD 224789	K1	17.74	0.89
HD 22049	K2	5.94	0.69
HD 204941	K2	3.12	0.99
HD 191408	K2.5	3.69	0.80
HD 4628	K2.5	1.42	0.78
HD 40307	K2.5	2.83	0.75
HD 176986	K2.5	3.90	0.92

Continued on next page

Table C.1 – *Continued from previous page*

HD 220339	K2.5	2.26	0.86
HD 215152	K2.5	2.10	0.70
HD 16160	K3	3.66	0.76
HD 32147	K3	1.49	0.72
HD 170493	K3	2.28	0.83
HD 104067	K3	9.37	0.75
HD 82342	K3.5	2.48	0.86
HD 131977	K4	9.80	0.71
HD 216803	K4	15.12	0.97
HD 125595	K4	4.74	1.48
HD 101581	K4.5	2.51	0.83
HD 209100	K5	7.22	0.97
HIP 5158	K5	34.66	1.76
HD 120467	K5.5	5.91	1.88
HD 85512	K6	1.37	0.79
HD 203040	K6.5	4.40	2.09
HD 211970	K7	7.73	3.31
HD 132683	K8	3.51	2.70
HD 113538	K9	18.69	2.38
GJ 229	M0	2.79	0.93
GJ 884	M0	2.34	2.55
GJ 846	M0	5.29	1.56
GJ 184	M0	2.40	1.56
GJ 731	M0	2.87	1.82
GJ 548A	M0	3.99	1.60
GJ 3942	M0	5.74	1.98
GJ 4057	M0	3.91	2.25
GJ 9482	M0	28.74	2.63
GJ 9404	M0	3.88	2.05
GJ 4092	M0	4.91	2.45
TYC 3973-2034-1	M0	29298.80	6.52
G 125-69	M0	1609.02	3.12
GJ 119A	M0	3.43	1.64
TYC 694-1183-1	M0	14099.29	13.33
GJ 9793	M0	413.76	3.00
HIP 17248	M0	0.80	5.10

Continued on next page

Table C.1 – *Continued from previous page*

2MASS J22+37[1]	M0	3.50	4.82
K 2-3	M0	9.37	7.60
GJ 784	M0.5	5.68	2.40
GJ 803	M0.5	6029.95	7.05
GJ 740	M0.5	4.58	1.39
GJ 507 A	M0.5	2055.74	1.72
GJ 685	M0.5	6.26	1.64
GJ 4306	M0.5	2.84	1.72
GJ 21	M0.5	4.83	1.90
GJ 3822	M0.5	7.13	2.40
GJ 694.2	M0.5	24.14	2.11
GJ 9689	M0.5	4.67	2.42
GJ 191	M1	9.00	1.32
GJ 1	M1	6.13	1.13
GJ 412 A	M1	3.14	1.23
GJ 393	M1	2.7267	1.19
GJ 514	M1	2.77	1.23
GJ 686	M1	2.31	1.49
GJ 536	M1	3.43	1.31
GJ 3997	M1	12.28	1.89
GJ 606	M1	3.55	1.94
GJ 3649	M1	3.22	1.95
GJ 9122 B	M1	5.57	1.88
GJ 3998	M1	3.18	2.22
GJ 1074	M1	3.66	2.31
GJ 119 B	M1	3.96	1.86
GJ 3352	M1	2.69	2.28
GJ 832	M1.5	10.46	1.15
GJ 205	M1.5	4.99	1.17
GJ 185 A	M1.5	75.17	7.05
GJ 49	M1.5	3.88	1.25
GJ 16	M1.5	1.95	1.81
GJ 220	M1.5	4.99	2.22
GJ 4182	M1.5		3.85
GJ 887	M2	5.95	1.23
GJ 15 A	M2	2.89	1.05

Continued on next page

[1] 2MASS J22353504+3712131

Table C.1 – *Continued from previous page*

GJ 526	M2	2.97	1.17
GJ 693	M2	2.64	1.58
GJ 908	M2	2.55	1.20
GJ 880	M2	3.67	1.09
GJ 701	M2	2.52	1.31
GJ 382	M2	7.58	1.31
GJ 450	M2	4.49	1.45
GJ 433	M2	3.16	1.37
GJ 2	M2	3.76	1.33
GJ 70	M2	3.01	1.63
GJ 410	M2	8.38	1.90
GJ 414B	M2	2.27	1.47
GJ 47	M2	2.91	1.61
GJ 3126	M2	4.84	1.57
GJ 895	M2	1.27	1.68
GJ 521	M2	2.95	1.47
GJ 272	M2	4.80	3.52
GJ 507 1	M2	4.25	1.55
StKM 1-587	M2	13.10	5.51
GJ 1030	M2	3.97	2.33
GJ 563.2 A	M2	2.97	2.63
GJ 588	M2.5	1.934	1.19
GJ 176	M2.5	5.35	1.47
GJ 162	M2.5	3.84	1.49
GJ 552	M2.5	2.10	1.75
GJ 399	M2.5	2.63	2.17
G 234-57	M2.5	18.68	3.15
GJ 476	M2.5	2.72	1.97
GJ 3117A	M2.5	2.97	1.89
G 214-14	M2.5	4.68	2.72
GJ 4100	M2.5	5.86	4.89
GJ 3470	M2.5	8.57	3.81
GJ 674	M3	6.45	1.12
GJ 388	M3	28.02	1.42
GJ 752A	M3	2.78	1.00
GJ 581	M3	9.76	1.46
GJ 625	M3	2.81	1.30
GJ 408	M3	2.33	1.30

Continued on next page

Table C.1 – *Continued from previous page*

GJ 667C	M3	4.9214	1.51
GJ 480.1	M3	2.80	2.33
GJ 793	M3	2.49	1.42
GJ 438	M3	1.56	1.57
GJ 877	M3	4.48	1.45
HIP 31292	M3		
GJ 357	M3	3.71	1.64
GJ 358	M3	7.37	1.57
GJ 479	M3	4.21	1.46
GJ 680	M3	6.25	1.52
GJ 436	M3	11.35	1.69
GJ 671	M3	1.83	1.69
GJ 26	M3	2.95	1.64
GJ 2128	M3	2.45	2.24
BPM 96441	M3	6.47	3.82
GJ 729	M3.5	26.39	2.96
GJ 273	M3.5	4.51	1.17
GJ 628	M3.5	3.11	1.17
GJ682	M3.5	2.53	1.61
GJ 300	M3.5	5.91	2.04
GJ 486	M3.5	3.81	1.79
GJ 257A	M3.5	1786.99	2.06
StKM 1-1877	M3.5	25.60	5.03
GJ 163	M3.5	6.15	2.11
GJ 317	M3.5	24.93	2.33
GJ 699	M4	4.20	0.99
GJ 54.1	M4	3.75	2.13
GJ 234	M4	58.57	3.84
GJ 3618	M4	4.50	4.97
LP 816-60	M4	3.40	2.02
GJ 213	M4	3.20	1.92
GJ 555	M4	2.41	1.66
GJ 402	M4	1.19	2.03
GJ 4248	M4	2.84	2.24
GJ 105 B	M4	4.27	1.96
GJ 447	M4.5	2.27	1.58
GJ 83.1	M4.5	16.47	3.41
GJ 876	M4.5	157.13	1.25

Continued on next page

Table C.1 – *Continued from previous page*

GJ 754	M4.5	4.38	2.60
GJ 285	M4.5	127.61	5.41
GJ 3737	M4.5	4.44	2.92
GJ 299	M4.5	8.22	3.41
GJ 4274	M4.5	2.67	6.64
GJ 1224	M4.5	9.19	5.58
GJ 1214	M4.5	10.68	5.15
GJ 551	M5.5	3.56	1.70
GJ 1061	M5.5	2.74	2.72